MODELING OF ULTRATHIN CATALYST LAYERS IN POLYMER ELECTROLYTE FUEL CELLS: PROTON TRANSPORT AND WATER MANAGEMENT

by

Karen Chan

B.Sc, Simon Fraser University, 2007

A THESIS SUBMITTED IN PARTIAL FULFILLMENT

OF THE REQUIREMENTS FOR THE DEGREE OF

Doctor of Philosophy

in the

Department of Chemistry

Faculty of Science

SIMON FRASER UNIVERSITY

Summer 2013

APPROVAL

Name: Karen Chan

Degree: Doctor of Philosophy

Title of Thesis: Modeling of Ultrathin Catalyst Layers in Polymer Electrolyte Fuel Cells: Proton Transport and Water Management

Examining Committee:

Dr. Paul Percival, Professor
Chair

Dr. Michael Eikerling, Professor, Senior Supervisor

Dr. Steven Holdcroft, Professor, Supervisor

Dr. Kourosh Malek, Adjunct Professor,
Supervisor

Dr. Hogan Yu, Professor, Internal Examiner

Dr. Peter Berg, Associate Professor of Physics,
Norwegian University of Science and Technology,
External Examiner

Date Approved: August 9, 2013

Partial Copyright Licence

Abstract

Ultrathin catalyst layers (UTCLs) are emerging as a promising alternative to conventional catalyst layers in polymer electrolyte fuel cells. In comparison, UTCLs have dramatically reduced Pt loading and thicknesses and are ionomer–free. We explore two open questions in the theory of UTCLs (1) the proton transport mechanism within the ionomer–free layer and (2) water management in membrane electrode assemblies (MEAs) with UTCLs.

To investigate (1), we present a UTCL model, which assumes the protons are drawn into the UTCL via their interaction with the metal surface charge. We consider a continuum model of a water–filled, cylindrical nanopore with charged walls. We derive the relation between metal potential and surface charge density from a Stern double layer model.

The model suggests the proton concentration and reaction current density to be highly dependent on the charging properties of the metal|solution interface, which are parameterized primarily by the potential of zero charge. Therefore, materials for UTCLs should be selected not only for their intrinsic mass activities and durability, but also for their charging properties. A systematic evaluation of the interplay of electrostatic, kinetic, and mass transport phenomena in UTCL demanded an impedance variant of the model. Based on the general set of transient equations, we have derived analytical impedance expressions and equivalent circuit representations in 4 limiting cases.

While the UTCL model suggests the charging of the metal|solution interface to be crucial to performance, theoretical studies on the charging behaviour of platinum are limited. We present a generalised computational hydrogen electrode that enables the *ab initio* simulation of metal|solution interfaces as a function of pH and potential.

To address (2), we present a water balance model to MEAs with UTCLs. The model relates the current densities, capillary pressure distributions, and fluxes of vapor and liquid water. Analysis of the model suggests that UTCLs require efficient liquid transport paths out of the MEA at low and moderate temperature. We discuss strategies for increasing the current density for the onset of GDL flooding, via enhanced liquid permeabilities, vaporization areas, and gas pressure differentials.

Acknowledgments

First and foremost, I would like to thank Michael, my senior supervisor, for his consistent support and encouragement during the course of my PhD. I am inspired by the value he places on honest scientific inquiry and independent thought and I am grateful for the many opportunities he provided me – in particular, my participation in international conferences and my stay in Denmark. I also thank my committee members, Kourosh Malek and Steve Holdcroft, for their constructive feedback.

I thank the members of the Eikerling group for their friendship and collaboration. I am grateful for the feedback on various parts of this thesis from Alix, Mehrtoos, Swati, and in particular, Anatoly, who patiently critiqued the whole thing. I am also grateful to Liya for teaching me how to chill–out, Ata for his warm sense of humor, Swati for our deep conversations, Anatoly for incarnating the pleasant aspects of Sheldon Cooper, and Alix for his intellectual insights and emotional support.

I also thank the electrochemistry group at the Technical University of Denmark for making my stay there very memorable. In particular, I thank Jan for welcoming me into his group and inspiring me with his enthusiasm and creativity, Mårten for managing the collaboration and the scientific discussions he had with me, and Vladimir for training me to use GPAW and Dacapo and advising me on many occasions.

I thank Neil who has been teaching me about scientific writing since my undergrad years.

I acknowledge NSERC for funding, via a strategic project grant, graduate scholarships, and a foreign study supplement. I also thank the Simons Foundation and Simon Fraser University for entrance scholarships.

Finally, I am indebted to my "Tiger" parents for encouraging me to persevere on the quantitative stuff, and to my partner Stéphane, for his unconditional love and support, and for believing in my potential even at moments when I did not.

SYMBOLS AND ACRONYMS

Table 1: Acronyms.

Acronym	Definition
CL	catalyst layer
CNT	carbon nanotube
CNF	carbon nanofibre
CHE	computational hydrogen electrode
CV	cyclic voltammetry
DM	diffusion media
ECSA	electrochemically active surface area
EIS	electrochemical impedance spectroscopy
FF	flow field
HOR	hydrogen oxidation reaction
ICE	internal combustion engine
MEA	membrane electrode assembly
MPL	microporous layer
NSTF	nanostructured thin films (3M)
NPGL	nanoporous gold leaf
ORR	oxygen reduction reaction
PEFC	polymer electrolyte fuel cell
PEM	polymer electrolyte membrane
PB	Poisson–Boltzmann
PNP	Poisson–Nernst–Planck
PTFE	polytetrafluoroethylene
RHE	reversible hydrogen electrode
SHE	standard hydrogen electrode
UTCL	ultrathin catalyst layer

Anode and cathode components are indicated with “a” and “c” respectively, e.g. aCL means anode catalyst layer.

Table 2: Physical constants, parameters, variables for Chapters 2 and 3.

Symbol	Definition	Value	Reference
c_1	constant		Eq. (B.12)
c_2	constant		Eq. (B.13)
c_3	constant		Eq. (3.25)
C_{dl}	double layer capacitance (F cm^{-2})		Eq. (3.33)
c_{H^+}	proton concentration (M)		
$c^o_{H^+}$	PEM bulk proton concentration	1.25M	[1]
c_{O_2}	oxygen concentration (M)		
$c^o_{O_2}$	Oxygen concentration at GDL|CL	3.2×10^{-4}M	[2]
C_H	Pt Helmholtz Capacity	0.2 F m^{-1}	[3], [4], [5]
C_{PEM}	capacitance of the PEM|UTCL interface		Sec. 3.3.5
D_{H^+}	Proton Diffusion Coefficient	1.8×10^{-4} cm^2 s^{-1}	[6]
D_{O_2}	Oxygen Diffusion Coefficient [1]	1×10^{-4} cm^2 s^{-1}	[7]
E	Applied, non-IR corrected electrode potential		
f	frequency (Hz)		
F	Faraday constant	96485 C/mol	
h	heterogeneity factor, dimensionless		
H_{O_2}	Henry's constant for oxygen	0.00059 mol kg^{-1} bar^{-1}	[8]
j^o	Exchange current density		
	low cd region	1.96×10^{-9} A cm^{-2}	[9]
	high cd region	1.40×10^{-6} A cm^{-2}	[9]
j_C	capacitive current density (A m^{-2})		
j_{elec}	electrostatic contribution to j_F (A m^{-2})		
j_F	Faradaic current density (A m^{-2})		
j_{CL}	catalyst layer current density (A cm^{-2})		
k	inverse thermal voltage F/R_gT		
L	pore length	100nm - 1μm	

[1] D_{O_2} is calculated from the Wilke-Chang equation, [7] p.418.

n	pore density	1×10^{11} cm^{-2}	
$\mathbf{N}_{H^+}$	proton flux (mol m^{-2} s^{-1})		
$\mathbf{N}_{O_2}$	oxygen flux (mol m^{-2} s^{-1})		
$p^o_{O_2}$	Oxygen partial pressure at GDL|CL	0.53bar	
r	pore radial coordinate (m)		
R	pore radius	5nm	
R_{sol}	solution resistance (Ω cm^2),		Eq. (3.32)
R_{ct}	charge transfer resistance (Ω cm^2)		Eq. (3.40)
R_{ct,O_2}	fast H^+ limit resistive element (Ω cm^2)		Eq. (3.50)
R_g	gas constant	8.314 J mol^{-1} K^{-1}	
t	time (s)		
T	cell temperature	353K	
X_p	porosity, dimensionless		
z	pore axial coordinate (m)		
Z	pore impedance (Ω m^2)		
Z_{CL}	catalyst layer impedance (Ω cm^2)		
Z_{ct,O_2}	Fast H^+ limit diffusive element (Ω cm^2)		Eq. (3.50)
α	Transfer coefficient		
	low cd region	1	[10]
	high cd region	$1/2$	[10]
ε	Dielectric constant of water	$61\varepsilon_o = 5.4 \times 10^{-10}$ F/m	[11]
η	local overpotential (V)		
η_c	cathode overpotential (V)		
η_c^T	Transition overpotential	-0.37V	[12]
γ	Proton reaction order		
	low cd region	$3/2$	[10]
	high cd region	1	[10]
Γ	effectiveness of Pt utilization, dimensionless		
Γ_{elec}	electrostatic contribution to Γ, dimensionless		
Γ_{O_2}	oxygen contribution to the Γ, dimensionless		
Λ	constant factor, $F^2/8\varepsilon R_g T$		
ϕ	solution phase electric potential (V)		

ϕ^M	metal potential (V)		
ϕ_{eq}	equilibrium electrode potential	$1.2\mathrm{V_{SHE}}$	
ϕ^o_{eq}	equilibrium bulk PEM potential		
ϕ^{pzc}	Potential of zero charge	$0.3-1.1\mathrm{V_{SHE}}$	see text
ϕ^o	bulk PEM potential (V)		
ω	angular frequency (rad s^{-1})		
ω_d	characteristic diffusive frequency		Eq. (3.45)
ω_k	characteristic kinetic frequency		Eq. (3.45)
ω_{ct}	characteristic fast transport frequency		Sec. 3.3.2
ω_{sol}	onset frequency for R_{sol} dominated response		Eq. (3.35)
σ	surface charge density, (C m^{-2})		

A superscript "c" indicates values at pore centre, $r = 0$, superscript "o" refers to reference values, and subscript "eq" refers to equilibrium values. In Chapter 3, steady state variables are indicated with an overbar "$-$", and transient ones with "δ".

Table 3: Physical constants, parameters, variables for Chapter 5

Symbol	Definition	Value	Reference
D_{MPL}, D_{GDL}	Vapor diffusion coefficient of MPL, aGDL, cGDL	6.3 $\times 10^{-6}$ m^2/s	[13]
F	Faraday constant	96485 C/mol	
j_o	Faradaic current density		
j_i^{fl}	Current density at the onset of flooding in medium i		
j_a^M, j_c^M	Current density at onset of M regime in aGDL, cGDL		
$j_a^{V_g}$, $j_c^{V_g}$	Current density at onset of V$_g$ regime in aGDL, cGDL		
J_a, J_c	Total mass water flux out aGDL, cGDL		
J_i^L	Mass liquid flux in medium i		
J_i^V	Mass vapor flux in medium i		
J_o	Mass flux of water produced in ORR		
J_{eo}	Mass flux of electro–osmotic drag		
k_a, k_c	Permeability of aGDL, cGDL	1 $\times 10^{-17}$ m^2	[14]
k_{MPL}	Permeability of MPL	1.2$\times 10^{-19}$ m^2	[15]
k_{PEM}^{sat}	Permeability of saturated PEM	2.4$\times 10^{-19}$ m^2	[14]
L_{aTL}, L_{cTL}	Extent of anode and cathode transmission lines		
l_a, l_c	L_{aTL}/L_{GDL}, L_{cTL}/L_{GDL} respectively		
L_{GDL}	Thickness of gas diffusion layers	225μm	
L_{MPL}	Thickness of microporous layer	60μm	
L_{PEM}	Thickness of PEM	20μm	
M_w	Molar mass of water	0.018kg/mol	
n_{eo}	Electro-osmotic drag coefficient	2	
p^c	Capillary pressure $p^L - p^G$		
$p_{fl,CL}^c$	Flooding capillary pressure of CL	-2.5 bar	
$p_{fl,GDL}^c$	Flooding capillary pressure of GDL	6 kPa	[16]
p^G	Gas pressure		
p^L	Liquid pressure		
$p^{V,eq}$	Equilibrium vapor pressure	see Eq. (5.7)	
$p_\infty^{V,eq}$	Equilibrium vapor pressure at infinite pore radius	see Eq. (5.7)	
r	CL pore radius	50nm	
R	Gas constant	8.314 J K^{-1} mol^{-1}	

$R_a^L,\ R_c^L$	aGDL, cGDL liquid permeation resistance (m/s)	6.6×10^6	
R_{MPL}^L	cathode MPL liquid permeation resistance (m/s)	2.0×10^8	
R_{PEM}^L	PEM liquid permeation resistance (m/s)	3.3×10^7	
R_{CL}^{LV}	aCL, cCL vaporization resistance (m/s)	2.5×10^8	
R_{GDL}^{LV}	aGDL, cGDL vaporization resistance (m/s)	2.5×10^8	
$R_a^V,\ R_c^V$	aGDL, cGDL vapor diffusion resistance (m/s)	5.7×10^6	
R_{MPL}^V	MPL vapor diffusion resistance (m/s)	1.4×10^6	
RH_a, RH_c	Relative humidity at anode, cathode	50%	
T	Temperature	323K	
V_M	Molar volume of water	1.8×10^{-6} m^3/mol	
y_a, y_p, y_c	Normalised axes along aGDL, PEM, cGDL		
Δp^G	Gas pressure difference $p_c^G - p_a^G$	0 kPa	
γ	Surface tension of water	0.0626 Nm	[17]
κ^{LV}	Vaporization rate constant	4.13×10^{-9} kg Pa^{-1} s^{-1} m^2	[18]
μ_w	Viscosity of water	see Eq. (5.8)	
ρ_w	Density of water	1×10^3 kg m^{-3}	
θ	Contact angle of water|Pt	0	[19]
ξ_{CL}^{LV}	Liquid|vapor interfacial area in CL	1 m^2/m$^2_{geo}$	
ξ_{GDL}^{LV}	Liquid|vapor interfacial area in GDL	1 m^2/m$^2_{geo}$	

Contents

Chapter 1

Introduction

Polymer electrolyte fuel cells (PEFCs) are potential low emission power sources for portable, vehicular, and stationary devices due to their high thermodynamic efficiencies and energy densities. In state of the art PEFCs, cathode catalyst layers (cCLs) contribute to a major proportion (30-40%) of voltage efficiency losses [20]. The sluggish oxygen reduction reaction (ORR) demands high Pt loadings to achieve sufficient current densities. Improving cCL designs to enhance Pt utilization in order to lower Pt loading and the associated costs is a central objective of PEFC research.

Conventional cCLs are random three-phase composites of ionomer, gas pores, and carbon-supported Pt [21]. These three phases are required to provide pathways for proton, oxygen, and water transport, and electronic conduction. Model studies suggest that, due to statistical percolation and mass transport limitations in these relatively thick random composites, only $\sim$5% of the catalyst surface is effectively utilized [22]. This implies tremendous potential for Pt loading reduction through improved structural design.

Recently, ultrathin catalyst layers (UTCLs) have shown promising improvements in Pt-specific power densities. In contrast to conventional CLs, UTCLs are usually

ionomer-free and have reduced Pt loadings and thicknesses (20nm-1μm). UTCL research explores a wide variety of alternative support materials and structural designs. To date, the search for suitable materials and nanostructures is mostly based on trial and error. Little is known about the mode of proton transport, the increased propensity of membrane electrode assemblies (MEAs) with UTCLs to flooding, or the constraints on geometrical parameters like thickness, porosity and pore sizes of UTCLs. Systematic improvements in UTCL structural design and materials selection require an understanding of the physical phenomena that determine UTCL performance.

In this thesis, we develop models motivated by two major open questions in UTCL research: the proton transport mechanism, and the propensity of UTCLs to flooding. The thesis is organized as follows:

- In the rest of this chapter, we outline basic principles of the operation of PEFCs, their advantages and detriments, and provide a review of UTCL designs and properties.

- In Chapter 2, we present a steady state, single pore model, which proposes that protons are drawn into the water-flooded UTCL via their electrostatic interaction with the metal surface charge density at the pore wall. The model higlights the importance of metal|solution interfacial properties to UTCL performance.

- In Chapter 3, we present the impedance variant of the single pore model, which allows for the separation of electrostatic and kinetic contributions to UTCL performance.

- In Chapter 4, we outline the basics of density functional theory and its application to electrocatalysis, and present a generalised computational hydrogen electrode scheme for *ab initio* simulations of metal|solution interfaces. This scheme determines the ground state interfacial structure as a function of pH and potential, and allows one to calculate the charging behaviour of metal|solution interfaces.

- In Chapter 5, we present a water balance model of UTCL MEAs, which relates capillary pressure distributions, current density, and water and vapor fluxes at the anode and cathode. This model suggests UTCL MEAs require efficient liquid transport paths out the MEA at low to moderate T, due to their low vaporization capacity.

In what follows, we give an introduction to PEFCs – its layout, basic principles of operation, thermodynamics, overpotential losses, and cost and durability challenges. We focus in particular on the catalyst layer – its structure, fabrication methods, and design challenges. We review recent developments and challenges in the design of UTCLs.

1.1 Polymer Electrolyte Fuel Cells

1.1.1 Basic Principles

Polymer electrolyte fuel cells (PEFCs) are considered as a highly efficient, low-emission alternative to the internal combustion engine (ICE), and for applications in stationary, off-the-grid/back up power generation and portable electronics [23,24]. PEFCs are electrochemical cells that harness the free energy of the reaction of hydrogen and oxygen to do electrical work, via a separation of reactant gases and corresponding half-reactions with a gas tight, proton conducting polymer electrolyte membrane (PEM).

Fig. 1.1 shows a schematic of a PEFC membrane electrode assembly (MEA). The electrodes consist of catalyst layers (CLs) containing H^+–conducting ionomer and carbon supported Pt, diffusion media (DM) consisting of a gas diffusion layer (GDL) of carbon cloth or paper and usually, on the cathode side, a microporous layer (MPL) of hydrophobized carbon black, and gas flow fields (FFs). During operation, H_2 gas flows through the flow fields (FFs) and the porous diffusion media (DM) to the anode catalyst

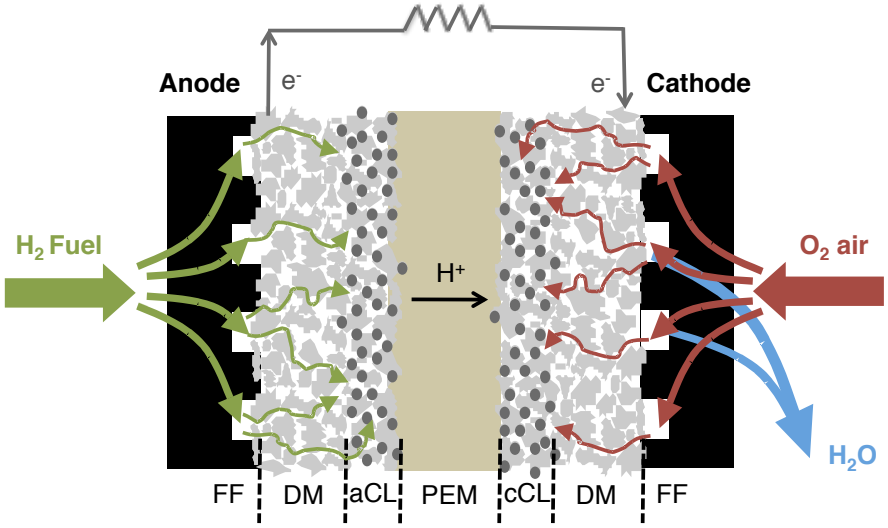

Figure 1.1: Schematic of a Polymer Electrolyte Fuel Cell; FF = flow fields, DM = diffusion media, CL = catalyst layer, PEM = polymer electrolyte membrane. Thicknesses are not to scale.

layer (aCL), where it oxidises:

$$H_2 \rightarrow 2H^+ + 2e^- \ . \tag{1.1}$$

The protons flow through the PEM, while the electrons flow through the external circuit to do electrical work. On the cathode side, O_2 (or air) flows through the FFs and DM towards the cCL, where it reduces with the protons coming from the PEM and electrons from the external circuit, to form H_2O:

$$^1/_2O_2 + 2H^+ + 2e^- \rightarrow H_2O \ . \tag{1.2}$$

The net reaction is simply

$$^1/_2O_2 + H_2 \rightarrow H_2O, \tag{1.3}$$

with the Gibbs free energy change of $\Delta G = -237$kJ/mol, the maximum work obtainable

for a fuel cell operating at constant pressure and temperature. Operation of PEFCs is usually restricted to < 100C since the PEM relies on liquid water for H^+ conduction.

At equilibrium and at standard conditions (pressure 1atm, 25C), the cell potential is

$$E^o_{eq} = -\frac{\Delta G}{2F} = 1.23\text{V} \ , \tag{1.4}$$

where the superscript o denotes standard conditions and F the Faraday constant. At other conditions, E_{eq} is given by the Nernst equation

$$E_{eq} = E^o_{eq} + \frac{RT}{2F} \ln\left(p_{H_2} p^{1/2}_{O_2}\right) \ , \tag{1.5}$$

where R is the gas constant, T the temperature, and p_i the pressure of gas i. To generate various output voltages (typically 6–200V), cells are connected in series to form a fuel cell stack [24]

The ideal, thermodynamic efficiency of a PEFC is one of its major advantages over ICEs. Energy conversion in ICEs is limited by the theoretical Carnot efficiency:

$$\varepsilon^{\text{Carnot}} = -\frac{W_r}{\Delta H} = 1 - \frac{T_2}{T_1} \tag{1.6}$$

where W_r is the reversible work performed, ΔH the enthalpy of reaction (heat drawn out of the hot reservoir) and T_1 and T_2 the temperatures of the hot and cold reservoirs, respectively. For most efficient engines at practical operating temperatures, $\varepsilon^{\text{Carnot}}$ does not exceed 50% [25].

In a fuel cell, the thermodynamic efficiency is:

$$\varepsilon^{\text{fc}} = -\frac{W_e}{\Delta H} = \frac{\Delta G}{\Delta H} \tag{1.7}$$

where W_e is the electrical work, and ΔH the enthalpy of reaction; the heat losses come from the -TΔS term in the ΔG. At 25^{o}C, $\Delta H = -286$ kJ/mol, and Eq. (1.7) gives a

theoretical efficiency of 83%.

The practical efficiency, however, in state–of–the–art PEFCs is considerably lower, due primarily to activation, ohmic, mass transport, and fuel utilization losses, and much of current research focusses on the reduction of such losses. The overpotential quantifies such losses, and is defined as

$$\eta = E - E_{eq} \,, \tag{1.8}$$

where E is the operating potential.

The largest overpotential loss in PEFCs arises from the sluggish oxygen reduction reaction (ORR). Generally, the current density from an electrochemical reaction is given by the Butler Volmer equation [26],

$$j = j^o \left[\left(\frac{c_a}{c_{a,o}} \right)^{\gamma_a} \exp\left(\frac{\alpha F \eta}{RT} \right) - \left(\frac{c_b}{c_{b,o}} \right)^{\gamma_b} \exp\left(-\frac{\beta F \eta}{RT} \right) \right] \,, \tag{1.9}$$

where j^o is the exchange current density, c the concentrations, with the o superscript indicating the reference concentrations for j^o, γ the reaction orders, and α and β the transfer coefficients for the oxidation and reduction reaction directions, respectively. j^o of the ORR is about 6 orders of magnitude smaller than that of hydrogen oxidation (HOR) [27, 28], so the ORR contributes to the majority of the activation overpotential losses. Ohmic and contact resistances in the PEM and electrical connections also contribute to overpotential losses; in particular, drying of the PEM under dry operation leads to dramatic increases in the Ohmic resistance [29]. Finally, excessive mass transport losses, resulting from electrode flooding and fuel starvation lead to transport-limited current densities.

The voltage efficiency is

$$\varepsilon^{\mathrm{v}} = \frac{E}{E_{eq}} \,. \tag{1.10}$$

The fuel utilization efficiency is [30]

$$\varepsilon^{\text{fuel}} = \frac{1}{\lambda},\ \lambda = \frac{nF v_{\text{fuel}}}{i} \tag{1.11}$$

where λ is the stoichiometry, v_{fuel} is the rate at which fuel is supplied (mol/s), and i is the current (A). Generally, slightly more fuel is supplied than required to prevent fuel starvation at the outlet of the flow fields, i.e. the cell is operated at $\lambda > 1$.

The practical efficiency of a fuel cell is thus

$$\varepsilon = \varepsilon^{\text{fc}} \cdot \varepsilon^{\text{v}} \cdot \varepsilon^{\text{fuel}}\ , \tag{1.12}$$

and is around $50-60\%$ in state of the art fuel cells [31]. In internal combustion engines, practical efficiencies are around 20% [32].

1.1.2 Cost and Durability Challenges in PEFCs

One of the major hurdles to commercialization of PEFCs is its cost. In particular, the sluggish ORR kinetics require the use of precious platinum/platinum alloys as catalysts. *Ab initio* electronic structure calculations have shown Pt and Pt–alloys to have the optimal binding energies to oxygen species for minimizing the activation losses in the ORR [33, 34]. Cheaper non–Pt catalysts still face stringent activity requirements; stack area cannot be increased indefinitely due to space limitations and increased costs of other MEA components, and dramatically increased electrode thicknesses would lead to higher mass transport limitations [35]. While research into platinum-free catalysts is very active, Pt and Pt alloys remain the most active and durable catalyst materials for the ORR [36, 37].

Figure 1.2 shows the cost breakdown for 2008 PEMFC systems and stack for the production of 500,000 systems/year; the stack contributes to 54% of the cost of the

system, and the catalyst ink to 56% of the stack. As a result, platinum contributes to ∼25% of the cost of the entire PEMFC system, and is the single largest cost contributor to a fuel cell stack. Thus, any efforts to reduce Pt loadings will yield large savings [20]. Cost aside, platinum is a limited resource. Current state-of-the art membrane electrode assemblies (MEAs) that meet voltage efficiency and MEA power density targets employ cathode and anode loadings of 0.4mg/cm^2 and 0.05mg/cm^2, respectively [38]. At such loadings, the estimated world platinum resources would be exhausted were only 20% of the world's automobiles run by PEFCs in 2020. Based on the 2012 US Department of Energy cost reduction targets, commercialization of fuel cells can only become viable when the total Pt loading in an MEA is reduced to ∼0.125mg/cm^2 [39].

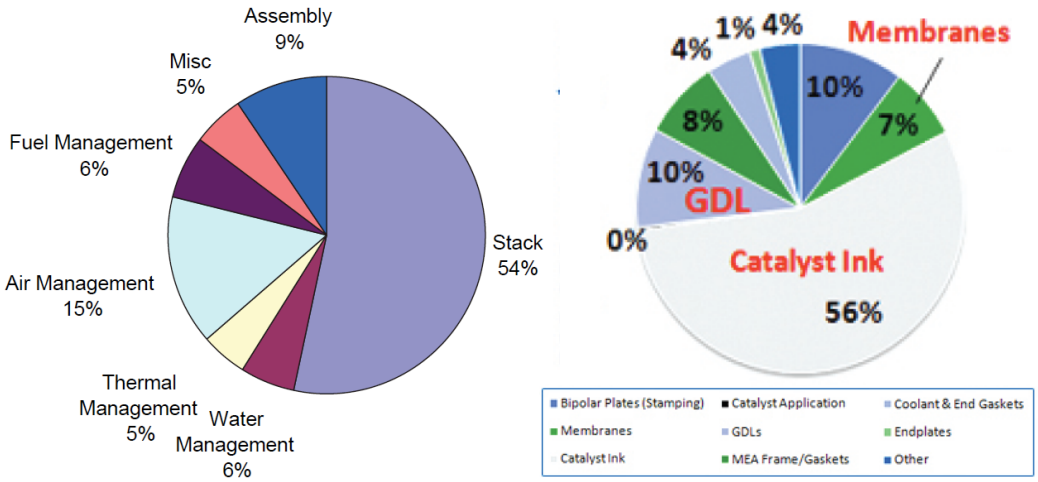

Figure 1.2: Cost breakdown for 2008 PEMFC system (left) and stack (right), stack estimates for 500,000 systems/yr. Reproduced from Ref. [20]. with permission from Fuel Cell Technologies Office, Office of Energy Efficiency and Renewable Energy, U.S. Department of Energy.

While a total Pt loading reduction to ∼0.125mg/cm^2 is dramatic, modelling studies of conventional cathode catalyst layers suggest this to be a possibility. Conventional catalyst layers are random three-phase composites; H^+ conduction occurs in ionomer or water-filled pores, electronic conduction in Pt nanoparticles on a carbon substrate,

and O_2 diffusion in gas pores. Optimal reaction sites, thus, reside close to where the three phases meet. Theory suggests Pt effectiveness of utilization in conventional layers to be only $\approx 5\%$ [22], due to the statistical limitation on Pt utilization and nonuniform reaction rate distributions. This leaves tremendous potential for performance improvement through new catalyst design; recent experimental research, discussed below, has shown promising results.

A further challenge for catalyst layer development is durability [20, 40]. The loss in active Pt surface area in conventional catalyst layers as a function of stack runtime, as shown in Figure 1.3, is substantial and well below DOE targets [20]. The low pH and elevated temperatures of the operating fuel cell and high start-up/shut down voltages lead to degradation of the catalyst layer through Pt dissolution, sintering/migration on the carbon support, and carbon corrosion. Increasing electrocatalyst durability remains a significant challenge in fuel cell commercialization and novel Pt catalyst layers must aim at DOE targets for stability [20]. Limited testing on non–Pt catalysts show that they face even greater challenges in durability improvement [37].

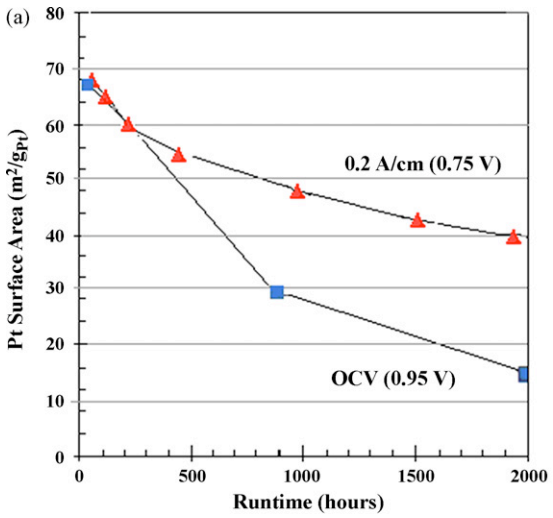

Figure 1.3: Pt surface area loss while operated at 0.95V and 0.75V. Reproduced from Ref. [41] with permission of The Electrochemical Society.

Since conventional aCLs show no significant loss of overpotential when Pt loading is reduced to 0.05mg/cm^2 [38], we discuss recent progress in the development of new cCLs. The reduction in Pt loading, while maintaining the same power output, means increasing overall Pt mass activity of the catalyst layer [35]) :

$$\text{Mass activity [A/mg]} = \frac{\text{Current density [A/cm}^2\text{]}}{\text{Pt loading [mg/cm}^2\text{]}} \tag{1.13}$$

Pt mass activity in catalyst layers can be increased through two avenues:

1. designing new CL structures that increase the effectiveness of Pt utilization via improved catalyst dispersion and/or decreased mass transport losses

2. designing new Pt–based materials to improve the intrinsic specific activity (current/real Pt surface area, at a given potential, [A/cm$^2_{\text{Pt}}$]) arising from electronic structure.

We focus on research motivated by the first avenue, although in some cases increased intrinsic Pt specific activities could also have influenced the overall UTCL performance. Recent efforts in alloying Pt to optimize its electronic structure have also shown promising results, especially at the single crystal level [42]. The ideal ultralow loading catalyst layer would combine a novel electrode structure with optimized Pt alloy catalyst materials. In the sections that follow, we discuss the structure of conventional layers, and review the research into ultralow Pt loading catalyst layers design.

1.2 Conventional Catalyst Layers

The first generation PEFCs were produced in the 1960s for NASA's Gemini spacecraft The catalysts were made of polytetrafluoroethylene (PTFE) bound fine Pt black powders, with loadings from 4 to 28mg/cm^2 [21, 43]. The high Pt loadings were prohibitive for commercialization, and PEFC development did not advance significantly until the

past two decades. In the 1980s, a major breakthrough in the reduction of catalyst loading was achieved in the development of carbon supported Pt catalysts bound by perfluorosulfonate ionomer (Nafion), which increased so much the surface area-to-volume ratio of Pt that loadings reduced to less than 1mg/cm^2 [44]. Fig. 1.4 shows a schematic of this

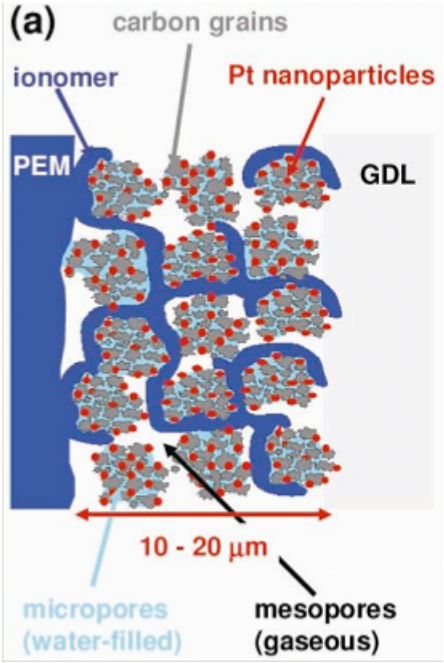

Figure 1.4: Schematic of a conventional catalyst layer. Reproduced from Ref. [45] with permission from Elsevier.

conventional CL. Carbon grains form agglomerates of 200-300nm, and the pores within the agglomerates are 20-40nm in size. Pt nanoparticles of 2.5–4nm sizes are deposited on the surface of the carbon grains, via electrochemical reduction of either a Pt solution or colloids on the carbon surface. Due to its large molecular size, ionomer does not penetrate into these small pores, and only surrounds the carbon agglomerates [45, 46]. Large secondary 40–200nm pores lie in the void spaces between agglomerates.

While many variants exist, the general catalyst layer preparation method consists of first dispersing the Pt/C partcles, ionomer, and, perhaps, a hydrophobizing agent, e.g.

polytetrafluoroethylene (PTFE), into a solvent to form a catalyst ink. The ink is applied to the DM or PEM , either through spraying, painting or decal transfer from a PTFE substrate. Solvents are removed by heat treatment, and hot-pressing is used to assemble the MEA [47].

1.3 Ultrathin Catalyst Layers

In contrast to conventional CLs, UTCLs are ionomer-free, over an order of magnitude thinner (20nm–1μm), and aim for dramatic reductions in Pt loading. Preliminary measurements of UTCL MEAs in recent literature do show comparable performance to standard Pt/C and increased specific power [48–51]. Optimization of other MEA components, such as GDLs, can further improve performance [49]. There are roughly two main types of UTCLs: support free ones, and ones utilizing novel support materials. In what follows, we discuss these two main types, and focus in particular on 3M nanostructured thin films (NSTFs), which are the most extensively tested alternative catalyst layer for PEFCs.

Support–free UTCLs are fabricated via sputtering or ion beam assisted deposition (IBAD) of Pt directly onto either the PEM or GDL [48, 49, 52, 53]. Sputtering involves the bombardment of a target material by energetic ions, leading to ejection and deposition of target atoms onto a substrate. IBAD combines either high temperature vacuum evaporation or sputtering with ion-beam bombardment of the substrate, which aids in heating the coating and coating/substrate interface and leads to a denser and more uniform film. Support-free catalysts have the advantage of being simple to fabricate, extremely thin ($<$100nm); increased utilization is thought to compensate for the lower dispersion and larger sizes (9-10nm [49]) of the Pt particles. Generally, steady state MEA performance was sensitive to thickness, and levels off beyond 20–50nm [48, 49, 53].

This levelling off has been attributed to limited gas transport in the denser thicker layers [48]. As discussed in Ch. 2, gas transport is likely not an issue in such thin layers, and the leveling off of the ECSA as loading is increased would be a likelier cause.

Novel support materials investigated in recent literature include carbon nanotubes and nanofibres (CNTs and CNFs), nanoporous gold, and non-conducting organic dye, used in 3M NSTF. Generally, Pt is deposited via reduction of Pt salts [50, 51, 54], or sputtering [55, 56]. Such support materials can have several advantages over carbon black: increased Pt dispersion over high surface area supports, and increased durability via supports with surface chemistry favorable for support-Pt interaction and superior resistance to corrosion.

In contrast to carbon black supports used in conventional catalyst layers, CNTs and CNFs have up to 5x higher specific surface areas, and do not contain micropores into which Pt nanoparticles may sink and be blocked from the reactant supply [36]. Sputtered Pt/oriented CNF UTCLs showed better steady state performance than plain sputtered Pt [55]; Caillard *et al.* postulates that oriented CNF carbon support promotes deeper penetration and sparser distribution of Pt nanoparticles and prevents the clustering of Pt nanoparticles that occurs with Pt layers sputtered directly onto Nafion or GDL [48, 53].

Carbon black is comprised of disordered basal graphite planes which interact weakly with supported platinum. CNFs are cylindrical structures consisting of stacked graphene layers. It has been postulated that the edges of the graphene planes at the outer surface of the fibers are stabler sites for small Pt nanoparticles, and the regular arrangement of such sites can distribute them more uniformly [57].

Finally, conventional carbon black suffers from corrosion at high electrode potentials during stop/start ups. The resultant Pt nanoparticle agglomeration and dissolution lead to dramatic losses of ECSA [58]. Hence, research into new, carbon-free supports has gained momentum in the past decade. For example, 3M NSTF and nanoporous

gold [59, 60] are thought to resist support corrosion due to the non-conductive nature of the NSTF support and the inertness of gold, respectively.

1.4 3M Nanostructured Thin Films

In the past 20 years, 3M has been developing promising carbon– and ionomer–free NSTF catalyst layers, which show superior durability and mass activities to conventional carbon supports [56,61–63]. The support particle is perylene red 149, a crystalline organic pigment, shown in Fig. 1.5. Perylene red is insoluble in common solvents, strong acids, and bases, and hence vacuum deposition is generally used for thin film fabrication. After vacuum deposition, the thin film is converted into oriented, densely packed crystalline "whiskers" by thermal annealing; whisker aspect ratios range from 20 to 50, whisker densities are 3-5 billion cm^{-2}, and a whisker cross-section is $\sim$50nm. The whisker's crystallinity and high resistivity affords high thermal and electrochemical stability under PEMFC operation conditions, as well as reproducibility and uniformity from batch to batch [61, 63, 64].

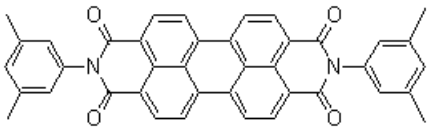

Figure 1.5: Perylene red 149 Structure [61, 65]

Fig. 1.6 shows a TEM image of a single whisker coated with Pt via sputtering. The Pt catalyst coating forms closely packed, discrete metal crystallites, called "whiskerettes", due to their elongated structure. Whiskerettes have diameters $\sim$ 8nm and lengths depending on both the whisker length and Pt loading. Lower Pt loadings or longer whiskers lead to smaller, shorter whiskerettes. The high degree of crystallinity of these individual metal whiskerettes is in contrast to the amorphous Pt coatings formed by IBAD.

Above loadings of 20μg/cm^2, the whiskers are completely coated by Pt in a continuous thin film, which eliminates any support oxidation and the resultant loss of ECSA [63]. The rough structure of the whiskerettes is almost completely smoothed out upon sample break–in via the 3M thermal and voltage cycling protocol [66].

To make an electrode, the whiskers are transferred from their substrate to a PEM. Fig. 1.7 shows SEM images of NSTF catalyst on its substrate (a) and after transfer to a PEM surface (b), without any ionomer application. Ionomer application has been shown to generally decrease performance, likely due to an increased O_2 transport resistance [64]. There is however, approximately ∼20% of the NSTF which are embedded into the ionomer, which may facilitate proton conduction [67]. The NSTF CL thickness about 0.3μm, which is 10 times thinner than conventional CLs [56].

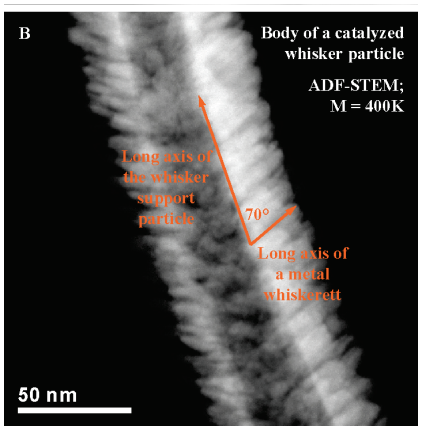

Figure 1.6: TEM image of NSTF Pt metal crystallites supported on perylene red whisker. Magnification 600,000 . Reproduced with permission from Ref. [63], Copyright 2008 American Chemical Society.

Due to the larger size of the Pt whiskerettes (∼8nm) than the Pt nanoparticles (2.5-4nm) in conventional Pt/carbon black electrodes, the ECSAs measured from cyclic voltammetry are only 10-20. This is much lower than that from conventional layers of similar loading, but is compensated by the ∼ 5 times higher area specific activity

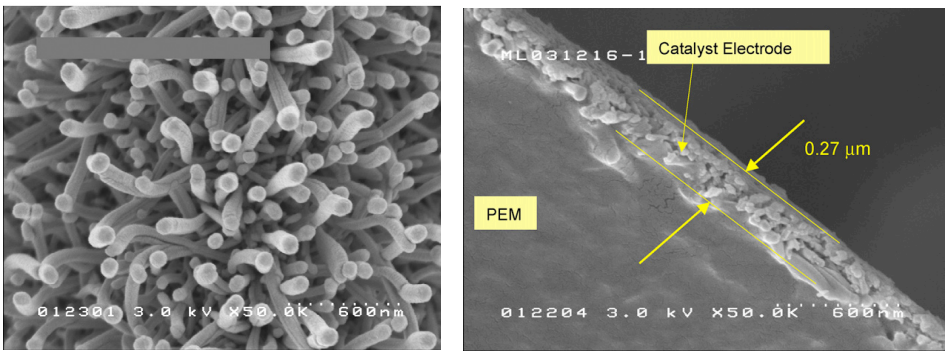

(a) (b)

Figure 1.7: (a) SEM image of NSTF catalysts on catalyst transfer substrate (b) SEM image of NSTF catalyst electrode layer after transfer to PEM surface. Magnification 50,000. Reprinted from Ref. [56] with permission from Elsevier.

($A/cm^2_{\text{active surface area}}$) of the NSTF. This large increase has been attributed to the bulk-like surface morphology of the Pt [63].

Aside from their lower loadings, the other major advantage of 3M's NSTF catalysts over conventional Pt/carbon black catalysts is their resistance to ECSA loss through support corrosion and Pt dissolution/agglomeration. Durability studies from 3M has compared ECSA losses of NSTF to Pt/carbon black as well as Pt/graphitic carbon under voltage cycling and at high voltage, 1.5V, where carbon corrosion is the primary degradation mechanism [56, 62]. Fig. 1.8(a) shows the ECSA losses of both NSTF and Pt/carbon black catalysts upon holding electrodes at 1.5V under saturated H_2/N_2 at 80C. Note that the much higher ECSA of Pt/C is due to the smaller Pt particle size and their dispersion over the carbon supports. ECSA in Pt/C degraded over 60% over 30min at 1.5V, while NSTF ECSAs remained stable after 180min at 1.5V. Fig. 1.8(b) shows the normalized ECSA losses (measured from hydrogen adsorption and desorption in CVs) for commercial Pt/Carbon black, 2 samples of Pt/Graphitic carbon of $0.4mg/cm^2$ Pt

loading, and four NSTF Pt and PtAB ternary catalysts of 0.1mg/cm^2 loading, cycled between 0.6-1.2V at 80C. All NSTF samples showed a leveling off of ECSA degradation at $\sim 30\%$, while the others all showed normalized ECSA losses of $> 90\%$.

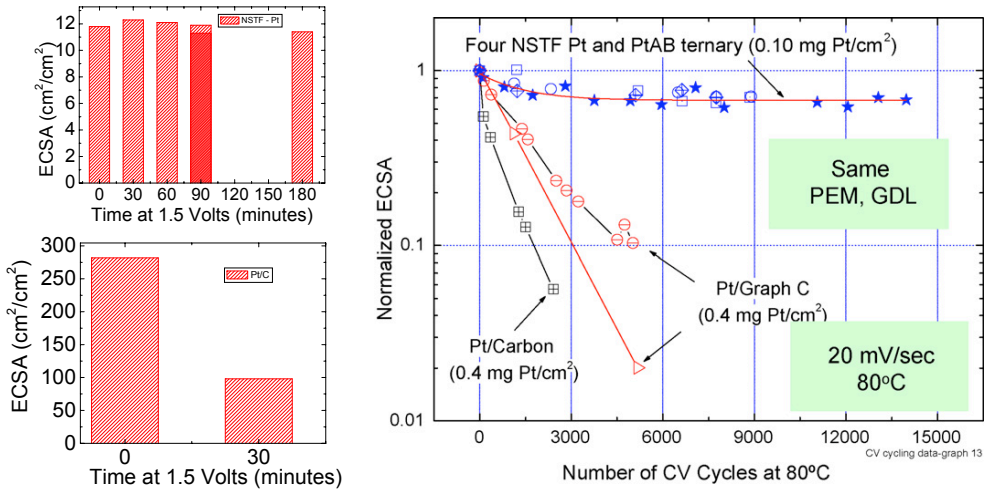

Figure 1.8: (a) ECSA losses upon holding electrodes at 1.5V under saturated H_2/N_2 at 80C. Reproduced from Ref. [62] with permission from The Electrochemical Society. (b) Normalised surface area vs. number of CV cycles from 0.6-1.2V for four NSTF Pt and PtAB samples, Pt/Graphitic carbon, and Pt/Carbon black. Reprinted from Ref. [56] with permission from Elsevier.

On the other hand, 3M NSTF MEAs show poorer performance than conventional layers at low RH and low temperatures (< 50C), and an increased propensity for cell reversal under load transients. The poor performance at low RH has been attributed to poor proton transport, and the poor performances at low temperature and under load transients has been attributed to catalyst layer flooding [68]. However, the latter hypothesis rests on the unrealistic assumption that O_2 does not diffuse in water; as we show in Sec. 2.4.2, oxygen penetration depth in flooded pores is sufficient at CL thicknesses of around 200nm. Current work in 3M NSTF focusses on mitigation of these water management issues via optimization of GDLs, operating pressures, addition of hygroscopic

silica particles to the NSTF, and hybrid Pt/C and NSTF catalyst layers [67, 69–72]

1.5 Scope and Outline of the Thesis

In this thesis, we explore two open questions in the theory of UTCLs:

- the proton transport mechanism within the ionomer-free UTCLs
- the susceptibility of UTCL membrane electrode assemblies (MEAs) to flooding

So far, there is no consensus on the mechanism of proton transport. A few recent studies have speculated on an unspecified surface proton transport mechanism [67, 73], but so far we have found no evidence to support an efficient surface transport mechanism. We postulate that the charging of Pt is the driving force for proton transport into the UTCL. As a first step, we consider bulk proton transport in flooded pores, where charging of Pt is considered as the driving force for proton transport into the UTCL. We also propose a computational scheme that allows for the calculation of metal surface charge from first principles.

The poor performance of UTCL MEAs at low T and during transients has been attributed to the flooding of the catalyst layer [68], which rests upon unrealistic assumptions on gas diffusivity in water. We explore water management in UTCLs via a water balance model, where we attribute the cause of the decrease in steady state polarization performance at low T to GDL flooding.

Chapter 2

Single Pore Model of UTCLs: Steady State Model

2.1 Introduction

In this chapter, we present a steady state, single–pore model of UTCLs [2][1]. Due to the structural differences between typical UTCLs and conventional CLs, available CL models cannot be applied to UTCLs. In conventional CLs, the embedded ionomer determines the proton concentration, and proton transport losses in the ionomer determine the overpotential distribution [45]. Since UTCLs contain no bulk electrolyte, the mechanism of proton transport in UTCLs is an open question.

Under capillary equilibrium and sufficient production of liquid water via the ORR (see Chapter 5), the nanosize, hydrophilic pores in UTCLs would be filled with water, through which protons can transport. We postulate that the proton concentration distribution within the pores is determined by the electrostatic interaction of the protons with the surface charge of the pore walls. We further assume that these protons undergo bulk

[1]This chapter reproduces in revised form material from Ref. [2], with permission from the Electrochemical Society.

transport through water via structural diffusion. These validity of these assumptions is suggested by recent experimental studies exploring surface charge-controlled ion transport in charged nanofluidic channels [74–76] and gold nanoporous membranes [77, 78]. In charged silica channels, results from a bulk ion transport model showed excellent agreement with experiment [79].

We neglect the consideration of a surface transport mechanism of protons, on which several recent studies have speculated [67,73,80]. A blocking electrode H_2/N_2 impedance study of ionomer-free Pt black electrodes, considered as a model system for 3M NSTF, found the proton conductivity to be 2-3 orders of magnitude larger than that of bulk water, and conductivity increased with RH [80]. It was proposed that the proton transports through an unspecified surface conduction mechanism; the RH dependence may be related to the thickness of the surface water films. Cyclic voltammograms of model systems of Pt pores [81–83] wetted with water, removed from ionomer, have been cited to support surface conduction [67, 73]. The 3M company has further speculated that a negatively charged hydroxyl covered surface may contribute to surface proton conduction [64]. However, neither the impedance nor cyclic voltammetry data elucidates any particular transport mechanism; they only show that water-wetted Pt remains active away from direct contact with Nafion. The RH dependence of proton conductivity in the Pt black system may also arise from the progressive flooding of pores; in the pores that are flooded, bulk transport could still prevail. To the best of our knowledge, there is no evidence in support of a surface proton transport mechanism on Pt or oxide-covered Pt surfaces that is comparable in efficiency to bulk proton transport in water. Furthermore, any future model of surface proton transport must also account for the effects of metal surface charge, since it is not screened by a bulk electrolyte.

Previously, UTCLs were modeled using a 1D macrohomogenoeous approach, where metal and solution phases were assumed to be one continuous, well-mixed phase [84]. Through the single-phase assumption, however, the electrostatic interaction between the

protons in solution and the metal surface charge density was neglected. To capture this interaction, we need to explicitly consider the charged metal|solution interface at UTCL pore walls, and hence return to a single–pore modeling approach. The substrate could consist either of an electronically conductive material with Pt nanoparticles deposited at pore walls, or it could be an insulating material covered with a continuous Pt layer, as in the case of 3M's nanowhisker-based UTCLs. As a first step, we consider a model system of a straight cylindrical nanopore with uniformly charged metal walls, corresponding to a uniform layer of Pt. We neglect complications of pore connectivity and tortuosity and local electric field fluctuations due to metal surface roughness or heterogeneity.

In what follows, we describe the model and discuss the input parameters. We introduce the effectiveness factor of Pt utilization, Γ, which quantifies the pore performance. We then present an analytical approximation to the solution of the fully coupled set of governing equations; this approximation allows us to decouple electrostatic and oxygen transport effects. We discuss the impact of metal|solution interfacial properties, ORR kinetic parameters, and pore geometry on the effectiveness of Pt utilization. For a comparison with typical UTCL polarization data, we scaled up the model, assuming a fixed pore size. Implications for UTCL design in view of high Γ are discussed.

2.2 Model Formulation

As shown in Fig. 2.1, we model a UTCL nanopore as a straight, water-filled cylinder of radius R and length L with smooth walls, at which a platinum layer of uniform thickness is deposited. Surface heterogeneities at the metal|solution interface are neglected. The pore is bounded at $z = 0$ by the PEM, which supplies the protons, and at $z = L$ by the GDL (or MPL), through which oxygen is supplied. Without embedded ionomer in the UTCL, the surface charge at the pore walls is the driving force for proton migration into the pore.

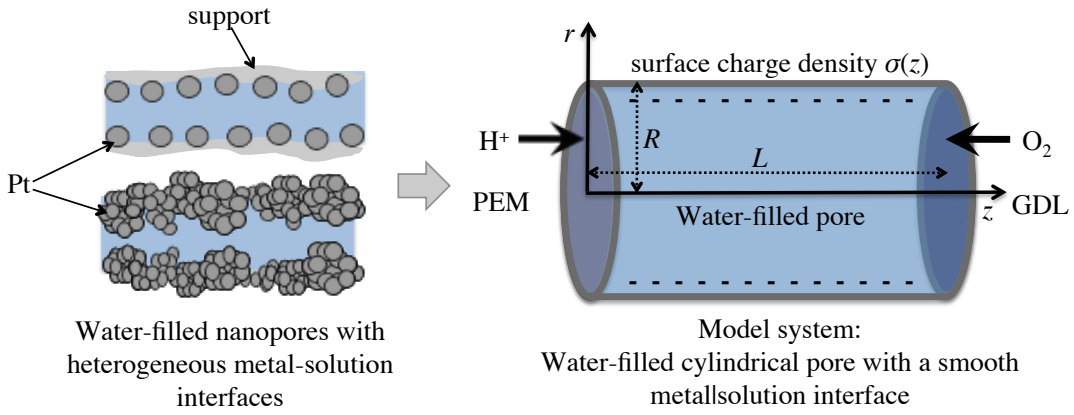

Figure 2.1: Model representation of a UTCL nanopore. We assume the pore is straight and cylindrical with charged Pt walls; we neglect surface roughness and pore tortuosity. We assume the pore is bounded by the PEM at one end and the GDL at the other.

To determine the electrochemical performance of the pore, we require the relation between the Faradaic current and the metal electrode potential. In order to establish this relation, we need (i) an electric double layer model to relate the applied electrode potential to the surface charge density at the pore wall, (ii) transport equations to relate the surface charge density to reactant concentrations, and (iii) charge transfer kinetic equations to relate local reactant concentrations and overpotentials to the electrochemical current density. The developed continuum model consists of coupled relations for reactant transport, metal surface charge, and charge transfer kinetics.

We expect the continuum approach to be accurate when the size of the pore is large compared to the size of a hydrated proton. In studies of biological ion channels, results of continuum models and molecular dynamics simulations do agree in channels of >15Å diameter [85, 86]. We restrict analysis of the model to pore radii larger than 2nm.

2.2.1 Governing Equations

The governing equations for this model are steady-state reactant transport equations. Distributions of proton concentration, c_{H^+}, and electric potential, ϕ, are determined by the Poisson-Nernst-Planck (PNP) equation, which has been widely applied in the theory of ion transport in biological membranes [87, 88]. We neglect proton transport from convection [84]; water and proton fluxes should be similar in magnitude, and we expect a much lower concentration of protons than water (i.e. c_{H^+} = 1M corresponds to 1 H^+/55 H_2O molecules). We also neglect the small concentration of hydroxide ions from water dissociation. Oxygen diffusion is determined by Fick's law.

In PNP theory, the proton flux, $\mathbf{N}_{H^+}$, is

$$\mathbf{N}_{H^+} = -D_{H^+}\left[\nabla c_{H^+} + c_{H^+} k \nabla \phi\right] \tag{2.1}$$

$$\nabla^2 \phi = -\frac{c_{H^+} F}{\varepsilon}, \tag{2.2}$$

where D_{H^+} is the proton diffusion coefficient in water, k is the inverse thermal voltage $F/R_g T$, and $\varepsilon = \varepsilon_r \varepsilon_o$ the dielectric constant of water. As discussed in Sec. (2.3.3), we do not consider dielectric saturation under normal operating conditions. Mass conservation requires $\nabla \cdot \mathbf{N}_{H^+} = 0$.

From Fick's law, the oxygen flux is

$$\mathbf{N}_{O_2} = -D_{O_2} \nabla c_{O_2}. \tag{2.3}$$

From mass conservation, the oxygen concentration is given by the Laplace equation,

$$\nabla^2 c_{O_2} = 0. \tag{2.4}$$

2.2.2 Boundary Conditions

At $z = 0$, the PEM|pore interface, the proton concentration, $c^o_{H^+}$, is assumed to be the volume-averaged proton concentration of the bulk PEM. This assumption neglects the charge distribution at the PEM|UTCL interface, as well as any fluctuations in potential arising from the PEM microstructure. The potential ϕ^o at the interface will hence be assumed uniform as well. The boundary conditions are thus

$$c_{H^+}(r,0) = c^o_{H^+}, \;\; \phi(r,0) = \phi^o. \tag{2.5}$$

The PEM is assumed to be gas–tight, i.e. the flux of oxygen at $z = 0$ is zero, so that

$$\partial_z c_{O_2}\big|_{(r,0)} = 0. \tag{2.6}$$

At $z = L$, the pore|GDL interface, the concentration of dissolved O_2, $c^o_{O_2}$, is determined from the oxygen partial pressure, $p^o_{O_2}$, using Henry's law,

$$c_{O_2}(r,L) = c^o_{O_2} = H_{O_2} p^o_{O_2}, \tag{2.7}$$

where H_{O_2} is Henry's constant for oxygen solubility in water. Assuming the DM is not flooded, the proton flux and electric field vanish at $z = L$,

$$N_{H^+,z}\big|_{(r,L)} = 0, \;\; \partial_z \phi\big|_{(r,L)} = 0\,. \tag{2.8}$$

We assume that $r = R$ corresponds to the reaction, or Helmholtz plane (see Sec. 2.2.3). The normal components of proton and oxygen fluxes are determined by the local Faradaic current density $j(z)$, given by the cathodic branch of the Butler-Volmer

equation,

$$N_{\mathrm{H}^+,r}|_{(R,z)} = \frac{j(z)}{F}, \quad N_{\mathrm{O}_2,r}|_{(R,z)} = \frac{j(z)}{4F} \ , \tag{2.9}$$

$$j_F(z) = j^o \left(\frac{c_{\mathrm{O}_2}(R,z)}{c^o_{O_2}} \right) \left(\frac{c_{H^+}(R,z)}{c^o_{H^+}} \right)^{\gamma} \exp\left(-\alpha k \eta(z)\right), \tag{2.10}$$

where j^o is the exchange current density corresponding to concentrations $c^o_{H^+}$ in the PEM and $c^o_{O_2}$ at the GDL, α the transfer coefficient, and γ is the reaction order of H^+ (to simplify notation we have omitted that for O_2 which is 1). The local overpotential at the reaction plane is

$$\eta(z) = (\phi^M - \phi(R,z)) - (\phi^M_{eq} - \phi^o_{eq}) \ , \tag{2.11}$$

where ϕ^M refers to the metal potential and subscripts "*eq*" indicate values at equilibrium. With the macroscopic cathode overpotential,

$$\eta_c = (\phi^M - \phi^o) - (\phi^M_{eq} - \phi^o_{eq}) \ , \tag{2.12}$$

we rewrite η with a Frumkin, diffuse layer correction, $(\phi(R,z) - \phi^o)$, to η_c [89],

$$\eta(z) = \eta_c - (\phi(R,z) - \phi^o) \ . \tag{2.13}$$

Table 2 lists the symbols and the definitions of the potentials used in the model. The boundary condition for potential that relates $\phi(R,z)$ to ϕ^M requires special consideration, and is discussed in the next section.

2.2.3 Boundary Condition for Potential at the Pore Walls

A crucial aspect of the model is the boundary condition for the electrostatic potential at the reaction plane, $r = R$. It captures the electrostatic interaction between the protons and the charged metal pore walls. Along the pore walls, both the reaction plane potential

$\phi(R,z)$ and metal surface charge density, $\sigma(z)$, can vary along z, depending on the proton distribution. The boundary condition should relate ϕ^M to $\phi(R,z)$ and/or the surface charge density $\sigma(z)$. Such a relation requires a model of the metal|solution interface.

We present here the straightforward derivation of the boundary condition for the case of a simple adsorbate–free metal|solution interface. We apply this simple boundary condition to the model as a first approximation. We provide a discussion of the possible complications of oxide formation processes at the Pt|solution interface in Appendix A.

We apply the Stern model of a metal|solution interface, illustrated in Fig. 2.2. The interface is considered as a series circuit of compact Helmholtz and diffuse layer capacitors that meet at the outer Helmholtz plane, the plane of closest approach of hydrated protons to the metal [89]. The interfacial capacitance $C_{dl} = \frac{d\sigma}{d(\phi^M - \phi^o)}$ is

$$\frac{1}{C_{dl}} = \frac{1}{C_H} + \frac{1}{C_{diff}} \tag{2.14}$$

$$C_H = \frac{d\sigma}{d(\phi_M - \phi(R,z))},\ C_{diff} = \frac{d\sigma}{d(\phi(R,z) - \phi^o)}\ , \tag{2.15}$$

where C_{diff} is the diffuse layer capacitance. C_H is determined primarily by metal, solvent and adsorbate electronic distributions and interactions, while C_{diff} is determined by the ionic charge distribution in solution. In the absence of specific adsorption, C_H can be determined by double layer capacitance measurements in sufficiently concentrated solutions, where $\phi^o \sim \phi(R,z)$ and $C_{dl} \sim C_H$, or through Parsons-Zobel plots [90].

We integrate the Helmholtz capacitance C_H to relate $\sigma(z)$ to ϕ^M,

$$\sigma(z) = \int_{\phi^{pzc} - \phi^o}^{\phi^M - \phi(R,z)} C_H(\phi) d\phi\ , \tag{2.16}$$

where ϕ^{pzc} is the potential of zero charge of the metal, and $\phi(R,z)$ the diffuse layer correction arising from the proton distribution in the pore. Further assuming a relatively constant Helmholtz capacitance and applying Gauss' law, $\sigma(z) = \varepsilon \partial_r \phi\big|_{R,z}$, we obtain a

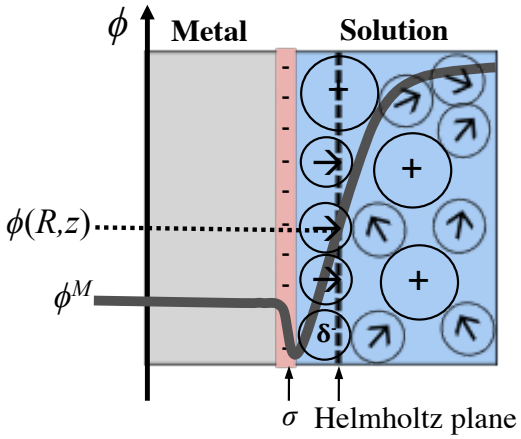

Figure 2.2: Schematic of the Stern model of the electrochemical interface.

Robin boundary condition for the potential at the pore walls,

$$\sigma = \varepsilon \partial_r \phi \big|_{R,z} = C_H \left[\left(\phi^M - \phi(R,z) \right) - \left(\phi^{pzc} - \phi^o \right) \right] . \tag{2.17}$$

A similar approach to the boundary condition for potential at the metal|solution interface has recently been applied by Bazant *et al.* [91, 92] to various electrochemical systems; however, they neglected consideration of the ϕ^{pzc}, which parametrizes the charging behaviour of a given metal|solution interface.

In principle, spatially varying dielectric constants and finite size effects can be included, via modifications to the PNP equations [93]. However, the Stern model does heuristically account for the saturated dielectric constant at the interface via the Helmholtz capacitance; the model also sets a distance of closest approach for the solvated protons.

2.2.4 Effectiveness Factor of Pt Utilization

To quantify the performance of the pore, we introduce an effectiveness factor of Pt utilization, Γ. This is defined by the total current produced by the pore, normalized by an "ideal" current that would be obtained, if reactant and potential distributions were completely uniform, $c_{H^+}(R,z) = c^o_{H^+}$, $\phi(R,z) = \phi^o$, and $c_{O_2}(R,z) = c^o_{O_2}$. This ideal corresponds to a "perfectly utilized" conventional CL:

$$\Gamma = \frac{\int_0^L j_F(R,z)dz}{L \times j_{ideal}}, j_{ideal} = j^o \exp\left(-\alpha k \eta_c\right). \tag{2.18}$$

2.3 Model Parameters

This section discusses various parameters listed in Table 2.

2.3.1 ORR Kinetic Parameters

Key parameters in the effective Butler-Volmer equation for oxygen reduction are the proton reaction order γ, the transfer coefficient α, and the exchange current density j^o (the O_2 reaction order, not written explicitly, is one). The rate-determining step is the proton transfer to oxygen reduction step,

$$O_2 \rightleftharpoons O_{2(ads)} \tag{2.19}$$

$$O_{2(ads)} + H^+ + e^- \rightarrow O_2H_{(ads)} \tag{2.20}$$

as originally proposed by Damjanovic [10, 94–96]. A doubling of Tafel slopes from $\approx$ –60mV/decade to $\approx$ –120 mV/decade at room temperature results from a transition between Temkin to Langmuirian kinetics upon decreasing electrode potential. This causes a shift in the effective transfer coefficient and reaction order from $\alpha = \frac{1}{2}$ and $\gamma = 1$ at low current density to $\alpha = 1$ and $\gamma = \frac{3}{2}$ at high current density. The transition

between these two regions occurs near the onset of oxide species formation, around cathode overpotentials η_c of -0.3 to -0.5V. For the parameter study that follows, we assume that this transition occurs at η_c^T of -0.4V.

The ORR is normally considered to have two exchange current densities, corresponding to the Temkin and Langmuirian regions. We use the values from Parthasarathy's temperature-dependent microelectrode kinetic study for a Pt|Nafion interface [9], scaling them to the reference concentrations,

$$j^o = j_{ref} \left(\frac{c^o_{H^+}}{c^{ref}_{\mathrm{H}^+}} \right)^{\gamma} \left(\frac{c^o_{\mathrm{O}_2}}{c^{ref}_{\mathrm{O}_2}} \right), \tag{2.21}$$

where ref refers to Parthasarathy's experimental values. We expect j^o to vary with particle morphology, size, shape, and with the type of support material [97].

2.3.2 The Potential of Zero Charge

From the boundary condition for potential, Eq. (2.17), ϕ^{pzc} at the Pt|aqueous solution interface is required to determine $\sigma(z)$ and $\phi(R,z)$ at a given ϕ^M. The presence of adsorption processes on Pt led to Frumkin's definition of a potential of zero total charge, ϕ^{pztc}, and a potential of zero free charge, ϕ^{pzfc} [98, 99]. The former refers the potential where the sum of the excess free charge and the charge that has crossed the interface due to adsorption is zero, whereas the latter refers to the potential where the physical, excess free charge is zero. For Eq. (2.17), we require the ϕ^{pzfc}; in the sections that follow, ϕ^{pzc} will imply ϕ^{pzfc}.

Different measurement methods over the recent years have yielded a range of ϕ^{pzfc} for Pt. Measurements done using the CO-displacement method have found ϕ^{pztc} to be $0.33\mathrm{V}_{\mathrm{RHE}}$ [100]; the ϕ^{pzfc} was estimated to be close to this value [101]. Using an *ex situ* immersion method at a clean Pt(111) surface and 0.1 M $HClO_4$, Hamm *et al.* determined $\phi^{pztc} = 0.84\mathrm{V}_{\mathrm{SHE}}$ and estimated an even higher $\phi^{pzfc} \sim 1.1\mathrm{V}_{\mathrm{SHE}}$ [102]. Friedrich's

second harmonic generation study of the Pt(111) electrode in 0.1 and 0.001M $HClO_4$ solution found a negatively charged surface up to a potential of $0.6V_{RHE}$; complications from hydroxide adsorption precluded exact determination of ϕ^{pzfc}. Finally, Pajkossy *et al.*'s double layer capacitance measurements of aqueous solutions at low concentrations down to 10^{-3} mM failed to find a Gouy-Chapman minimum associated with a ϕ^{pzfc} within the range of $\sim$ 0 - $0.75V_{SHE}$ [3, 5].

A further complication is a possible second, "inversed" ϕ^{pzfc} in the oxide adsorption region, discovered by Frumkin and Petrii in the 1970s; at this inversed ϕ^{pzfc}, the surface charge shifts from positive and negative upon increasing potential [98, 103]. A more complex charging behaviour in the Pt oxide region was also proposed in a recent theoretical study of Pt(111), where ϕ^{pzc} was reported generally to increase with the degree of surface oxidation [104]. These results suggest that, in the case of oxide-covered Pt, the relation between σ and ϕ^{M} may be more complicated than implied by Eq. (2.17); with a second ϕ^{pzc} in the oxide region, the relation would no longer be monotonic, and requires the more general treatment described in Appendix A. Our present approach emphasises the importance of charging phenomena at the metal|solution interface, but it may not account for the complications that could arise from the progressive oxidation of Pt at high ϕ^{M}. We considered the ϕ^{pzc} as a variable parameter in with the range 0.3 – $1.1V_{SHE}$.

2.3.3 Dielectric Constant of Water Inside the Nanopore

The model equations assume a constant dielectric constant within the diffuse layer. This assumption was made in view of Paul and Paddison's statistical mechanical model of water in polymer electrolyte membranes [105, 106]. This model assumes the PEM to be comprised of water-filled channels lined by arrays of dissociated sulfonic acid groups, with surface charge density around -0.3C/m^2. Their model results indicate that substantial deviations of the dielectric constant, ε, from the bulk value are limited to about

3-4Å away from the SO_3^- group centres. Smoothing out the SO_3^- distribution within the channel at constant charge density reduces the width of the region in which ε is reduced from the bulk value. In the case of a uniform charge distribution - the case of interest here - the extent of dielectric saturation due to the charged surface is expected to be reduced further from 3-4Å. Similarly, in Yeh and Berkowitz' molecular dynamics study of water at the Pt(111) interface under constant applied electric fields, major field and charge density fluctuations arising from water-Pt interactions were generally contained within $\sim$ 5Å. As shown below in the inset of Fig. 2.4, absolute surface charge densities $|\sigma|$ calculated with an unsaturated ε for the relevant range of $\phi^M - \phi^{pzc}$ do not exceed 0.1Cm^{-2}; a lowered ε would only decrease this limit. Thus we expect that any dielectric saturation is contained within $\sim$ 4Å from the metal surface, i.e. within the compact layer. The ε within the diffuse layer is therefore assumed to be that of bulk water, $61\varepsilon_o$, at a fuel cell operating temperature $T = 353\text{K}$ [11].

2.3.4 Pore Geometry

Pore sizes for ionomer-free catalyst layers have not in general been characterized. One exception is Pt-plated nanoporous gold leaf (Pt-NPGL), where the gold leaf thickness is known and SEM imaging shows the pore sizes after Pt plating [60]. In other cases, only the thickness of the entire catalyst layer is known; as a first assumption we equate thickness with pore length.

Assuming that the support particles (or the Pt particles, in the case of a support free catalyst layer) are closely packed, we can obtain a rough, order-of magnitude estimate of the minimum pore size. With an ideal "hexagonal close packing", the pore size should be $\sim$ 20% of the support particle size; a "simple cubic packing" gives pore sizes that are $\sim$ 40% of support particle sizes.

Generally, support particles are on the order of 30-50nm in diameter while sputtered particles have diameters of $\sim$ 10nm. Thus, we could expect typical UTCL pore

diameters to be 2-20nm.

2.4 Model Solution and Analysis of Results

Generally, the fully coupled set of governing equations must be solved numerically. However, due to the sluggish oxygen reduction, the Poisson-Boltzmann equation is a valid approximation to the PNP equation over the ranges of R, L, η_c, and ϕ^{pzc} considered in this work. As we show below, this approximation allows for an analytical solution for the potential and reactant concentration distributions, and the separation of Γ into factors due to electrostatic and oxygen transport effects.

2.4.1 Electrostatic Effects: The Poisson Boltzmann Problem

At the limit of small current density, the PNP equations can be simplified by setting the flux term to zero, which gives the PB equation. Due to the sluggish oxygen reduction reaction, this is usually a valid simplification within the range of parameters studied. In Sec. 2.4.2, we evaluate this approximation by comparison to the numerical solution of the fully coupled system of governing equations. This approach allows us to solve for the potential distribution independently of proton concentration, and isolate the electrostatic effects on Γ from the effects due to limited oxygen transport. The PB equation is

$$\nabla^2\phi = -\frac{c_{\mathrm{H}^+}F}{\varepsilon}\exp(-k[\phi-\phi_o]) \tag{2.22}$$

The proton concentration follows a Boltzmann distribution,

$$c_{\mathrm{H}^+} = c^o_{\mathrm{H}^+}\exp\left(-k[\phi-\phi_o]\right)\ , \tag{2.23}$$

which reduces the effectiveness factor Eq. (2.18) to

$$\Gamma = \int_0^L \left(\frac{c_{O_2}}{c^o_{O_2}} \right) \exp\left[k(\alpha - \gamma_{H^+})(\phi(R,z) - \phi_o) \right] dz \, . \tag{2.24}$$

In the considered geometry, there should be a Donnan potential difference at the PEM|UTCL interface; beyond this region, the problem varies only in the radial direction, r. The extent of this region is around the Debye length, $\lambda_D = \sqrt{\varepsilon R_g T / F^2 c^o_{H^+}} \sim 4$Å. Neglecting this small decay region, i.e., setting $\partial_{zz}\phi = 0$ in Eq. (2.22), we reduce the electrostatic problem to one dimension only.

Since $\phi(R,z)$ no longer has an axial dependence, the effectiveness factor from Eq. (2.24) can be separated into electrostatic and oxygen transport components, $\Gamma = \Gamma_{elec}\Gamma_{O_2}$, where

$$\Gamma_{elec} = \exp\left[k\left(\alpha - \gamma\right)\left(\phi(R,z) - \phi_o\right) \right], \quad \Gamma_{O_2} = \int_0^L \left(\frac{c_{O_2}(R,z)}{c^o_{O_2}} \right) dz. \tag{2.25}$$

With a Boltzmann distribution for c_{H^+} (cf. Eq. 2.23), an increase in c_{H^+} is accompanied by a decrease in ϕ. Thus, the increase in j_F (cf. Eq. 2.10) due to an increase in c_{H^+} is partially offset by a decrease in $|\eta(z)|$. As shown in Eq. (2.25), the ORR microscopic paramaters, α and γ, determine the net effect of these competing trends on Γ_{elec}. In their seminal kinetic studies of the oxygen reduction kinetics, Sepa *et al.* [10] determined that $(\alpha - \gamma) = -\frac{1}{2}$, under both Temkin and Langmuirian adsorption conditions. Hence, an increase in $c_{H^+}(R,z)$, with the corresponding decrease in $\phi(R,z)$, has a net positive effect on Γ_{elec}. In other words, an increased proton concentration in the pore always leads to an increased reaction rate.

The 1D, radial Poisson Boltzmann problem has an analytical solution [107–109],

$$\phi - \phi^o = \frac{1}{k} \ln \left[\frac{\left(1 - \Lambda c^c_{H^+} r^2\right)^2 \cdot c^o_{H^+}}{c^c_{H^+}} \right] , \tag{2.26}$$

$$c_{H^+} = \frac{c^c_{H^+}}{(1 - \Lambda c^c_{H^+} r^2)^2} , \tag{2.27}$$

where $\Lambda = {}^{kF}/_{8\varepsilon} = {}^{F^2}/_{8\varepsilon R_g T}$, and $c^c_{H^+}$, the proton concentration at the pore centre, $r = 0$ depends on the boundary condition for potential at the pore wall. Since σ in the 1D case is independent of z, $c^c_{H^+}$, as well as Γ_{elec}, can be found as explicit functions of σ, without assuming any model of the compact region of the double layer. We first examine this more general case in Sec. 2.4.1. To relate Γ_{elec} to the applied electrode potential ϕ^M, a model of the compact region of the double layer is required, as detailed in Sec. 2.4.1.

Electrostatic effectiveness Γ_{elec} as a function of surface charge density σ

For a given σ, Gauss' law gives $\partial_r \phi\big|_{r=R} = \sigma/\varepsilon$. Substituting this boundary condition in Eq. (2.26), we obtain the dependence of $c^c_{H^+}$ on σ and R,

$$c^c_{H^+} = \frac{1}{\Lambda} \frac{\sigma F R}{\sigma F R - 4\varepsilon R_g T}. \tag{2.28}$$

With Eq. (2.26) evaluated at $r = R$, and $c^c_{H^+}$ given by Eq. (2.28), Eq. (2.25) gives the electrostatic effectiveness as a function of σ,

$$\Gamma_{elec} = \left[\frac{\sigma^2}{2 c^o_{H^+} \varepsilon R_g T} \left(1 + \frac{R_c}{R}\right) \right]^{-(\alpha - \gamma_{H^+})} , \tag{2.29}$$

where the σ-dependent critical radius $R_c = {}^{-4\varepsilon R_g T}/_{\sigma F}$ was introduced. σ is restricted to negative values, since it must balance the positive charges of the protons within the pore.

Eq. (2.29) is generally valid where the 1D, radial Poisson-Boltzmann assumption applies. Any functional dependence of σ on ϕ^M could be used in Eq. (2.29) to determine Γ_{elec} as a function of electrode potential ϕ^M. This dependence could be determined from experimental or theoretical studies. In the section that follows, we adopt a simple Stern model of the metal|solution interface.

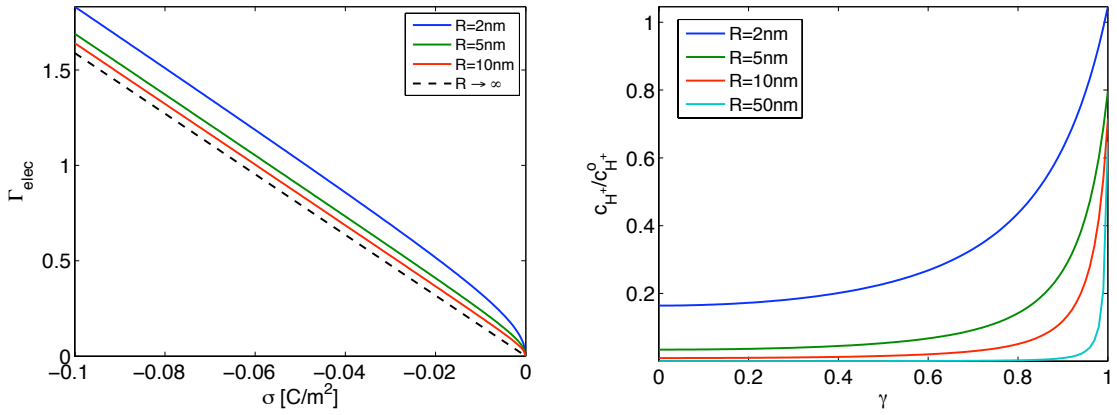

(a) (b)

Figure 2.3: In the 1D Poisson Boltzmann limit: (a) the electrostatic effectiveness Γ_{elec} vs. σ for $R = 2, 5, 10$nm and the limiting case of $R \to \infty$, (b) the normalized proton concentration $c_{H^+}/c^o_{H^+}$ vs. γ for R = 2, 5, 10, 50nm with σ = -0.05 C/m^2. At lower R, double layer overlap and pore wall curvature leads to an enhancement in proton concentration at the pore walls.

Fig. 2.3(a) shows Γ_{elec} vs. σ for R = 2, 5, 10 nm and in the limit $R \to \infty$. As implied by Eq. (2.29), $\Gamma \to 0$ as $\sigma \to 0$, since protons are not drawn into the pore when negative surface charges are not present. In principle, we should consider OH^- from dissocation of water as $\sigma \to 0$, however, we have not dealt with this complication here. The first term of Eq. (2.29) corresponds to Γ in the limit $R \to \infty$. The R_c/R term provides the enhancement in current conversion efficiency due to the confining pore geometry. This term becomes significant when $R \sim R_c$. There are physically intuitive explanations for this enhancement. Where $R \sim R_c$, the negatively charged, curved wall

exhibits an enhanced attractive electrostatic force on nearby protons. Moreover, overlapping electric double layers lead to higher electrostatic repulsion between protons at the pore centre [110]. Both of these factors increase the proton concentration at the pore walls, which gives rise to the enhancement of Γ_{elec}. For a typical $\sigma = -0.05$ C/m^2, R_c = 1.3nm, which approaches the limit of the validity of the continuum approach. However, the influence of this R-dependent term is evident in Fig. 2.3(a) for $R <$ 10nm. Fig. 2.3(b) shows $c_{\mathrm{H}^+}/c^o_{\mathrm{H}^+}$ vs. r/R at σ = -0.05C/m^2 for pores of R = 2, 5, 10, and 50nm; increasingly overlapped double layers and enhanced pore wall concentrations $c_{\mathrm{H}^+}/c^o_{\mathrm{H}^+}$ are seen with decreasing R.

Electrostatic effectiveness Γ_{elec} as a function of ϕ^M

To relate ϕ and Γ_{elec} to the applied potential ϕ^M, we apply the boundary condition given by Eq. (2.17), where $\phi(R,z)$ and $\partial_r\phi\big|_{r=R}$ no longer depend on z. Inserting Eq. (2.26) into Eq. (2.17) gives $c^c_{\mathrm{H}^+}$ as an implicit function of $\phi^M - \phi^{pzc}$,

$$\ln\left[\frac{(1-\Lambda c^c_{\mathrm{H}^+}R^2)^2\cdot c^o_{\mathrm{H}^+}}{c^c_{\mathrm{H}^+}}\right] - \frac{4\varepsilon\Lambda c^c_{\mathrm{H}^+}R}{C_H\left(1-\Lambda c^c_{\mathrm{H}^+}R^2\right)} = k\left(\phi^M-\phi^{pzc}\right)\ . \tag{2.30}$$

With Eqs. (2.25) and (2.26) , $\phi(R,z)-\phi^o$ and $\partial_r\phi\big|_{r=R}$ of Eq. (2.17) can be written in terms of Γ_{elec}, to obtain Γ_{elec} as an implicit function of $\phi^M - \phi^{pzc}$,

$$\frac{\ln\Gamma_{elec}}{\alpha-\gamma_{\mathrm{H}^+}} + \frac{\varepsilon}{C_H R}\left(2-\sqrt{4+\frac{2F^2c^o_{\mathrm{H}^+}R^2\Gamma_{elec}^{-\frac{1}{\alpha-\gamma_{\mathrm{H}^+}}}}{\varepsilon R_g T}}\right) - k(\phi^M-\phi^{pzc}) = 0\ . \tag{2.31}$$

Fig. 2.4 shows the electrostatic effectiveness Γ_{elec} vs. $\phi^M - \phi^{pzc}$ for radii R= 2, 5, 10nm and in the limit $R\to\infty$. σ vs. $\phi^M - \phi^{pzc}$ corresponding to the same pore radii is shown in the inset. In the $\alpha-\gamma = -\frac{1}{2}$ case, there are explicit, physically intuitive relations between Γ_{elec} and $\phi^M - \phi^{pzc}$, as well as a separation of the R, $\phi^M - \phi^{pzc}$, and

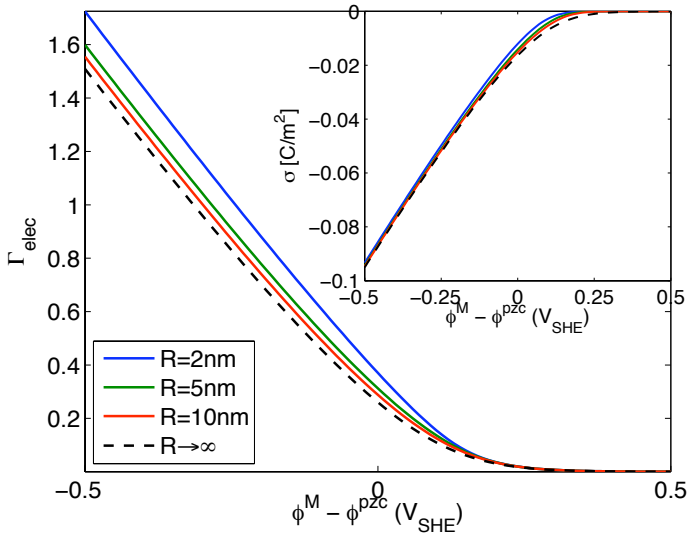

Figure 2.4: In the Poisson-Boltzmann limit, electrostatic effectiveness Γ_{elec} vs. $\phi^M - \phi^{pzc}$ for $R = 2$, 5, 10nm, and the limiting case of $R \to \infty$. Inset: corresponding surface charge density σ vs. $\phi^M - \phi^{pzc}$.

C_H contributions to Γ_{elec}.

Where $\Gamma_{elec} \sim 1$, Eq. (2.31) reduces to

$$\Gamma_{elec} \approx \left(2 + \frac{F}{C_H}\sqrt{\frac{2\varepsilon c^o_{H^+}}{R_g T}}\right)^{-1} \left[\frac{2\varepsilon}{C_H R} - k(\phi^M - \phi^{pzc}) + 2\right] . \tag{2.32}$$

The first term within the second bracket in Eq. (2.32) is $\propto 1/R$ and gives a slight enhancement in Γ_{elec} for small $R < 10$nm; we attribute this to pore curvature and double layer overlap, as was discussed for $\Gamma_{elec}(\sigma)$ (Eq. 2.29). The second term shows linear dependence on $\phi^M - \phi^{pzc}$. The lower the ϕ^M is relative to ϕ^{pzc}, the more negative the surface charge density, and, as expected from the trend in Γ_{elec} vs. σ, the higher the Γ_{elec}. These two features are evident in the $\Gamma \sim 1$ region of Fig. 2.4. The dependence of Γ_{elec} on C_H is contained in the first term, a constant factor. An increase in C_H increases this term, which means Γ_{elec} increases faster with decreasing ϕ^M; this is consistent with

the physical interpretation of more extensive pore wall charging with a given shift in potential, when C_H is higher.

As $\Gamma \to 0$, Eq. (2.31) reduces to

$$\Gamma_{elec} \approx \exp\left[-\frac{k}{2}\left(\phi^M - \phi^{pzc}\right)\right] . \tag{2.33}$$

Γ_{elec} at this limit can be understood by considering the potential distribution at small σ. For $\sigma \sim 0$, there is little drop in potential within the compact layer; the shift in ϕ^M from ϕ^{pzc} should be reflected mostly in potential changes in the diffuse layer

$$\phi^M - \phi^{pzc} \approx \phi(R,z) - \phi^o. \tag{2.34}$$

Substituting Eq. (2.34) in (2.25) gives Eq. (2.33). The exponential dependence of Γ_{elec} on ϕ^M as $\Gamma_{elec} \to 0$ is visible in Fig. 2.4.

Eq. (2.33) also implies that Γ_{elec}, and thus c_{H^+}, both asymptotically approach zero as ϕ^M increases. Our present approach, where c_{H^+} in the channel is determined only by the supply of excess protons from the PEM boundary and their electrostatic interaction with the charged channel walls, is expected to fail when c_{H^+} approaches $\sim 10^{-7}$M. At such low c_{H^+}, protons and hydroxide anions from the dissociation of water should be accounted for. However, since such low c_{H^+} give rise to essentially a negligible Γ_{elec}, we do not consider this effect further in the present work.

Fig. 2.4 and limiting cases Eq. (2.32) and Eq. (2.33) illustrate the importance of ϕ^{pzc} to the overall pore performance. Roughly proportional to the metal work function, [90], ϕ^{pzc} is a measure of the propensity of a given metal|solution interface to retain electrons at its surface. For a given operating electrode potential ϕ^M, higher ϕ^{pzc} corresponds to more negative σ and higher Γ_{elec}. In the linear, $\Gamma_{elec} \sim 1$ regime, (Eq. 2.32), a shift in ϕ^{pzc} by 0.3V would shift Γ_{elec} by ~ 0.8. This implies that even an inactive catalyst support may exert a considerable influence on Γ_{elec} through its surface charge. Since

ϕ^{pzc} has been shown to exhibit particle size [97,111] and roughness dependences [100], this finding may have implications for the choice of Pt particle size and shape as well.

Eqs. (2.29) and (2.31) and Figs. 2.3(a) and 2.4 imply that Γ_{elec} increases indefinitely as σ and ϕ^M decreases. However, the assumption of the PEM as an infinite reservoir of protons may no longer be accurate as Γ_{elec} increases well beyond 1. At high enough current densities, transport limitations will also affect the overall Γ. This is addressed in Sec. 2.4.2.

Local Oxide Coverage

As discussed in Sec. 2.3.1, the kinetic parameters γ and α shift at the onset of oxide coverage. Because coverages of oxide species depend on both overpotential and pH, one would normally expect the local oxide coverage within the pore to vary from that at the pore|PEM interface; hence γ and α may vary locally within the pore, affecting $j(z)$. However, this is not the case in the Poisson-Boltzmann limit. From [10], we have the following relation for oxide coverage, verified experimentally for pH in the range 0-14 and at relevant electrode potentials,

$$\theta = \kappa\left(\frac{2.3}{k}\mathrm{pH} + \eta_c\right) + C \tag{2.35}$$

where κ and C are constants. This relation can be derived by assuming the water splitting reaction to be at equilibrium. Applying $\mathrm{pH}(R,z) = \mathrm{pH}^o + {}^{k}/_{2.3}(\phi(R,z) - \phi^o)$ (Eq. 2.23), and Eq. (2.13) for $\eta(z)$, the local coverage $\theta(z)$ equals that at the PEM|metal interface, θ^o:

$$\theta(z) = \kappa\left[\frac{2.3}{k}\mathrm{pH}(R,z) + \eta(z)\right] + C \tag{2.36}$$

$$= \kappa\left[\frac{2.3}{k}\mathrm{pH}^o + \eta_c\right] + C = \theta^o \tag{2.37}$$

Thus, the effect of an increase in pH away from the PEM is exactly compensated by a drop in local overpotential, so that no net change in coverage occurs. In other words, the applied cathode overpotential η_c alone determines whether the kinetics within the pore are in the high (Langmuirian adsorption) or low (Temkin adsorption) current density regime.

2.4.2 Oxygen Transport Limitations

The oxygen penetration depth in flooded UTCLs should be considerably reduced from that in conventional CLs, which contain open gas pores. Where the Poisson-Boltzmann limit applies, the oxygen diffusion problem can be decoupled from the electrostatic one, i.e., Γ can be reduced as in Eq. (2.25). We solve the Laplace equation, Eq, (2.4), with boundary conditions

$$\partial_z c_{\mathrm{O}_2}\big|_{(r,0)} = 0, \quad c_{\mathrm{O}_2}(r,L) = c^o_{\mathrm{O}_2} \tag{2.38}$$

$$\partial_r c_{\mathrm{O}_2}\big|_{(R,z)} = -\Omega c_{\mathrm{O}_2}(R,z), \tag{2.39}$$

where $\Omega = j_{ideal}\Gamma_{elec}/4c^o_{\mathrm{O}_2}D_{\mathrm{O}_2}F$, j_{ideal} is given by Eq. (2.18), and Γ_{elec} by Eq. (2.31). By separation of variables,

$$c_{\mathrm{O}_2}(r,z) = 2c^o_{\mathrm{O}_2}\sum_{k=1}^{\infty}\frac{R\Omega}{\lambda_k^2+(R\Omega)^2}\frac{J_o\left(\frac{\lambda_k r}{R}\right)}{J_o(\lambda_k)}\frac{\cosh\left(\frac{\lambda_k z}{R}\right)}{\cosh\left(\frac{\lambda_k L}{R}\right)}, \tag{2.40}$$

where J_i is the Bessel function of order i, and λ_k are the roots of

$$R\Omega J_o(\lambda_k) = \lambda_k J_1(\lambda_k). \tag{2.41}$$

The oxygen transport contribution to the effectiveness factor is then

$$\Gamma_{O_2} = \frac{\int_0^L c_{O_2}(R,z)dz}{c^o_{O_2} L} = \frac{2R}{L}\sum_{k=1}^{\infty} \frac{R\Omega}{\lambda_k[\lambda_k^2 + (R\Omega)^2]} \tanh\left(\frac{\lambda_k L}{R}\right) \tag{2.42}$$

To evaluate the validity of this analytical approximation, it was compared to the full numerical solution. The general problem requires the simultaneous solution of the PNP equations and the Laplace equation with the boundary conditions stated in Sec (2.2.1). This was performed using COMSOL Multiphysics.

The oxygen distribution within the pore depends on R, L, η_c, and σ, determined by ϕ^{pzc}; the η_c and ϕ^{pzc} dependence of $c_{O_2}(r,z)$ is contained in the sink term Ω. In Figs. 4(a) - (c), we show the impact of varying R, L, and ϕ^{pzc} on Γ as a function of η_c, for a reference set of parameters ϕ^{pzc} = 0.7V_{SHE}, R = 5nm, and L =100nm. To highlight the effect of oxygen diffusion, Γ_{elec} is also shown as a dashed black line; the deviations from Γ_{elec} indicate the onset of oxygen transport limitations. The analytical approximation, $\Gamma \approx \Gamma_{elec}\Gamma_{O_2}$, is shown as solid lines, and the numerical solution for Γ obtained from the full set of governing equations is shown as points.

Fig. 2.5(a) shows the impact of L on Γ. Γ vs. η_c curves are shown for L = 20nm, 100nm, 1μm, ϕ^{pzc} = 0.7V_{SHE}, and R = 5nm. As expected, higher L show more severe oxygen transport limitations; the inset shows corresponding normalized oxygen concentration profiles $c_{O_2}/c^o_{O_2}$ at $r = R$ vs. the dimensionless coordinate z/L at η_c = -0.6V. In the case of L = 1μm, the interplay of increasing proton concentrations and oxygen depletion leads to a maximum in Γ vs. η_c.

Fig. 2.5(b) shows the impact of R on Γ. Γ vs. η_c is plotted for R = 2, 5, 20nm. At a given η_c, one would normally expect that increasing R would lead to lower diffusion limitations and hence a higher Γ. However, because of the slight enhancement in Γ_{elec} from double layer overlap, the optimal R for a pore of given L and $\phi - \phi^{pzc}$ varies with the operating potential.

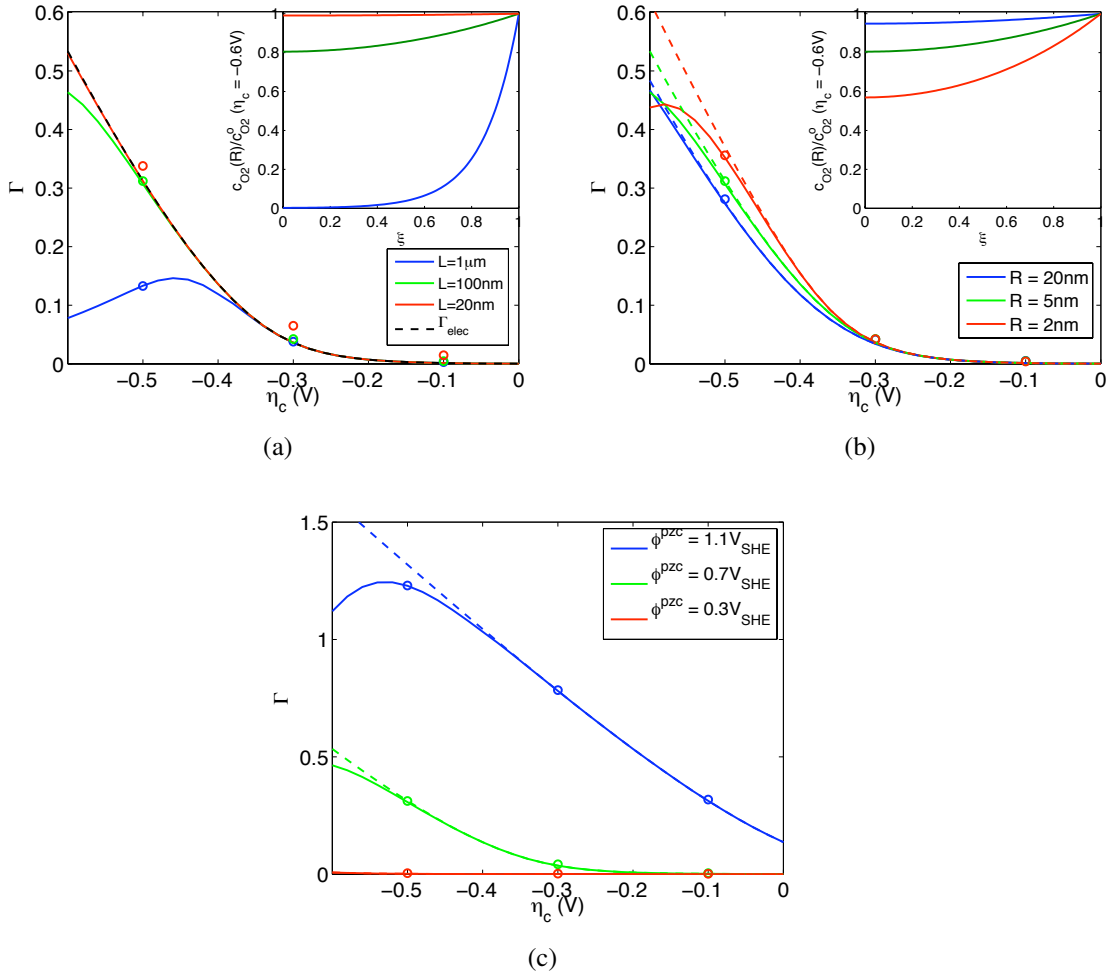

Figure 2.5: Γ vs. η_c. Points correspond to numerically calculated Γ's and lines to the analytical approximation $\Gamma = \Gamma_{elec}\Gamma_{O_2}$. To show the impact of Γ_{O_2}, Γ_{elec} is shown as a dotted line. (a) Curves for ϕ^{pzc} = 0.7V$_{\text{SHE}}$, R = 5nm, L = 20nm, 100nm, 1μm. Inset: corresponding $c_{O_2}/c^o_{O_2}$ at η_c = -0.6V. (b) Curves for Γ vs. η_c for pores of R =2, 5, 20nm, L = 100nm, at ϕ^{pzc} = 0.7V$_{\text{SHE}}$. Inset: corresponding $c_{O_2}/c^o_{O_2}$ at η_c = -0.6V. (c) Curves for R = 5nm, L = 100nm, at ϕ^{pzc} = 1.1, 0.7, and 0.3V$_{\text{SHE}}$.

To illustrate the impact of ϕ^{pzc}, Γ vs. η_c is plotted in Fig. 2.5(c) for pores with R = 5nm, L = 100nm, and ϕ^{pzc} = 1.1, 0.7, and 0.3V_{SHE}. As discussed previously, ϕ^{pzc} exerts a major effect on Γ. Generally, higher ϕ^{pzc} leads to a higher Γ_{elec} and hence higher overall Γ.

Generally, the approximation $\Gamma \approx \Gamma_{elec}\Gamma_{O_2}$ is rather accurate for the conditions evaluated. In the case of Fig. 2.5(a) for the shortest pore with L= 20 nm, the slightly enhanced numerical value of Γ arises from the current densities within the PEM|UTCL double layer, the Donnan "decay region" from the PEM that has been neglected in the analytical approximation; where L is close to the extent of the decay region, the decay region may contribute to a perceptible fraction of the overall current density. This correction, however, does not change the general trends predicted by the analytical approximation.

2.4.3 Model Evaluation and Implications

Model results presented in previous sections should be evaluated by systematic experimentation. Proton concentration in a conductive nanoporous membrane consisting of water-filled nanopores, as considered in our model, is expected to be a function of $\phi^M - \phi^{pzc}$. The variation of proton concentration in such nanoporous metal matrices could be probed by proton conductivity measurements [112] and impedance spectroscopy, as discussed in the next chapter. In principle, the tunability of the ion conductivity of porous gold matrices with $\phi^M - \phi^{pzc}$ has already been demonstrated in Refs. [77,113]. Exploiting this phenomenon for the design of nanoporous materials with both tunable proton conductivity and electrocatalytic properties has not been explored.

An obligatory consistency check of the presented model is the comparison with available experimental polarization curves. The scale-up of the single pore model to the relation between ϕ^M and the total Faradaic current density produced by the UTCL, j_{CL}, requires knowledge of the pore size and length distributions, electrochemically active

surface area (ECSA), ϕ^{pzc}, membrane resistance R_{PEM}, fraction of water-filled active pores (if larger pores are present), and rigorously determined ORR kinetic parameters (j^o and transition overpotential, η_c^T) for the Pt/support species present. Moreover, pore tortuosity, which was not considered in this work, should be accounted for.

While a rigorous homogenization of the current model has been performed by Schmuck and Berg [114], it relies on a simple Gauss' law surface charge density boundary condition, which does not relate charge to the applied metal potential. We take a simplified scale-up approach to examine general trends in the polarization curves predicted by the current model. We assume that the UTCL is comprised of straight cylindrical water-filled pores with fixed R and L. We consider ϕ^{pzc} as an adjustable parameter. The relation between j_{CL} and IR-corrected electrode potential ϕ^M is thus given by

$$j_{CL}(\eta_c) = j_{ideal}(\eta_c) \cdot \Gamma(\phi^M - \phi^{pzc}) \cdot \text{ECSA} \,, \tag{2.43}$$

where ϕ^M refers to the IR-corrected metal potential, and j_{ideal} is given by Eq. (2.18) with $\eta_c = \phi^M - \phi^M_{eq}$, and $\Gamma = \Gamma_{elec}\Gamma_{O_2}$ from Eqs. (2.31) and (2.42). The applied electrode potential is

$$E(j_{CL}) = \phi^M_{eq} + \eta_c - j_{CL}(\eta_c)R_{PEM} + \eta_{other} \tag{2.44}$$

where $j_{CL}(\eta_c)R_{PEM}$ gives the IR losses, and η_{other} includes anode overpotentials, and electrode and contact resistances. We neglect η_{other} in the following calculations, as well as any mass transport losses in the diffusion media.

We have evaluated polarization curves of two UTCLs that have been characterized in greater detail than others, that is, Pt-plated nanoporous gold leaf (Pt-NPGL) [60] and 3M's Pt nanostructured thin film catalyst layer (3M Pt-NSTF) [56]. In Pt-NPGL, the unknown parameters are R_{PEM} and ϕ^{pzc}; other parameters can be estimated from available characterization data. In 3M-NSTF, the most uncertain parameters are the pore radius R and ϕ^{pzc}. To account for the impact that particle size, morphology, and/or

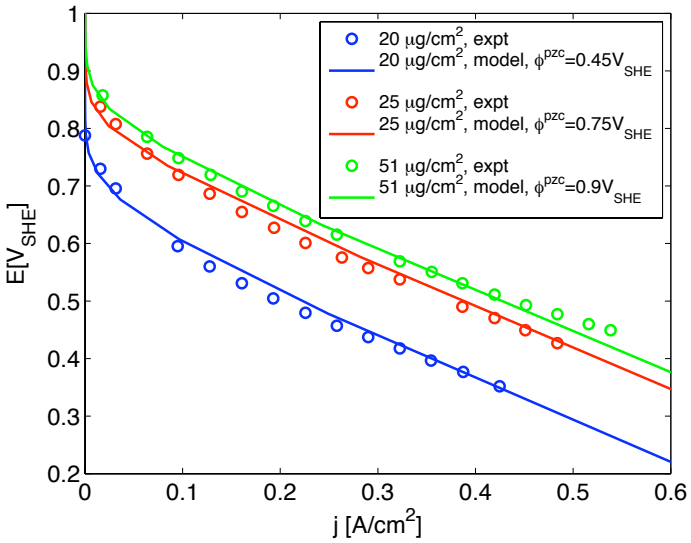

Figure 2.6: Pt-NPGL polarization curves at loadings 20, 25, 51 μg/cm^2; points indicate experimental values from [60] and lines model curves. Parameters used to calculate model curves are listed in Table 2.1.

catalyst support may have on the ORR rates of these UTCLs, kinetic parameters used in calculating the model parameters were taken from fits to rotating disk electrode (RDE) data. For Pt-NSTF UTCL, we used the RDE data from Ref. [115]. These are then scaled to the operating oxygen pressures and Nafion proton concentration using Eq. (2.21). An activation energy of $\sim$ 42kJ/mol for the rate determining step in ORR was used to scale the j^o up to the UTCL characterization temperatures, as determined in Ref. [116] for Pt(111), (100), and (110). Table 2.1 provides the parameters used in calculating model polarization curves.

Fig. 2.6 compares model and experimental polarization data for Pt-NPGL layers at Pt loadings of 20, 25, 51 μg/cm^2. Pt-NPGL with loadings below 20μg/cm^2 were not considered, because they required high overpotentials at which H adsorption and H_2O_2 production may have set in. A 25μg_{Pt}/cm^2 loading corresponded to a Pt film of $\sim$ 2nm thickness, and the radius of the unplated pore was $\sim$ 7.5nm [60]; R values for

Parameter	**Pt-NPGL** [60]	**3M Pt-NSTF** [56]
j^o, low cd region	2.9×10^{-8} A cm^{-2}	2.3×10^{-6} A cm^{-2}
j^o, high cd region	5.8×10^{-5} A cm^{-2}	2.4×10^{-4} A cm^{-2}
η_c^T	-0.46V	-0.28V
$p^o_{O_2}$	3.4 bar	1 bar
$c^o_{O_2}$	2.1×10^{-3} M	6.4×10^{-4} M
T	348K	348K
R	$20\mu g_{Pt}$/cm^2: 5.9nm	20nm
	$25\mu g_{Pt}$/cm^2: 5.5nm	
	$51\mu g_{Pt}$/cm^2: 3.5nm	
L	100nm	270nm
ECSA	$20\mu g_{Pt}$/cm^2: 9.7cm$^2_{Pt}$/cm$^2_{geo}$	13.1cm$^2_{Pt}$/cm$^2_{geo}$
	$25\mu g_{Pt}$/cm^2: 14.6cm$^2_{Pt}$/cm$^2_{geo}$	
	$51\mu g_{Pt}$/cm^2: 16.8cm$^2_{Pt}$/cm$^2_{geo}$	
R_{PEM}	0.65 Ωcm^2 (fitted)	0.065Ωcm^2
ϕ^{pzc} (fitted)	$20\mu g_{Pt}$/cm^2: 0.45V	0.7V
	$25\mu g_{Pt}$/cm^2: 0.75V	
	$51\mu g_{Pt}$/cm^2: 0.9V	

Table 2.1: Parameters used in calculating model polarization curves. j^o's and η_c^T were obtained by fitting room temperature RDE data from Refs. [117] and [118], corrected for operating $p^o_{O_2}$ and $c^o_{H^+}$ using Eq. (2.21) and T using ΔH = 42kJ/mol. For Pt-NPGL, a $25\mu g_{Pt}$/cm^2 loading had a Pt film of $\sim$ 2nm thick, and the radius of the unplated pore was $\sim$ 7.5m [60]; values of R for the other loadings were scaled proportionally. The ECSAs were determined from Fig. 8 in [60], i.e. ECSA = specific active area $\times$ Pt loading. In both UTCLs, L was assumed to be the thickness of the UTCL.

the other loadings were scaled proportionally. The ECSA also shifts with loading, and we determined ECSA values from Fig. 8 of Ref. [60] (i.e., ECSA = specific active area $\times$ Pt loading). Since the membrane resistance was not measured, it was set to 0.6Ωcm^2 for all three curves to fit the "mixed kinetic/Ohmic region" at higher overpotentials[2]. The downward shifts in the curves with decreasing loading were reproducible from changes in the ϕ^{pzc} (0.9 to 0.45V$_{SHE}$). ϕ^{pzc} values of Pt and Au determined via the immersion method were $\sim$ 1.1V and and 0.53V respectively [102]; this is consistent

[2]This is a rather high value for Nafion, which suggests that there may have been an issue with keeping the membrane humidified during cell tests.

with the decrease in the fitted ϕ^{pzc} towards approximately the ϕ^{pzc} of Au as the Pt loading decreases.

Normally, the electrostatic effect of shifting ϕ^{pzc} is not considered, and the shifts in the curves would be attributed only to a kinetic effect, i.e., variations in the exchange current density, determined by elementary ORR processes. The downward shift in the polarization curve induced by the change in ϕ^{pzc} from 0.9 to 0.45V_{SHE} can be reproduced alternatively by a reduction in exchange current density of 2 orders of magnitude. To evaluate the contributions from kinetic and electrostatic effects, we require a detailed understanding of the Pt-NPGL electronic structure, which can be affected by both the Au support and the island structure of the Pt in Pt-NPGLs that forms at Pt loadings $>$ 25μg/cm^2.

Fig. 2.7(a) shows the polarization curve calculated for Pt-NSTF, and data from Ref. [56]. The pore radius R is not known, so it was assumed to be 20nm, on the scale of the whisker size. A value of ϕ^{pzc} = 0.7V_{SHE} gave a reasonable fit of the data; the divergence from the model curve at high current densities is attributed to GDL flooding. The inset shows the corresponding dependence of Γ vs. E. As can be seen, values of Γ lie significantly below 1, with a maximum of $\Gamma \approx 0.15$ at $E \approx 0.75V_{SHE}$. The Pt effectiveness in these layers remains quite low due to a combination of the relatively low value of ϕ^{pzc}, which diminishes the electrostatic effectiveness, and the relatively high thickness $>$ 250nm, which leads to severe oxygen depletion effects at $E < 0.8V_{SHE}$. There are thus reserves for improvements. However, the overall current densities turn out to be rather high, due to the high exchange current densities of the Pt whiskerettes shown in Table 1. The corresponding proton concentration at the reaction plane, shown as pH vs. E in Fig. 2.7(b), is significantly lower than proton concentrations in ionomer-impregnated catalyst layers; in particular, proton concentrations at high potentials $E > 0.9V_{SHE}$ are reduced by several orders of magnitude. This observation would be consistent with extremely low rates of Pt dissolution found in Pt-NSTF if

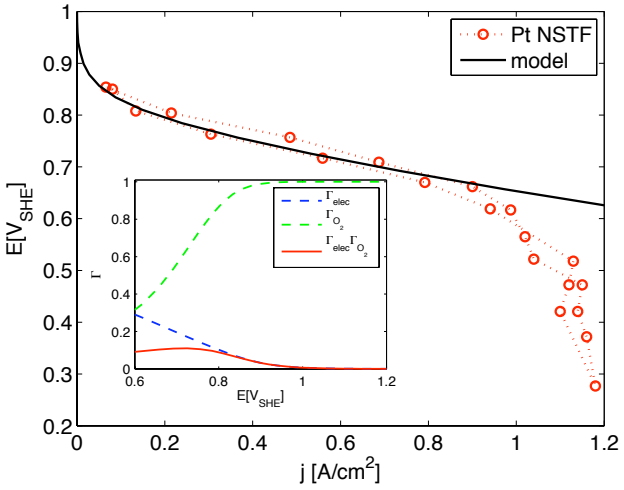

(a)

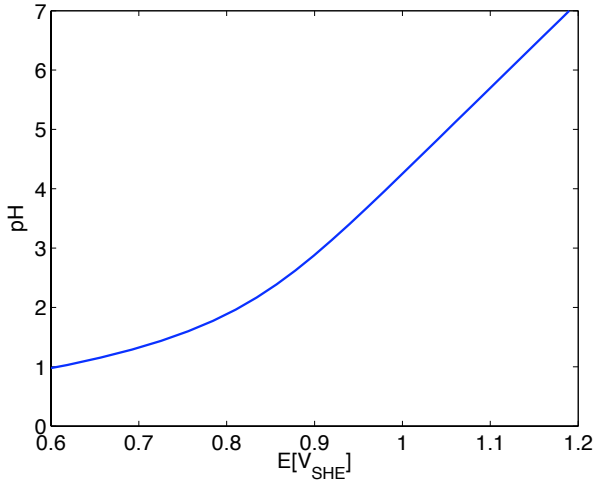

(b)

Figure 2.7: (a) Polarization curve for 3M-NSTF. Lines correspond to model calculations, circles to experimental data from Ref. [56]. Parameters used to calculate model curves are listed in Table 2.1. Inset: corresponding effectiveness factors Γ_{elec}, Γ_{O_2}, and $\Gamma_{elec}\Gamma_{O_2}$. (b) 3M-NSTF: pH at the reaction plane, $r = R$, vs. non-IR-corrected electrode potential E.

a chemical pathway of Pt oxide dissolution prevails [56, 119].

2.5 Summary

We presented a single pore model of oxygen reduction in a water-filled nanopore with charged, metal pore walls. The electrostatic interaction between protons at the PEM and the metal surface charge determine the distributions of protons and electrostatic potential in the pore. These phenomena distinguish the present pore model from the gas- and electrolyte-filled single pore models pioneered by Markin [120], Srinivasan [121], and de Levie [122].

With the explicit consideration of the pore wall surface charge, the potential of zero charge, ϕ^{pzc}, of the metal|solution interface is the most crucial parameter determining pore performance. The ϕ^{pzc} can be considered as a measure of the propensity of the metal|solution interface to retain electronic charge. The lower the applied potential relative to the potential of zero charge, i.e. the more negative the difference $\phi^{M} - \phi^{pzc}$, the more negative the surface charge, and the higher the proton concentration and current density produced at the pore walls. Thus, at a given operating electrode potential ϕ^{M}, a higher ϕ^{pzc} is desirable for increasing the overall current density produced by a UTCL. UTCLs may outperform conventional catalyst layers provided that the ϕ^{pzc} is sufficiently large.

With moderate $\phi^{pzc} \sim 0.7\mathrm{V_{SHE}}$, proton concentrations in UTCL are several orders of magnitude smaller than those in conventional, ionomer-impregnated catalyst layers. A possible benefit of such a reduced proton concentration could be the correspondingly reduced rate of Pt oxide dissolution via a chemical mechanism. If this mechanism prevails, Pt dissolution rates in water-filled nanochannels should be vanishingly small for $\phi^{M} > \phi^{pzc}$. Variation of ϕ^{pzc} could be a viable route to fine-tune UTCLs in view of both high ORR activity and a low Pt dissolution rate. Where ϕ^{pzc} is high (i.e. $\phi^{M} -$

$\phi^{pzc} < 0$), a high Helmholtz capacitance C_H would further improve the Pt effectiveness.

Increasing absolute local overpotentials $|\eta|$ corresponds to increasing proton concentrations. The ORR transfer coefficient and proton reaction order determine the net impact of these competing trends on the reaction rate. Since $\alpha - \gamma = -\frac{1}{2}$ from kinetic ORR data, the net effect of an increased proton concentration is always an increased reaction rate.

Oxygen penetration depth in UTCLs is generally reduced from that in conventional CLs with significant gas porosity, since oxygen in UTCLs diffuses through water flooded pores. The limiting pore length is around 200nm for a reasonable set of parameters.

Usually, macrohomogeneous catalyst layer models assume that the metal phase acts simply as a current sink. While this may be a valid assumption in ionomer-impregnated catalyst layers, where proton concentrations are relatively fixed, our model suggests that anion-free, water-filled pores require the consideration of the interaction between protons and metal surface charge, since it plays a crucial role in determining overall pore effectiveness. The implication for UTCL design is that catalyst layer materials should be tuned for not only their intrinsic mass activities but also their metal|solution interfacial properties, i.e. the potential of zero charge, ϕ^{pzc}, and Helmholtz capacitance, C_H, or, more generally, the relation between σ and ϕ^M. It is expected that particle size, shape, and surface roughness may influence ϕ^{pzc}; catalytically inactive support materials may exert a considerable impact on performance through their surface charge. Future theoretical studies of the impact of electronic structure, particle size, and oxide species adsorption on ϕ^{pzc} can be invaluable to UTCL catalyst and support materials design.

Chapter 3

Single Pore Model of UTCLs: Impedance Variant

3.1 Introduction

In this chapter, we present the impedance variant of the single pore model of oxygen reduction in UTCLs [123] [1]. In the steady state model discussed in Chapter 2, polarization curves were output for a consistency check with experiment. However, polarization curves are relatively featureless; they do not allow for the separation of the effects of surface charging and intrinsic catalyst activity on the overall current density. Impedance spectra, on the other hand, can separate processes that occur on different timescales.

The governing equations are time–dependent, transport equations in two spatial dimensions. With simplifying assumptions, we reduce the model to one dimension, and derive analytical impedance expressions with intuitive equivalent circuit representations in various limits.

[1] This chapter reproduces in revised form material from Ref. [123], with permission from the Electrochemical Society.

In what follows, we formulate the impedance model, derive and discuss the analytical solutions and equivalent circuit representations, and discuss its diagnostic capabilities for UTCL characterization.

3.2 Model Formulation

We deal with the same model system as in the steady state model, shown in Fig. 2.1. Since our focus is on the bulk UTCL response, we neglect the electric double layer at the PEM|UTCL interface. An explicit description of this interface would require accounting for PEM structure and processes in the model, which is beyond the scope of the current work. As discussed in Sec. 3.3.5, we can as a first step include this interface by an effective capacitance in parallel with the pore response.

Governing Transport Equations

The governing equations are the time-dependent versions of those in the steady state model, i.e. PNP equations for proton transport and Fick's Law for oxygen diffusion,

$$\partial_t c_{\mathrm{H}^+} = -\nabla\cdot\mathbf{N}_{\mathrm{H}^+},\ \mathbf{N}_{\mathrm{H}^+} = -D_{\mathrm{H}^+}\left(\nabla c_{\mathrm{H}^+} + k c_{\mathrm{H}^+}\nabla\phi\right)\ , \tag{3.1}$$

$$\nabla^2\phi = -\frac{c_{\mathrm{H}^+}F}{\varepsilon}\ , \tag{3.2}$$

$$\partial_t c_{\mathrm{O}_2} = -\nabla\cdot\mathbf{N}_{\mathrm{O}_2},\ \mathbf{N}_{\mathrm{O}_2} = -D_{\mathrm{O}_2}\nabla c_{\mathrm{O}_2}\ . \tag{3.3}$$

Parameters, variables, and physical constants are shown in Table 2.

Boundary Conditions

At $z = L$ and $r = R$, we assume identical boundary conditions to the steady state model, Eqs. (2.7, 2.8) and Eqs. (2.9, 2.10, 2.13, 2.17), where a Stern model of the electric double layer is used to relate ϕ^M and σ.

The impedance response includes Faradaic and charging currents. Neglecting adsorption pseudocapacitances, the capacitive current density is given by

$$j_C = \partial_t \sigma \, . \tag{3.4}$$

As we focus on the bulk response of the pore, we set the $z = 0$ boundary to the plane right outside the PEM|UTCL double layer. Assuming transport limitations in this thin interfacial layer to be negligible, the potential and concentration distribution in this plane correspond to a Poisson-Boltzmann distribution in a cylindrical pore, Eqs. (2.26, 2.27). Assuming there is no oxygen flux out into the PEM, the boundary condition for oxygen is given by Eq. (2.6).

Linearization of transient response

We assume a small applied potential (or current) modulation so that the transient response is linear. In response to a harmonic perturbation of the applied potential, $\phi^M = \overline{\phi}^M + e^{i\omega t}\delta\phi^M$, all variables can be written in the form $x = \overline{x} + e^{i\omega t}\delta x$, with higher order terms discarded. The overbar "–" refers to a steady state variable and δx indicates the complex amplitude of the perturbation signal, which contains phase shift information. We consider steady state and transient parts separately, and solve for $\delta\phi$, δc_{H^+} and δc_{O_2} [124].

The linearized transient governing equations are

$$i\omega\delta c_{H^+} = -\nabla\cdot\delta\mathbf{N}_{H^+}, \;\; \delta\mathbf{N}_{H^+} = -D_{H^+}(\nabla\delta c_{H^+} + \overline{c}_{H^+}k\nabla\delta\phi + \delta c_{H^+}k\nabla\overline{\phi}) \tag{3.5}$$

$$\nabla^2\delta\phi = -\frac{\delta c_{H^+}F}{\varepsilon} \tag{3.6}$$

$$i\omega\delta c_{O_2} = -\nabla\cdot\delta\mathbf{N}_{O_2}, \;\; \delta\mathbf{N}_{O_2} = -D_{O_2}\nabla\delta c_{O_2} \, . \tag{3.7}$$

The boundary conditions are

$$\partial_z \delta\phi = 0,\ \partial_z \delta c_{\mathrm{H}^+} = 0,\ \delta c_{\mathrm{O}_2} = 0, \quad \text{at } z = L, \tag{3.8}$$

and

$$\varepsilon \partial_r \delta\phi = C_H \left(\delta\phi^M - \delta\phi\right) \tag{3.9}$$

$$\delta N_{\mathrm{H}^+,r} = -\frac{\delta j_F}{F},\ \delta N_{\mathrm{O}_2,r} = -\frac{\delta j_F}{4F}, \tag{3.10}$$

$$\delta j_F = \bar{j}_F \left(-\alpha k \left[\delta\phi^M - \delta\phi\right] + \gamma \frac{\delta c_{\mathrm{H}^+}}{\bar{c}_{\mathrm{H}^+}} + \frac{\delta c_{\mathrm{O}_2}}{\bar{c}_{\mathrm{O}_2}}\right) \tag{3.11}$$

at $r = R$.

At $z = 0$, the boundary condition for oxygen is

$$\partial_z \delta c_{\mathrm{O}_2} = 0. \tag{3.12}$$

Assuming an infinitesimally thin PEM|UTCL interface, proton concentration and potential at $z = 0$ should respond instantaneously to $\delta\phi^M$, i.e.

$$\delta\phi = \frac{\partial\bar{\phi}}{\partial\bar{\phi}^M}\cdot\delta\phi^M = \frac{\partial\bar{\phi}}{\partial\Lambda\bar{c}^c_{\mathrm{H}^+}}\cdot\frac{\partial\Lambda\bar{c}^c_{\mathrm{H}^+}}{\partial\bar{\phi}^M}\cdot\delta\phi^M,\ \ \delta c_{\mathrm{H}^+} = \frac{\partial\bar{c}_{\mathrm{H}^+}}{\partial\bar{\phi}^M}\cdot\delta\phi^M = \frac{\partial\bar{c}_{\mathrm{H}^+}}{\partial\Lambda\bar{c}^c_{\mathrm{H}^+}}\cdot\frac{\partial\Lambda\bar{c}^c_{\mathrm{H}^+}}{\partial\bar{\phi}^M}\cdot\delta\phi^M\,, \tag{3.13}$$

where by differentiation of Eqs (2.26, 2.27, 2.30), the partial derivatives above are

$$\frac{\partial\Lambda\bar{c}^c_{\mathrm{H}^+}}{\partial\bar{\phi}^M} = \frac{k}{R^2}\cdot\frac{(1-\Lambda\bar{c}^c_{\mathrm{H}^+}R^2)^2}{\Lambda\bar{c}^c_{\mathrm{H}^+}R^2 - 1/(\Lambda\bar{c}^c_{\mathrm{H}^+}R^2) - 4\varepsilon/C_H R}, \tag{3.14}$$

$$\frac{\partial\bar{\phi}}{\partial\Lambda\bar{c}^c_{\mathrm{H}^+}} = -\frac{1}{k\Lambda\bar{c}^c_{\mathrm{H}^+}}\cdot\frac{1+\Lambda\bar{c}^c_{\mathrm{H}^+}r^2}{1-\Lambda\bar{c}^c_{\mathrm{H}^+}r^2}\,, \tag{3.15}$$

$$\frac{\partial\bar{c}_{\mathrm{H}^+}}{\partial\Lambda\bar{c}^c_{\mathrm{H}^+}} = \frac{1}{\Lambda}\cdot\frac{1+\Lambda\bar{c}^c_{\mathrm{H}^+}r^2}{(1-\Lambda\bar{c}^c_{\mathrm{H}^+}r^2)^3}\,. \tag{3.16}$$

Impedance Response

The impedance response of the pore is

$$Z(\omega) = \frac{1}{2\pi R} \cdot \frac{\delta\phi^M(\omega)}{\int_0^L \delta j(\omega, z) dz}, \tag{3.17}$$

where $\delta j(\omega, z) = \delta j_F(\omega, z) + \delta j_C(\omega, z)$.

One dimensional equation system

The reduction of the full set of governing equations and boundary conditions, Eqs. (3.1-3.17), to a one dimensional, analytically solvable form is detailed in Appendix B. The simplification relies on two assumptions:

1. Pore radii R are small relative to characteristic diffusion lengths, so that reactant distributions in the radial direction do not deviate significantly from equilibrium values. Then, at a given z, c_{O_2} is approximately constant along r, and c_{H^+} and ϕ are approximated by a Poisson-Boltzmann distribution. Proton concentration and potential are then represented by their values at $r = 0$, the pore centre, $c^c_{H^+}(z)$ and $\phi^c(z)$.

2. Steady state proton concentration and potential distributions vary negligibly along z, i.e. $\overline{c}^c_{H^+}$ and $\overline{\phi}^c$ are assumed to be constant. This assumption was shown in Chapter 2 to be usually valid over relevant operating parameter ranges, due to a relatively small proton flux.

As discussed in Sec. 2.4.1, the second assumption allows for a separation of the effectiveness factor into electrostatic and oxygen transport components, $\Gamma \approx \Gamma_{elec}\Gamma_{O_2}$. We define the electrostatic contribution to the current density (i.e. current density obtained

if there are no oxygen transport limitations),

$$\bar{j}_{elec} = -j^o \exp\left(-\alpha k \bar{\eta}_c\right) \cdot \Gamma_{elec} \,, \tag{3.18}$$

where Γ_{elec} is given by Eq. (2.25).

With linearization of the transient parts, $\delta\phi^c$ is directly proportional to $\delta c^c_{\mathrm{H}^+}$ (Eq. B.11) and the governing equations reduce to two coupled ordinary differential equations for $\delta c^c_{\mathrm{H}^+}$ and δc_{O_2},

$$\left(\frac{i\omega}{(1-\Lambda\bar{c}^c_{\mathrm{H}^+}R^2)^2} - D_{\mathrm{H}^+} \cdot \frac{1+c_1\bar{c}^c_{\mathrm{H}^+}}{1-\Lambda\bar{c}^c_{\mathrm{H}^+}R^2} \cdot \partial_{zz}\right) \delta c^c_{\mathrm{H}^+} = \frac{2\delta j_F}{FR} \tag{3.19}$$

$$\left(i\omega - D_{\mathrm{O}_2}\partial_{zz}\right) \delta c_{\mathrm{O}_2} = \frac{\delta j_F}{2FR} \tag{3.20}$$

where the transient Faradaic current density is

$$\delta j_F = \bar{j}_{elec}\left(c_2 \delta c^c_{\mathrm{H}^+} \bar{c}_{\mathrm{O}_2} + \delta c_{\mathrm{O}_2}\right) / c^o_{\mathrm{O}_2} \tag{3.21}$$

and constants c_1 and c_2, given respectively by Eqs. (B.12) and (B.13), are related to the steady state concentration $\bar{c}^c_{\mathrm{H}^+}$. The capacitive current density is

$$\delta j_C = -\frac{i\omega FR\delta c^c_{\mathrm{H}^+}}{2(1-\Lambda\bar{c}^c_{\mathrm{H}^+}R^2)} \tag{3.22}$$

where Eq. (B.4) was used to evaluate $\sigma = \varepsilon\partial_r\delta\phi\big|_{r=R}$.

The 1D system requires boundary conditions only at the pore ends. At $z = L$, the boundary conditions remain the same as in the general case,

$$\partial_z \delta c^c_{\mathrm{H}^+} = 0, \; \delta c_{\mathrm{O}_2} = 0. \tag{3.23}$$

At $z = 0$, the boundary condition for oxygen also remains

$$\partial_z \delta c_{O_2} = 0; \tag{3.24}$$

the boundary condition for proton concentration is given by Eq. (3.13), with the partial derivatives (Eqs. 3.14, 3.16) evaluated at $r = 0$,

$$\delta c^c_{H^+} = -c_3 \delta\phi^M, \;\; c_3 = \frac{k\bar{c}^c_{H^+}(1-\Lambda\bar{c}^c_{H^+}R^2)^2}{1-(\Lambda\bar{c}^c_{H^+}R^2)^2 + 4\varepsilon\Lambda\bar{c}^c_{H^+}R/C_H} \; . \tag{3.25}$$

Scale up from pore to UTCL response

For a simple structural UTCL model consisting of straight, parallel, cylindrical pores, the porosity is given by the ratio of the area of pore openings to geometric UTCL area,

$$X_p = \frac{A_{pores}}{A_{geom}} \; . \tag{3.26}$$

The heterogeneity factor is the ratio of active Pt area to A_{geom},

$$h = \frac{A_{Pt}}{A_{geom}} \; . \tag{3.27}$$

The pore density can be calculated from X_p or h,

$$n = \frac{X_p}{\pi R^2} = \frac{h}{2\pi RL} \; . \tag{3.28}$$

and allows for the scale-up of the pore model to give the catalyst layer impedance response, $Z_{CL} = Z/n$. As in Ch. 2, we do not consider the effects of pore connectivity, tortuosity, or roughness in this simple scale up.

In calculated impedance spectra, we assume $n = 1 \times 10^{11}/\text{cm}^2$, which corresponds to, e.g. $h = 4\pi$, $L = 200\text{nm}$, and $R = 10\text{nm}$. Such geometric values are on the order of

magnitude as those estimated for 3M NSTFs and Pt-plated NPGLs (as shown in Table III of Ref. [2]).

3.3 Results and Discussion

The one dimensional equation system, Eqs. (3.19, 3.20), and boundary conditions, Eqs. (3.23 − 3.25), can be solved analytically in certain cases. The analytical expressions yield physically intuitive equivalent circuit interpretations of the UTCL impedance that can be applied to analyze experimental data. Their accuracy is verified with numerical solutions of the full 2D system, detailed in Appendix C. In the spectra presented, lines correspond to the analytical solutions, and points the numerical ones. Unless otherwise indicated, the frequency range for all calculated impedance spectra was $f = 10^{-3} - 10^{8}$ Hz.

In what follows, we derive and discuss the analytical solutions to the bulk UTCL impedance response in four cases. The simplest, blocking electrode case corresponds to a O_2–free (e.g. N_2–fed) electrode, where no Faradaic reactions occur. With O_2–fed electrodes, the impedance response has analytical solutions in three cases:

- The fast reactant transport case, where δc_{H^+} and $\delta\phi$ within the pore respond instantaneously to the applied $\delta\phi^M$, and O_2 does not deplete significantly inside the pore.
- The fast oxygen diffusion case, where limitations in H^+ transport dominate the impedance response, and O_2 does not deplete significantly inside the pore.
- The fast proton transport case, where δc_{H^+} and $\delta\phi$ within the pore respond instantaneously to the applied $\delta\phi^M$, and limitations in O_2 transport dominate the impedance response.

As illustrated in the schematic of Figure 3.1, which case applies depends on the steady state proton concentration (which depends on ϕ^{pzc}), the applied overpotential $\overline{\eta}_c$, and the pore dimensions. The fast transport case applies at low $|\overline{\eta}_c|$. At higher $|\overline{\eta}_c|$, transport limitations are present. The fast O_2 diffusion case applies for low ϕ^{pzc} materials, where proton concentrations and current densities tend to be low, and the fast H^+ transport case applies for high ϕ^{pzc}, where proton concentrations and current densities tend to be high. At very large $|\overline{\eta}_c|$, both reactant species should show transport limitations and the impedance would have to be calculated numerically. As discussed below, H^+ and O_2 transport limitations both show characteristic features in the Nyquist plots.

Taking pore dimensions of $R = 20$nm and $L = 300$nm corresponding to estimated pore geometry for 3M NSTF as an example (Ch. 2), the horizontal boundary in Figure 3.1 would be at approximately $|\overline{\eta}_c| \sim 0.4$V, and the vertical one at $\phi^{pzc} \sim 0.7$V. Both reactants are expected to show transport limitations where $|\overline{\eta}_c| \gtrsim 0.8$V.

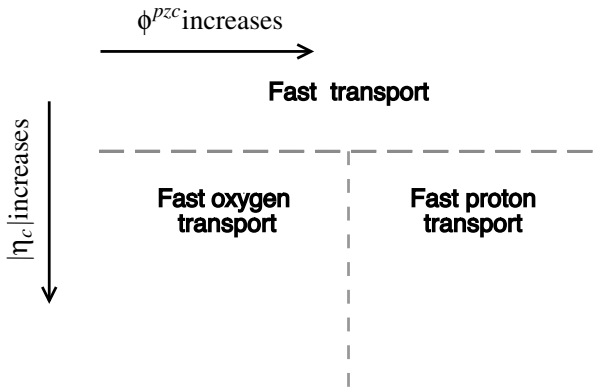

Figure 3.1: Rough schematic of the regions where the three analytical approximations are applicable to the impedance response of O_2-fed electrodes. Locations of the boundaries depend on pore geometry.

3.3.1 Case 1: Blocking electrode response

The blocking electrode case corresponds to an O_2-free impedance measurement, (i.e. a N_2-fed cathode). Under these conditions, the proton conductivity and capacitance of the UTCL can be characterized without interference from the charge transfer response. With $\delta j_F = 0$, Eq. (3.19) simplifies to

$$\left(\frac{i\omega}{1-\Lambda \bar{c}^c_{H^+} R^2} - D_{H^+}(1+c_1 \bar{c}^c_{H^+})\partial_{zz} \right) \delta c^c_{H^+} = 0 \tag{3.29}$$

which, with boundary conditions in Eqs. (3.23, 3.25), has the solution

$$\delta c^c_{H^+} = -c_3 \delta\phi^M \frac{\cosh \nu(z-L)}{\cosh \nu L}, \quad \text{where } \nu^2 = \frac{i\omega}{D_{H^+}(1+c_1 \bar{c}^c_{H^+})(1-\Lambda \bar{c}^c_{H^+} R^2)} . \tag{3.30}$$

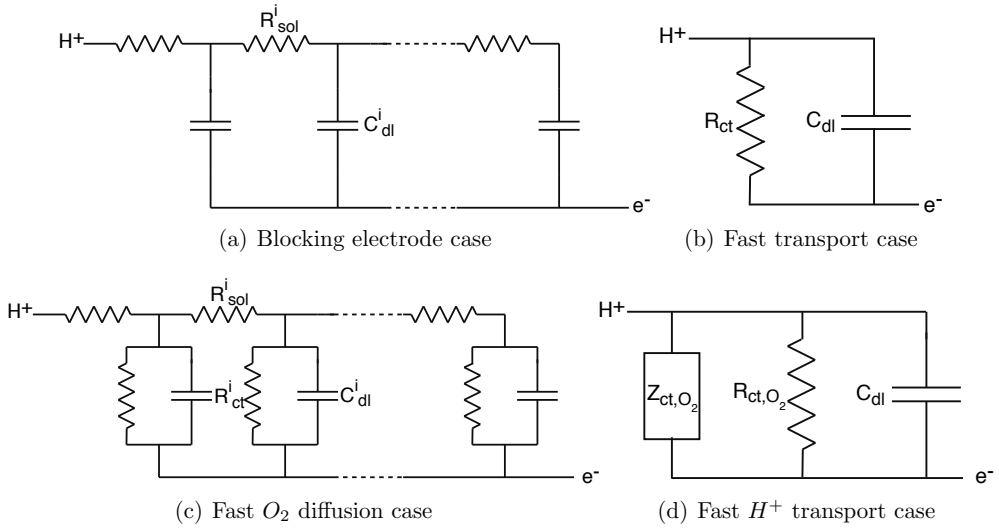

(a) Blocking electrode case (b) Fast transport case

(c) Fast O_2 diffusion case (d) Fast H^+ transport case

Figure 3.2: Equivalent circuit interpretations of the impedance response of a UTCL in 4 limiting cases: (a) Blocking electrode case, (b) Fast transport case, (c) Fast O_2 diffusion case, (d) Fast H^+ transport case.

The impedance response corresponds to a transmission line equivalent circuit, illustrated in Figure 3.2(a), like that for electrolyte-filled pores (units $\Omega \cdot \mathrm{cm}^2$) [122],

$$Z_{CL}(\omega) = \sqrt{\frac{R_{sol}}{i\omega C_{dl}}} \coth \sqrt{R_{sol} i\omega C_{dl}}, \tag{3.31}$$

where the solution resistance ($\Omega \cdot \mathrm{cm}^2$) has the form

$$R_{sol} = \frac{1}{n} \cdot \frac{R_g T L}{D_{\mathrm{H}^+} F^2 \int_0^R \overline{c}_{\mathrm{H}^+}(r) 2\pi r dr} = \frac{L}{8 X_p \varepsilon D_{\mathrm{H}^+}} \cdot \frac{(1 - \Lambda \overline{c}^c_{\mathrm{H}^+} R^2)}{\Lambda \overline{c}^c_{\mathrm{H}^+}} \quad , \tag{3.32}$$

and the double layer capacitance is ($\mathrm{F/cm}^2$)

$$C_{dl} = h \cdot \frac{\partial \overline{\sigma}}{\partial \overline{\phi}^M} = \frac{\varepsilon h}{R} \cdot \frac{4 \Lambda \overline{c}^c_{\mathrm{H}^+} R^2}{1 - (\Lambda \overline{c}^c_{\mathrm{H}^+} R^2)^2 + 4 \varepsilon \Lambda \overline{c}^c_{\mathrm{H}^+} R / C_H} \, . \tag{3.33}$$

Corresponding transmission line elements, R^i_{sol} and C^i_{dl}, are given by $R_{sol} \cdot \Delta z$ and $C_{dl} \cdot \Delta z$, respectively, where Δz represents a single element of the transmission line.

The essential distinguishing feature of the water-flooded pore response is the dependence of R_{sol} and C_{dl} on $\overline{\sigma}$, which is tuned by $\overline{\phi}^M - \phi^{pzc}$. Figure 3.3 shows the impedances corresponding to $\overline{\phi}^M - \phi^{pzc} = -0.4$, 0, and $+0.4$V, $R = 5$nm, L=100nm, and $n = 1 \times 10^{11} \mathrm{cm}^{-2}$. Figure 3.4(a) shows R_{sol} and C_{dl} as a function of $\overline{\phi}^M - \phi^{pzc}$, for the same pore geometry.

On a logarithmic scale, both R_{sol} and C_{dl} show a transition in slope near ϕ^{pzc}. The slopes of $\log R_{sol}$, $\log C_{dl}$ vs. $\overline{\phi}^M$ at $\overline{\phi}^M \gtrsim \phi^{pzc}$ are $k/2.3$ and $-k/2.3$, respectively, and both level off to zero as $\overline{\phi}^M$ decreases from ϕ^{pzc}. At high proton concentrations ($\overline{\phi}^M - \phi^{pzc} < 0$ and $\Lambda \overline{c}^c_{\mathrm{H}^+} R^2 \to 1$), $C_{dl} \to C_H \cdot h$, i.e. the Helmholtz capacitance dominates the capacitive response.

As noted in Sec. 2.3.2, the charging behaviour of Pt is complicated by adsorption, and corresponding shifts in the ϕ^{pzc}. R_{sol} and C_{dl} should thus show more complex dependence on ϕ^M than predicted by the current Stern model. We will explore this

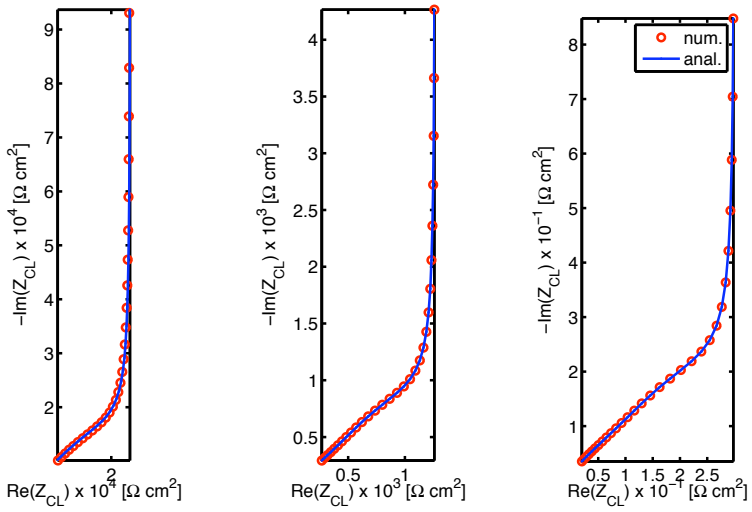

(a) (b) (c)

Figure 3.3: High frequency blocking electrode impedances at various $\bar{\phi}^M - \phi^{pzc}$, calculated from numerical solution of the 2D general system of equations (dots) and 1D analytical approximations (lines). Assumed $n = 1 \times 10^{11}$ cm^{-2}, $R = 5$nm, L=100nm. To highlight the high frequency regions, frequency ranges were varied. (a) $\bar{\phi}^M - \phi^{pzc} = -0.4$V, $f = 10^{6.5} - 10^8$Hz, (b) $\bar{\phi}^M - \phi^{pzc} = 0$V, $f = 10^6 - 10^8$Hz, (c) $\bar{\phi}^M - \phi^{pzc} = +0.4$V, $f = 10^{5.5} - 10^8$Hz.

further in Sec. 3.3.5.

The low and high frequency limits of Z_{CL}, well known from de Levie's model [122], are

$$\lim_{\omega\to 0} Z_{CL} = \frac{1}{i\omega C_{dl}} + \frac{R_{sol}}{3}, \quad \lim_{\omega\to\infty} Z_{CL} = \sqrt{\frac{R_{sol}}{\omega C_{dl}}} \cdot \frac{1-i}{\sqrt{2}}, \tag{3.34}$$

i.e. at low ω the real component of the impedance approaches $R_{sol}/3$, and at high ω there is a 45^o incline from the Re(Z) axis on a Nyquist plot. These features are shown in Figure 3.3. R_{sol} can thus simply be read off the low frequency impedance, and C_{dl} can be obtained by a fit to the high frequency region. We can define

$$\omega_{sol} = \frac{1}{R_{sol} C_{dl}} \tag{3.35}$$

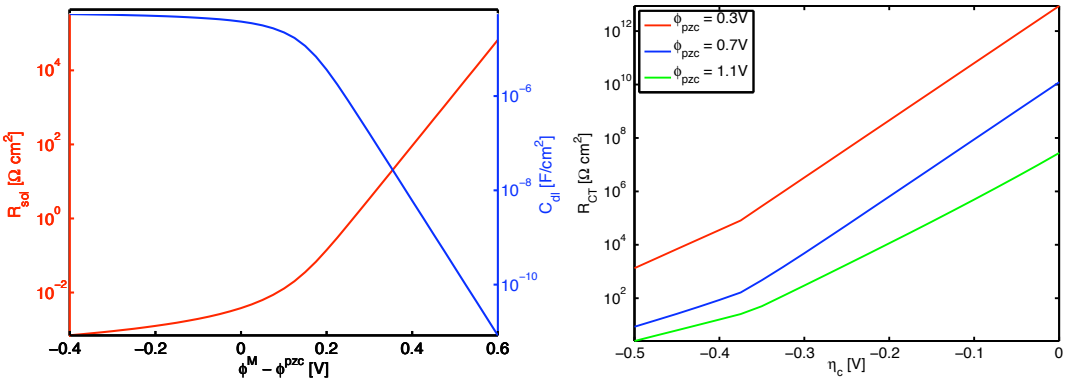

(a) (b)

Figure 3.4: Variation of equivalent circuit elements with potential: (a) R_{sol} and C_{dl} vs. $\overline{\phi}^{M} - \phi^{pzc}$, (b) R_{ct} vs. $\overline{\eta}_c$ at various ϕ^{pzc}. Assumed pore radius $R = 5$nm, L=100nm, $n = 1 \times 10^{11}\text{cm}^{-2}$.

as a critical frequency for the onset of high frequency behaviour. The larger $R_{sol}C_{dl}$ is, the smaller the ω_{sol}. Hence, the appearance of the 45^o incline at lower frequencies is indicative of more severe proton transport limitations and/or higher capacitances.

R_{sol} can be used to determine $\overline{\sigma}$ and Γ_{elec}. Electroneutrality requires that $\overline{\sigma}$ balance the charge of the protons in the water-flooded pores; rearranging Eq. (3.32),

$$\overline{\sigma} = \frac{R_g T L^2}{h D_{\text{H}^+} F R_{sol}} \,. \tag{3.36}$$

With knowledge of pore dimensions and porosity, Γ_{elec} can be determined from R_{sol}; rearranging Eq. (B.10),

$$\Gamma_{elec} = \left[\frac{R_{sol}^2 K^2 c^o_{\text{H}^+} \Lambda}{L(R_{sol}K + R^2 L)} \right]^{\alpha-\gamma}, \; K = 8 X_p \varepsilon D_{\text{H}^+} \,, \tag{3.37}$$

where $\alpha - \gamma = -1/2$, as determined in Ref. [10].

3.3.2 Case 2: Fast reactant transport

The fast transport case applies where the UTCL is sufficiently thin, $L \lesssim 300$nm, and the applied overpotential is low, $|\overline{\eta}_c| \lesssim 0.4$V. The proton concentration then responds instantaneously to the applied potential, and O_2 transport is not limiting,

$$\delta c^c_{H^+} = -c_3 \delta\phi^M,\ \bar{c}_{O_2} = c^o_{O_2},\ \delta c_{O_2} = 0\ . \tag{3.38}$$

The corresponding impedance response of the UTCL is that of a simple parallel *RC* circuit, illustrated in Figure 3.2(b), with the form

$$Z_{CL}(\omega) = \left[\frac{1}{R_{ct}} + i\omega C_{dl}\right]^{-1}\ . \tag{3.39}$$

The charge transfer resistance R_{ct} is $(\Omega \cdot \mathrm{cm}^2)$

$$R_{ct} = \frac{1}{h}\cdot\frac{\partial\overline{\phi}^M}{\partial\overline{j}_{elec}} = -\frac{1}{h}\cdot\frac{R_g T}{F}\cdot\frac{1}{\overline{j}_{elec}}\cdot\frac{1-(\Lambda\bar{c}^c_{H^+}R^2)^2+4\varepsilon\Lambda\bar{c}^c_{H^+}R/C_H}{\left[\gamma\left(1-(\Lambda\bar{c}^c_{H^+}R^2)^2\right)+\alpha\left(4\varepsilon\Lambda\bar{c}^c_{H^+}R/C_H\right)\right]}\ . \tag{3.40}$$

where the last term is a factor that varies from $1/\gamma$ to $1/\alpha$, and has a range of $2/3$ to 2. Figure 3.5 shows two impedance spectra where the fast transport case applies, at $\phi^{pzc} = 1.1$V, $\overline{\eta}_c = -0.2$ and -0.25V, R = 5nm, and L =100nm. R_{ct} is equal to the zero frequency impedance, and corresponds to the diameter of the characteristic semicircle in a Nyquist plot. C_{dl} can be determined from the characteristic frequency at the apex of the semicircle, $\omega_c = 1/R_{ct}C_{dl}$.

Figure 3.4(b) shows the variation of R_{ct} with $\overline{\eta}_c$ and ϕ^{pzc} for a UTCL with R=5nm, L=100nm, and $n = 1\times10^{11}\mathrm{cm}^{-2}$. R_{ct} depends on ϕ^{pzc} as well as $\overline{\eta_c}$, since $\overline{j}_{elec}$ depends on both of these factors.

The slope of $\log R_{ct}$ vs. $\overline{\eta}_c$ arises from the dependence of R_{ct} on $\overline{j}_{elec}$ (Eq. 3.18).

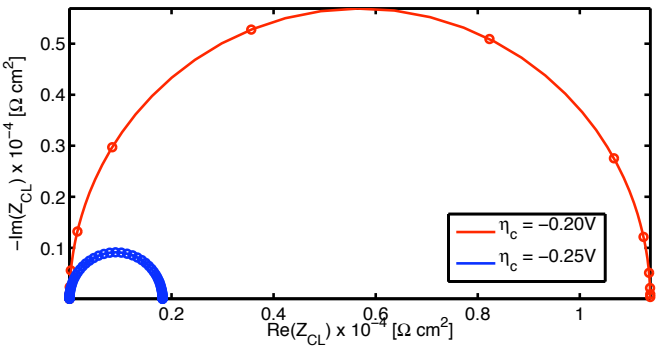

Figure 3.5: Numerically calculated (dots) and analytically approximated impedance in the fast transport case (line). $\phi^{pzc} = 1.1$V, R = 5nm, L =100nm, $n = 1 \times 10^{11}$ cm^{-2}.

From Section 2.4.1, Γ_{elec} has a linear dependence on $\overline{\phi}^M$ at $\overline{\phi}^M - \phi^{pzc} \lesssim 0.1$V, and takes the form $\exp\left(k\left[\alpha-\gamma\right]\left[\overline{\phi}^M - \phi^{pzc}\right]\right)$, at $\overline{\phi}^M - \phi^{pzc} \gtrsim 0.1$V, with $\alpha - \gamma = -1/2$. Hence, the slope of $\log R_{ct}$ vs. dimensional $\overline{\eta}_c$ is expected to be $k\alpha/2.3$ in the former case, and $k(\alpha+1/2)/2.3$ in the latter one. This is consistent with the lower slope shown for $\phi^{pzc} = 1.1$V than those for $\phi^{pzc} = 0.3$ or 0.7V shown in Fig. 3.4(b). The shift in slopes at $\overline{\eta}_c \approx -0.37$V for all three curves arises from the shift in α corresponding to the transition between Temkin to Langmuirian kinetics for oxygen reduction [10].

3.3.3 Case 3: Fast oxygen diffusion

The fast O_2 diffusion case applies at low c_{H^+} (low $\phi^{pzc} \lesssim 0.7$V) and high $|\overline{\eta}_c| \gtrsim 0.4$V. With low c_{H^+}, the current density would also be low and O_2 transport is not expected to be limiting. Assuming $\overline{c}_{O_2} = c^o_{O_2}$, $\delta c_{O_2} = 0$, Eq. (3.19) simplifies to

$$\left(\frac{i\omega}{(1-\Lambda\overline{c}^c_{H^+}R^2)^2} - \frac{2\overline{j}_{elec}c_2}{FR} - D_{H^+}\cdot\frac{1+c_1\overline{c}^c_{H^+}}{1-\Lambda\overline{c}^c_{H^+}R^2}\cdot\partial_{zz}\right)\delta c^c_{H^+} = 0\,. \tag{3.41}$$

Constants c_1 and c_2 are given by Eqs. (B.12, B.13). The corresponding impedance response is

$$Z_{CL}(\omega) = \sqrt{R_{sol} Z_{int}} \coth \sqrt{\frac{R_{sol}}{Z_{int}}}, \quad Z^{int} = \left[\frac{1}{R_{ct}} + i\omega C_{dl} \right]^{-1} \tag{3.42}$$

where R_{sol}, C_{dl} and R_{ct} are given by Eqs. (3.32), (3.33), and (3.40), respectively. This response corresponds to the transmission line equivalent circuit illustrated in Figure 3.2(c) [122]. The element R^i_{ct} is given by $R_{ct}/\Delta z$.

At large frequencies, charging dominates the impedance response, and $Z_{CL}(\omega \to \infty)$ is identical to that of the blocking electrode (2nd part of Eq. 3.34), i.e. a 45^o incline in the high frequency region of the Nyquist plot is observed as the hallmark of proton transport limitations [125]. Where there are severe proton transport limitations, $R_{sol} \gg R_{ct}$, the low frequency impedance is

$$\lim_{\omega \to 0} Z_{CL} \approx \sqrt{R_{sol} R_{ct}} \; ; \tag{3.43}$$

in this case, R_{ct} can be estimated from the zero-frequency impedance, when R_{sol} is known. In the case $R_{sol} \ll R_{ct}$, we recover the same zero-frequency limit as in the fast transport case,

$$\lim_{\omega \to 0} Z_{CL} \approx R_{ct} \; . \tag{3.44}$$

Figure 3.6 shows the fast O_2 transport impedances at R = 5nm, $\phi^{pzc} = 0.3$V, $\overline{\eta}_c = -0.6$V, and various L. As expected, the characteristic straight line inclined at 45^o to the real axis is more prominent for the longer pore lengths. In the case of L = 1μm, the low frequency deviations of the numerically calculated impedance (shown in dots) from the analytical approximation (shown as a line) is due to the depletion of protons at steady state; the corresponding $\overline{c}_{H^+}$ distribution at $r = R$ is shown in Fig. 3.7. The depletion of $\overline{c}_{H^+}$ leads to the increase in values of R^i_{sol} and R^i_{ct} along z, not accounted

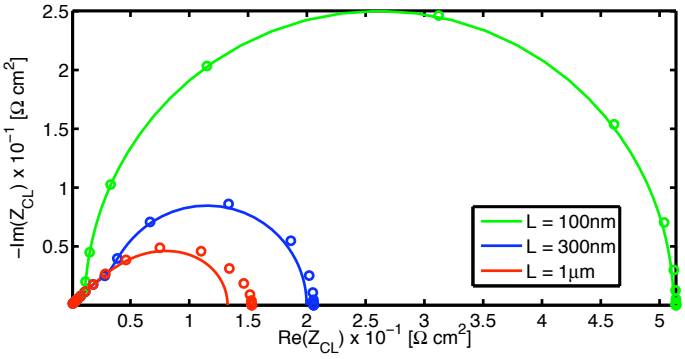

Figure 3.6: Numerically calculated (dots) and analytically approximated impedances in the fast O_2 diffusion case (lines) at $n = 1 \times 10^{11}$ cm^{-2}, $R = 5$nm, $\phi^{pzc} = 0.3$V, $\overline{\eta}_c = -0.6$V, and $L = 100$, 300, and 1000nm

for in the analytical approximation. However, the general trends in the impedance are well reproduced by the analytical approach.

3.3.4 Case 4: Fast proton transport

The fast H^+ transport case applies at high c_{H^+} ($\phi^{pzc} \gtrsim 0.7$V) and high $|\overline{\eta}_c| \gtrsim 0.4$V. Consideration of oxygen diffusion limitations requires the steady oxygen distribution $\overline{c}_{O_2}$, obtained from the solution of the steady state part of Eq. (B.1),

$$\overline{c}_{O_2} = c^o_{O_2} \cdot \frac{\cosh\left(\sqrt{\omega_k/\omega_d}\cdot z/L\right)}{\cosh\sqrt{\omega_k/\omega_d}}\ ,\ \omega_k = -\frac{\overline{j}_{elec}}{2F c^o_{O_2} R}\ ,\ \omega_d = \frac{D_{O_2}}{L^2}\ , \tag{3.45}$$

where we have introduced characteristic kinetic and diffusive frequencies, ω_k and ω_d, respectively. The effectiveness of oxygen diffusion is

$$\Gamma_{O_2} = \frac{1}{L c^o_{O_2}} \int_0^L \overline{c}_{O_2} dz = \frac{\tanh\sqrt{\omega_k/\omega_d}}{\sqrt{\omega_k/\omega_d}}\ . \tag{3.46}$$

Assuming protons respond instantaneously to the applied $\delta\phi^M$, $\delta c_{H^+} = -c_3\delta\phi^M$, Eq. (3.20) reduces to

$$\left[i\omega - \omega_k - D_{O_2}\partial_{zz}\right]\delta c_{O_2} = -\omega_k c_2 c_3 \bar{c}_{O_2}(z)\cdot\delta\phi^M \ , \tag{3.47}$$

which has the solution

$$\delta c_{O_2} = c_2 c_3 \cdot \frac{\omega_k}{i\omega}\cdot\left(c^o_{O_2}\cdot\frac{\cosh\sqrt{(\omega_k+i\omega)/\omega_d}\cdot z/L}{\cosh\sqrt{(\omega_k+i\omega)/\omega_d}} - \bar{c}_{O_2}(z)\right)\delta\phi^M \ . \tag{3.48}$$

Constants c_2 and c_3 are given in Appendix B.

The corresponding impedance response is

$$Z_{CL} = \left[\frac{1}{Z_{ct,O_2}} + \frac{1}{R_{ct,O_2}} + i\omega C_{dl}\right]^{-1} \ , \tag{3.49}$$

and has the equivalent circuit shown in Figure 3.2(d). Z_{ct,O_2} and R_{ct,O_2} are diffusive and resistive components. These components take the form

$$Z_{ct,O_2} = R_{ct}\cdot\frac{i\omega/\omega_k}{\frac{\tanh\sqrt{(\omega_k+i\omega)/\omega_d}}{\sqrt{(\omega_k+i\omega)/\omega_d}} - \Gamma_{O_2}} \ , \ R_{ct,O_2} = \frac{R_{ct}}{\Gamma_{O_2}} \ . \tag{3.50}$$

Z_{CL} has the same form as the impedance expression derived in Ref. [126] for an electrolyte-filled pore with reactant concentration gradient. Where oxygen diffusion limitations are prominent, $\omega_k \gg \omega_d$, the low frequency impedance is

$$\lim_{\omega\to 0,\omega_k\gg\omega_d} Z_{CL} = R_{ct}\cdot 2\sqrt{\omega_k/\omega_d}. \tag{3.51}$$

Where oxygen diffusion is not limiting, $\Gamma_{O_2}\to 1$ and $\omega_k \ll \omega_d$, and we recover the same

low frequency impedance as for the fast transport case,

$$\lim_{\omega\to 0,\omega_k\ll\omega_d} Z_{CL} = R_{ct} \ . \tag{3.52}$$

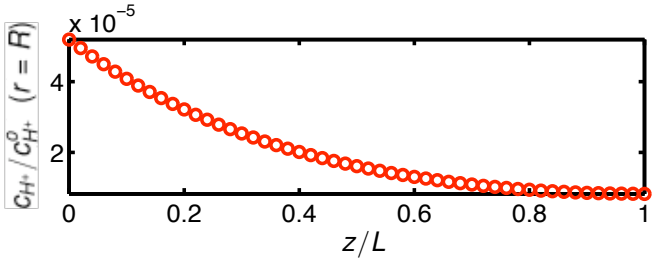

Figure 3.7: Numerically calculated steady state proton concentration profile at $r = R$, for parameters $R = 5$nm, $L = 1\mu$m, $\phi^{pzc} = 0.3$V, $\overline{\eta}_c = -0.6$V. $\bar{c}_{\mathrm{H}^+}\big|_{r=R}$ shows significant variation along z, which led to the deviation of the numerically calculated impedance from the analytically approximated one.

Figure 3.8 shows the numerically calculated impedances (dots) for $\phi^{pzc} = 1.1$V, $\overline{\eta}_c = -0.4$ and -0.6V, $R = 5$nm, and $L = 100$nm and 1μm, as well as the analytical approximations from the fast H^+ transport (solid lines) and fast transport (dashed lines) cases. The more severe the steady state oxygen diffusion limitations, the larger the Nyquist semicircle is relative to that from the fast transport approximation.

Figure 3.9 shows $\log Z_{CL}(\omega \to 0)$ vs. dimensional $\overline{\eta}_c$ in solid lines, for $\phi^{pzc} = 0.7$ and 1.1V; dotted lines show the corresponding fast transport, zero frequency limit. With the onset of oxygen transport limitations, the slope of $\log Z_{CL}(\omega \to 0)$ vs. $\overline{\eta}_c$ shows a marked decrease from that of the fast transport case; this arises from the factor $\sqrt{\omega_k/\omega_d} \propto \sqrt{\bar{j}_{elec}}$ in Eq. (3.51). Since $R_{ct} \propto 1/\bar{j}_{elec}$ (Eq. 3.40), overall, $Z_{CL}(\omega \to 0) \propto 1/\sqrt{\bar{j}_{elec}}$; thus, oxygen diffusion limitations leads to a halving of the slope of $\log Z_{CL}(\omega \to 0)$ vs. $\overline{\eta}_c$ relative to the fast transport case.

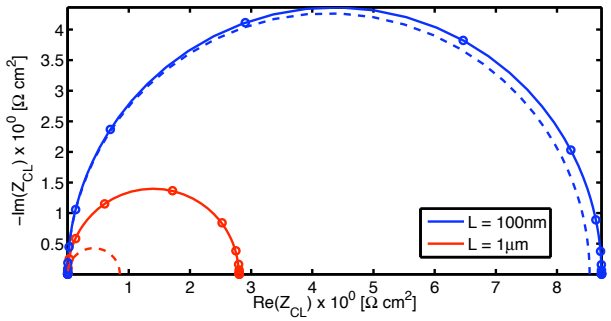

(a) $\overline{\eta}_c = -0.4$V

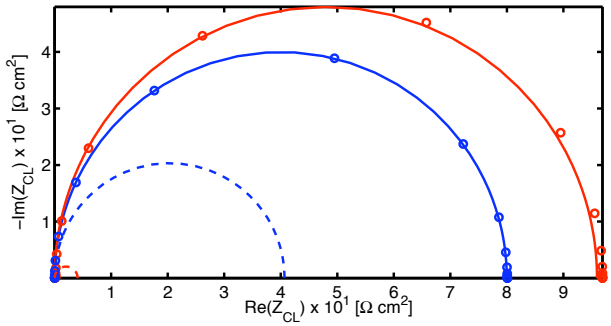

(b) $\overline{\eta}_c = -0.6$V

Figure 3.8: Numerically calculated impedance spectra (dots) and analytical approximations at the fast H^+ transport (solid lines) and fast transport (dashed lines) cases at $\phi^{pzc} = 1.1$V, $R = 5$nm, $L = 100$nm and 1μm, and $n = 1 \times 10^{11}$ cm^{-2}. (a) $\overline{\eta}_c = -0.4$V, (b) $\overline{\eta}_c = -0.6$V

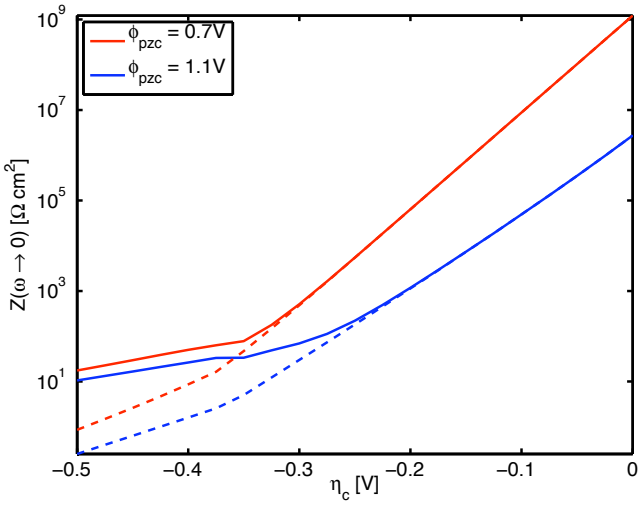

Figure 3.9: Solid lines: impedance at the zero frequency limit as calculated from the fast H^+ transport limit, at $\phi^{pzc} = 0.7,\ 1.1$V and $\overline{\eta}_c$, and for pore dimensions R = 5nm, L = 1μm, and $n = 1 \times 10^{11}$ cm^{-2}. Dotted lines: the corresponding R_{ct} from the fast transport limit, for comparison.

3.3.5 Characterization Capabilities and Challenges, and Preliminary Results

The developed impedance model allows for the analysis of electrostatic, kinetic, and transport contributions to UTCL performance. With the surface charge controlled proton transport mechanism as a key assumption of the model, a determination of R_{sol} and C_{dl} as a function of $\overline{\phi}^M$ would be the first priority. For Pt, the relation of R_{sol} and C_{dl} to $\overline{\phi}^M$ is expected to be more complex than suggested by Fig. 3.4, due to the oxidation of Pt (cf. Sec. 2.3.2); ϕ^{pzc} may not be fixed and the variation of surface charge density with potential may not be monotonic. Regardless of these complications, one can still extract $\overline{\sigma}$ from R_{sol}. With knowledge of UTCL porosities and pore dimensions, Γ_{elec} can also be determined from R_{sol} (Eq. 3.37).

In the presence of oxygen transport limitations, Eqs. (3.49, 3.50) could be applied to fit the impedance data; however, this involves many fitted elements, which

increases uncertainties. A simpler way to probe for transport limitations is in the slope of $\log Z_{CL}(\omega \to 0)$ vs. $\bar{\eta}_c$, as discussed in Sec. 3.3.4; from Eq. (3.51), we may be able to estimate ω_k/ω_d; with a reasonable estimate of ω_d, we could estimate Γ_{O_2}.

Where the range of potential probed is not sufficient for this analysis, one can "check" for oxygen diffusion limitations in the product $R_{ct}\bar{j}_{CL}$. From Eq. (3.40), which assumes no O_2 diffusion limitations, this product is expected to be R_gT/F times a constant factor of 2/3 to 2, depending on the steady state proton concentration, i.e. approximately 0.045–0.060mV at 353K. Where there are oxygen diffusion limitations, the R_{ct} obtained would actually correspond to the $Z_{CL}(\omega \to 0)$ limit at $\omega_k >> \omega_d$, and $\bar{j}_{CL}$ would correspond to $\bar{j}_{elec}h\Gamma_{O_2}$; the apparent product of $R_{ct}\bar{j}_{CL}$ would then be approximately doubled. Therefore a $R_{ct}\bar{j}_{CL}$ of over 60mV would be a sign of O_2 diffusion limitations in the UTCL.

Currently, some impedance data for UTCLs have been reported in literature [48, 80, 127], but not at a systematic set of $\bar{\phi}^M$ required to provide insights for model refinement. Impedance measurements of UTCLs have several challenges:

- *High ω_{sol}, onset frequency for R_{sol} dominated Z_{CL}.*

  We can roughly estimate ω_{sol} by assuming the UTCL to have the same conductivity as for Pt black [80], i.e. $R_{sol} \approx R_{sol}^{\mathrm{PB}} \times L/L^{\mathrm{PB}}$, where PB indicates Pt black and L the layer thickness, and assuming a standard $C_H \approx C_{dl}$, $20\mu\mathrm{F/cm}^2$. This gives $\omega_{sol} = 42\mathrm{kHz}$; we must go beyond ω_{sol} in order to see the R_{sol} dominated region, and this is beyond the range of some standard impedance spectrometers. Also, high frequency inductances can contribute to the impedance response and thus obscure the R_{sol} response.

- *The capacitive response of the PEM|UTCL interface.*

  This can come into play where its associated impedance is on the order of the UTCL impedance response. Assuming that the PEM|UTCL response is in parallel to the bulk response (i.e. the PEM|Pt interfaces are the primary contribution), it

should be possible to separate the PEM|UTCL and pore response via [128]

$$Z = \left(\frac{1}{Z_{CL}} + i\omega C_{\text{PEM}} \right)^{-1}; \tag{3.53}$$

a significant PEM|UTCL capacitance (C_{PEM}) leads to a greater than 45^o incline in the high frequency region. This extra circuit element increases uncertainties in the fitting of the bulk UTCL response.

- *Adsorption pseudocapacitances.*

  The timescale of H adsorption is so short that the process acts as a simple, frequency–independent capacitance within practical frequency ranges; in fact, recent EIS studies of conventional CLs were performed with the working point in the H adsorption region, since the associated ω_{sol} is lowered by the increased capacitance [80, 129, 130]. Oxide adsorption, however, has longer timescales, so the associated pseudocapacitance is frequency dependent [3], which complicates the resultant impedance response. Unpublished results from GM indicated that the oxide pseudocapacitances completely obscure the blocking electrode impedance response of Pt black at 0.8V_{SHE}. In O_2–fed electrodes, these pseudocapacitances may pose less of an interference if R_{ct} associated with ORR is smaller; therefore it is worth probing these regions with an O_2–fed electrode to attempt to extract R_{sol}.

- *Low frequency inductive loops.*

  Low frequency inductive loops have also been observed in EIS studies of conventional catalyst layers, and have been attributed to oxide kinetics or water transport dynamics through the PEM [131–133]. As a first step we simply neglect these regions in the fitting of impedance data.

We now discuss the impedance data of 3M NSTF MEAs, performed by Zhong Xie

at the NRC Institute for Energy, Mining, and Environment. While the experimental data are very preliminary, we document them here, since they are, to the best of our knowledge, the first attempt to characterize the EIS of 3M NSTF. The MEA consisted of a of $0.2 mg_{Pt}/cm^2$ Pt 3M NSTF CL at the cathode, 3M proprietary PEM, a $0.1 mg_{Pt}/cm^2$ TKK conventional CL at the anode, and diffusion media of SGL 24 BC (GDL and MPL) at the cathode and TGP-60 carbon fibre paper (no MPL, 0% PTFE) at the anode. The thermal cycling break–in protocol recommended by 3M [134, 135] could not be implemented in existing experimental setups, so the conditioning was done using the new 3M fast condition protocol [135], which consists dry cycling between 0 and $0.2 A/cm^2$ 22x at 75C, 44x at 50C, at anode and cathode flow rates of 140 and 124mL/min, respectively. We note that this fast protocol was reported by 3M to give inconsistent results, and, upon their recommendation, we followed the protocol by flushing the MEA 3–5x with liquid water via a syringe. We note that cyclic voltammograms gave capacitances approximately 100x that expected in the double layer charging region, suggesting that this protocol was insufficient to remove all impurities from the NSTF; however, polarization curves still gave approximately the expected performance [136].

For the EIS measurements, H_2 and O_2 fed at ambient pressure and flow rates were 795 and 1780mL/min, respectively, to ensure differential cell conditions. A RH=100% was applied to ensure the cathode UTCL was fully flooded. A frequency range of 0.1Hz–10kHz and DC current densities of $0.04–3.17 A/cm^2$ were probed.

Fig. 3.10 shows the raw and fitted EIS curves. Given the $>45^o$ incline in the high frequency region, we fitted the spectra to Eq. (3.53) with Z_{CL} in the fast oxygen transport limit (Eq. 3.42). We also considered a high frequency resistance (HFR) in series with Z, arising from the Ohmic PEM and contact resistances. The circuit elements, fitted with nonlinear least squares, are shown in Fig. 3.11, and the error bars correspond to a 95% confidence interval. The low frequency loops were not included in the fit; all data points following a change in concavity of the spectra were discarded. The scatter in the

high frequency regions, attributed to instrumental error, was also discarded. Given that the reactants were fully humidified, the HFR was fitted across all spectra to a value of $0.047 \pm 0.001 \Omega cm^2$, close to the expected value for hydrated 3M PEMs. This HFR was used to determine the HFR–corrected potential in Fig. 3.11. C_{dl} was consistent with that determined from cyclic voltammetry. However, both C_{dl} and C_{PEM} were about 2 orders of magnitude larger than expected, given that a standard Helmholtz capacitance $C_H \approx 20 \mu F/cm^2$, and diffuse layer contributions would tend to reduce the total capacitance from this value. This would suggest contributions from impurities that were not fully evacuated during the break–in. We note, however, that this higher C_{dl} likely led to a lowering of ω_{sol}, which allowed us to see the entire distorted semicircle even when the highest frequency probed was only 10kHz.

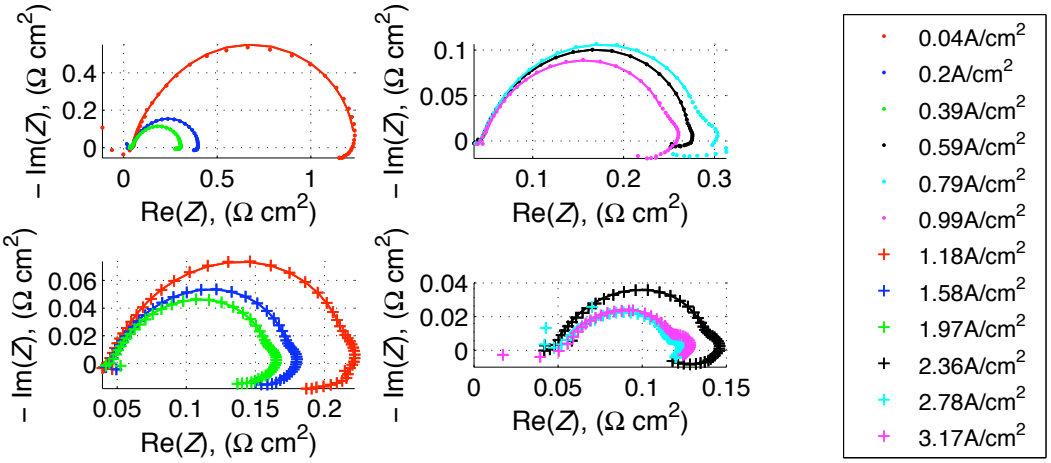

Figure 3.10: Raw (dots) and fitted (lines) EIS curves. Flow rates of H_2 and O_2 were 795 and 1780mL/min, respectively, and RH=100%. A frequency range of 0.1Hz–10kHz and DC current densities of 0.04–3.17A/cm^2 were probed.

From R_{sol}, the conductivity L/R_{sol} can be determined and is shown in Fig. 3.12. These values are at the same order of magnitude as determined for Pt Black [80]: 2–3 orders of magnitude larger than bulk water, but 1–2 orders of magnitude smaller than

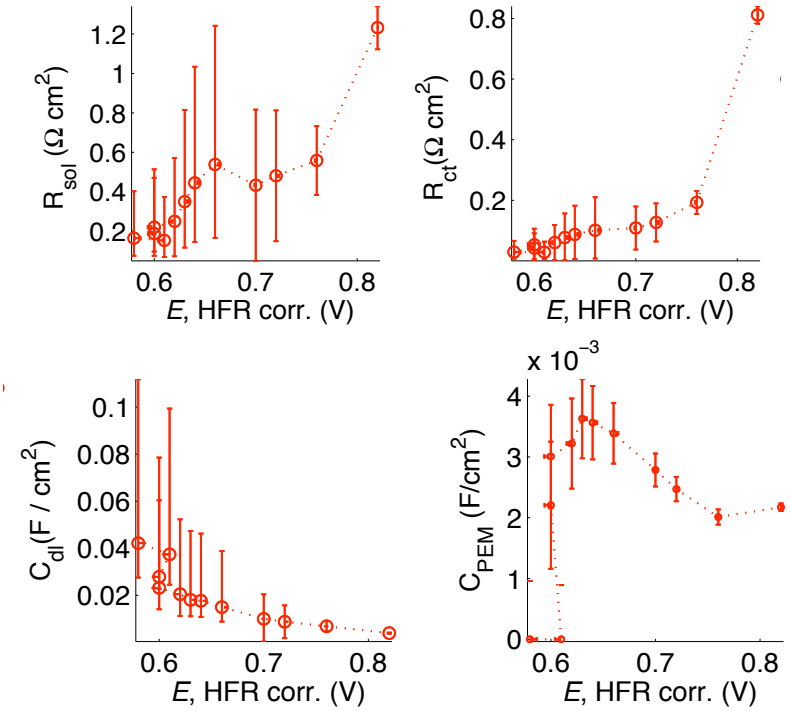

Figure 3.11: Circuit elements fitted via a non–linear least squares to Eq. (3.53) with Z_{CL} in the fast oxygen transport limit (Eq. 3.42). Error bars correspond to 95% confidence intervals. Dotted lines are guides for the eye only. Potentials E were corrected via the fitted HFR value of $0.047 \pm 0.001 \Omega\text{cm}^2$.

for conventional electrodes. The error bars, however, are too large and the range of potential too small to probe the variation of conductivity with potential.

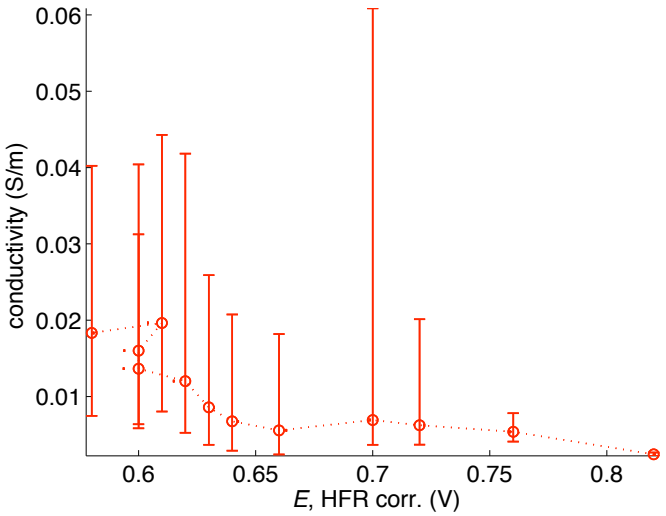

Figure 3.12: Conductivity of the 3M NSTF cathode as calculated from the fitted R_{sol}. Dotted lines are guides for the eye only.

Blocking (N_2–fed) electrode measurements were also attempted at +0.45V, an adsorbate free region, but the high frequency R_{sol} region could not be resolved, due perhaps to the contribution of high frequency inductances. It is not understood why the high frequency inductances, evidenced by a straight +Im(Z) contribution in the Nyquist plots appeared to be more pronounced in these measurements than in the O_2–fed ones.

While further detailed studies with the 3M NSTF are in progress, these preliminary results suggest that 3M NSTF may not be an appropriate model system to probe the proton transport mechanism, given its thickness and high corresponding ω_{sol} that prohibits a more precise determination of R_{sol}. A more appropriate choice would be a much thicker model system such as Pt Black. Pt Black catalyst layers were investigated successfully in a blocking electrode setup in Ref. [80] at a fixed working point. The

advantage of thicker layers is that they would have higher R_{sol} and C_{dl} and lower corresponding ω_{sol}, and likely a reduced C_{PEM} contribution due to the increased Z_{CL}. To build upon the Pt Black study, we could repeat the measurements at a range of potentials, with both blocking and O_2–fed setups, since at +0.8V oxide pseudocapactances obscure the blocking electrode response. Given the complex charging behaviour of Pt (Sec. 2.3.2), it would also be insightful to characterize a nanoporous layer of a more inert material such as Au (e.g. thick Au–NPGL), where the surface is adsorbate–free over a significantly larger potential range, and R_{sol} expected to follow the simple relation shown in Fig. 3.4.

3.4 Summary

This chapter presented an impedance model of water-flooded pores in ionomer-free UTCLs. Assuming pores of high aspect ratios, we derived analytical impedance expressions with equivalent circuit representations in the blocking, fast transport, fast oxygen diffusion, and fast proton transport cases. The crucial distinguishing feature of water-flooded pores from electrolyte-filled ones is that solution resistance and double layer capacitance are highly dependent on the metal phase surface charge, which is tuned by the applied metal potential of the UTCL material. The impedance expressions allow for the analysis of electrostatic, kinetic, and transport processes to the overall Faradaic current density produced in the UTCL, and for the determination of interfacial parameters of UTCL materials. We recommend that model evaluation be performed on thick model systems, e.g. Pt black catalyst layers; UTCLs of standard thicknesses are expected to have high characteristic frequencies, so their impedance responses may not be easily resolved from high frequency inductive and capacitive responses.

Chapter 4

Generalised Computational Hydrogen Electrode

4.1 Motivation

The previous two chapters suggest the surface charge density of Pt/Pt oxide species to have a major impact on the proton conductivity and performance of ionomer–free catalyst layers. The charging behaviour of the Pt|solution interface is particularly complex, due to oxide species adsorption. Since specific adsorption alters the surface electronic structure [26], the charge density is highly dependent on oxide coverage. To our knowledge, the last experimental work to address this phenomenon was from Frumkin and Petrii in the 1970s; using ion radiotracers, they found an "inverse ϕ^{pzfc}" in the oxide region [98, 137]. Above this inverse ϕ^{pzfc}, the surface becomes more negative upon increasing ϕ. The charge density should therefore depend on both potential and pH, since oxide coverage is pH–dependent [10].

The complex charging behaviour of Pt is not trivial to address theoretically; up until now, there is no existing *ab initio* method that addresses pH. As a first step towards the *ab initio* determination of the Pt surface charge as a function of potential and pH,

we present the generalized computational hydrogen electrode, a novel method that explicitly captures the pH and potential effects on the interface structure and its corresponding free energy [138, 139][1]. Using simple thermodynamic arguments, the method determines ground state interface structures as a function of pH and potential. As an example, we apply the method to a sample set of Pt(111)|water structures and determine the corresponding Pourbaix diagram.

While this method was motivated by charging of Pt, the scheme proposed is completely general to any atomistic metal|solution interface model. Electrochemical reaction rates can be strongly affected by solution pH, and there is increasing interest in the development of efficient electrocatalysts for alkaline environments [140, 141]. Consideration of pH is thus a crucial challenge in *ab initio* simulations of electrochemical intefaces. This method opens up the possibility of correctly addressing pH and potential effects on the structure and electrocatalytic activity of electrochemical interfaces.

We begin with a brief introduction to density functional theory and its application to electrocatalysis. We then describe the generalised computational hydrogen electrode, and apply it to a Pt(111)|water interface.

4.2 Density Functional Theory

This section provides an introduction to density functional theory (DFT). We have summarized relevant parts of Kohanoff's *Electronic Structure Calculations for Solids and Molecules* [142], which provides extensive discussion on the topics touched upon here.

DFT has been one of the most widely used methods for electronic structure calculations in quantum physics and chemistry in the past 20 years. The major advantage of DFT over other *ab initio* methods is its computational efficiency. As detailed below,

[1]The 2nd half of this chapter reproduces in revised form material from Ref. [139], with permission of the PCCP Owner Societies.

DFT maps the problem of the multi-electron wave function to one of electron density, which greatly reduces the degrees of freedom.

4.2.1 The Schrödinger Equation

All properties of a stationary system of solids and/or molecules can be derived from the solution of the time-independent Schrödinger equation,

$$\hat{H}\Psi_n(\mathbf{R},\mathbf{r}) = \varepsilon_n\Psi_n(\mathbf{R},\mathbf{r}) \ , \tag{4.1}$$

where $\mathbf{R} = (\mathbf{R}_1, \mathbf{R}_2, ...\mathbf{R}_P)$ are the nuclear coordinates, $\mathbf{r} = (\mathbf{r}_1, \mathbf{r}_2, ...\mathbf{r}_N)$ the electronic coordinates, ε_n the energy eigenvalues, Ψ_n the corresponding wave functions, and where the Hamiltonian is

$$\hat{H} = \hat{T}_n + \hat{T}_e + \hat{V}_{nn} + \hat{V}_{ee} + \hat{V}_{ext} \ . \tag{4.2}$$

The terms in the Hamiltonian are

$$\hat{T}_n = -\sum_{I=1}^{P} \frac{\hbar^2}{2M_I}\nabla_I^2 \qquad \text{(the nuclear kinetic energy)} \tag{4.3}$$

$$\hat{T}_e = -\sum_{I=1}^{N} \frac{\hbar^2}{2m}\nabla_i^2 \qquad \text{(the electronic kinetic energy)} \tag{4.4}$$

$$\hat{V}_{nn} = \frac{e^2}{2}\sum_{I=1}^{P}\sum_{J\neq I}^{P} \frac{Z_I Z_J}{|\mathbf{R}_I - \mathbf{R}_J|} \qquad \text{(the nuclear–nuclear interaction energy)} \tag{4.5}$$

$$\hat{V}_{ee} = \frac{e^2}{2}\sum_{i=1}^{N}\sum_{j\neq i}^{N} \frac{1}{|\mathbf{r}_i - \mathbf{r}_j|} \qquad \text{(the electron–electron interaction energy)} \tag{4.6}$$

$$\hat{V}_{ext} = -e^2\sum_{I=1}^{P}\sum_{i=1}^{N} \frac{Z_I}{|\mathbf{R}_I - \mathbf{r}_i|} \qquad \text{(the nuclear–electron interaction energy)} \tag{4.7}$$

The Schrödinger equation is thus an equation of $3(P+N)$ degrees of freedom, where P is the number of nuclei, and N the number of electrons. The difficulty in solving the problem arises from the two–body Coulomb interactions, which make the equation

inseparable. In practice, one applies a number of approximations to arrive at a solution.

4.2.2 The Born–Oppenheimer and Classical Nuclei Approximations

The first simplifying assumption is the Born–Oppenheimer approximation. The time scale of nuclei motion is in general much slower than that for electrons. The nuclei can thus be considered as stationary points in space, so that the total wave function is separable into nuclear and electronic wave functions,

$$\Psi_n(\mathbf{R},\mathbf{r}) = \Theta_n(\mathbf{R})\Phi_n(\mathbf{R},\mathbf{r}) \ . \tag{4.8}$$

The electronic Schrodinger equation is

$$\hat{h}_e\Phi_n(\mathbf{R},\mathbf{r}) = E_n(\mathbf{R})\Phi_n(\mathbf{R},\mathbf{r}) \ , \tag{4.9}$$

with the electronic Hamiltonian

$$\hat{h}_e = \hat{T}_e + \hat{V}_{ee} + \hat{V}_{ext} \ . \tag{4.10}$$

The second approximation is a classical treatment of the nuclei. By the Hellmann–Feynman theorem, the force on nuclei I is

$$\mathbf{F}_I = -\int \Phi_n^*(\mathbf{R},\mathbf{r})\frac{\partial\hat{h}_e(\mathbf{R},\mathbf{r})}{\partial\mathbf{R}_I}\Phi_n(\mathbf{R},\mathbf{r})d\mathbf{r} - \frac{\partial V_{nn}(\mathbf{R})}{\partial\mathbf{R}_I} \ . \tag{4.11}$$

Eq. (4.11) is minimized in the geometry optimization of the nuclei.

4.2.3 The Electronic Problem

The basis of density functional theory – the mapping of the ground state multi-electron wave function to one of electronic density – rests upon the Hohenberg and Kohn theorems:

1. There exists a one–to–one mapping between the electronic wave function and the electronic density $\rho(\mathbf{x})$.

2. For any V_{ext}, we can define an energy functional $E[\rho]$, and the $\rho(\mathbf{x})$ that minimizes this energy functional corresponds to the ground state $\rho_o(\mathbf{x})$.

In practice, $\rho_o(\mathbf{x})$ is determined via the Kohn–Sham scheme. The ansatz is a system of non-interacting electrons that reproduces the same $\rho(\mathbf{x})$ as the interacting system, i.e.

$$\rho(\mathbf{r}) = 2\sum_{i=1}^{N_s} |\phi_i|^2 \tag{4.12}$$

where $N_s = N/2$, the number of doubly occupied orbitals[2], and ϕ_i the single particle orbitals. The electronic wave function is constructed by a Slater determinant to ensure antisymmetry under exchange,

$$\Phi(\mathbf{r}) = \frac{1}{\sqrt{N_s}} \begin{vmatrix} \phi_1(\mathbf{r}_1) & \phi_2(\mathbf{r}_1) & \cdots & \phi_{N_s}(\mathbf{r}_1) \\ \phi_1(\mathbf{r}_2) & \phi_2(\mathbf{r}_2) & \cdots & \phi_{N_s}(\mathbf{r}_2) \\ \vdots & \vdots & \ddots & \vdots \\ \phi_1(\mathbf{r}_{N_s}) & \phi_2(\mathbf{r}_{N_s}) & \cdots & \phi_{N_s}(\mathbf{r}_{N_s}) \end{vmatrix} . \tag{4.13}$$

ϕ_i are the N_s lowest energy eigenfunctions of the one-electron Schrödinger equation with an effective potential V_{eff}, i.e., the Kohn–Sham equations,

$$\hat{H}_{KS}\phi_i(\mathbf{x}) = \varepsilon_i\phi_i(\mathbf{x}), \;\; \hat{H}_{KS} = -\frac{\hbar^2}{2m}\nabla^2 + V_{eff}(\mathbf{x}) \; . \tag{4.14}$$

[2]for treatment of spin-polarized systems, please see Ref. [142].

V_{eff} contains the external (including nuclear-electron interaction), the classical electrostatic Hartree, and the exchange and correlation contributions,

$$V_{eff} = V_{ext} + \int \frac{\rho(\mathbf{x}')}{|\mathbf{x}-\mathbf{x}'|} d\mathbf{x}' + \frac{\delta E_{xc}[\rho]}{\delta \rho} \ . \tag{4.15}$$

The exchange energy arises from the Pauli exclusion principle, i.e. no two electrons can occupy the same quantum state. Correlation refers to the reduced probability of finding an electron in the vicinity of another. The exact form of the E_{xc} functional is unknown, and must be approximated. As shown in Eq. (4.15), V_{eff} is dependent on ρ and hence the one–electron solutions. Therefore, the ϕ_i's must be found by self–consistent solution so that the ρ used to construct V_{eff} coincides with them via Eq. (4.12). The total energy, in terms of ϕ_i and ρ, is

$$E = -\frac{\hbar^2}{m} \sum_{i=1}^{N_s} \int \phi_i^* \nabla^2 \phi_i d\mathbf{x} + \int \rho(\mathbf{x}) V_{ext}(\mathbf{x}) d\mathbf{x} + \frac{1}{2} \int \int \frac{\rho(\mathbf{x})\rho(\mathbf{x}')}{|\mathbf{x}-\mathbf{x}'|} d\mathbf{x} d\mathbf{x}' + E_{xc}[\rho] \ , \tag{4.16}$$

with contributions from the kinetic energy of the non-interacting electrons, the nuclear–electron interaction, the classical Hartree interaction, and exchange and correlation. Fig. 4.1 shows a flowchart of the determination of the ρ, ϕ_i via the Kohn-Sham scheme, as well as nuclei geometry optimization.

4.2.4 Exchange and Correlation Functionals

There are two major approximations for $E_{xc}[\rho]$, the local density approxmation (LDA), and the generalised gradient approximation (GGA). LDA is the simplest approximation to the exchange and correlation energy. This approximation applies locally the exchange and correlation functionals corresponding to a homogenous electron gas,

$$E_{xc}^{LDA} = \int \rho(\mathbf{x}) \varepsilon_{xc}^{homo}[\rho] d\mathbf{x} \ . \tag{4.17}$$

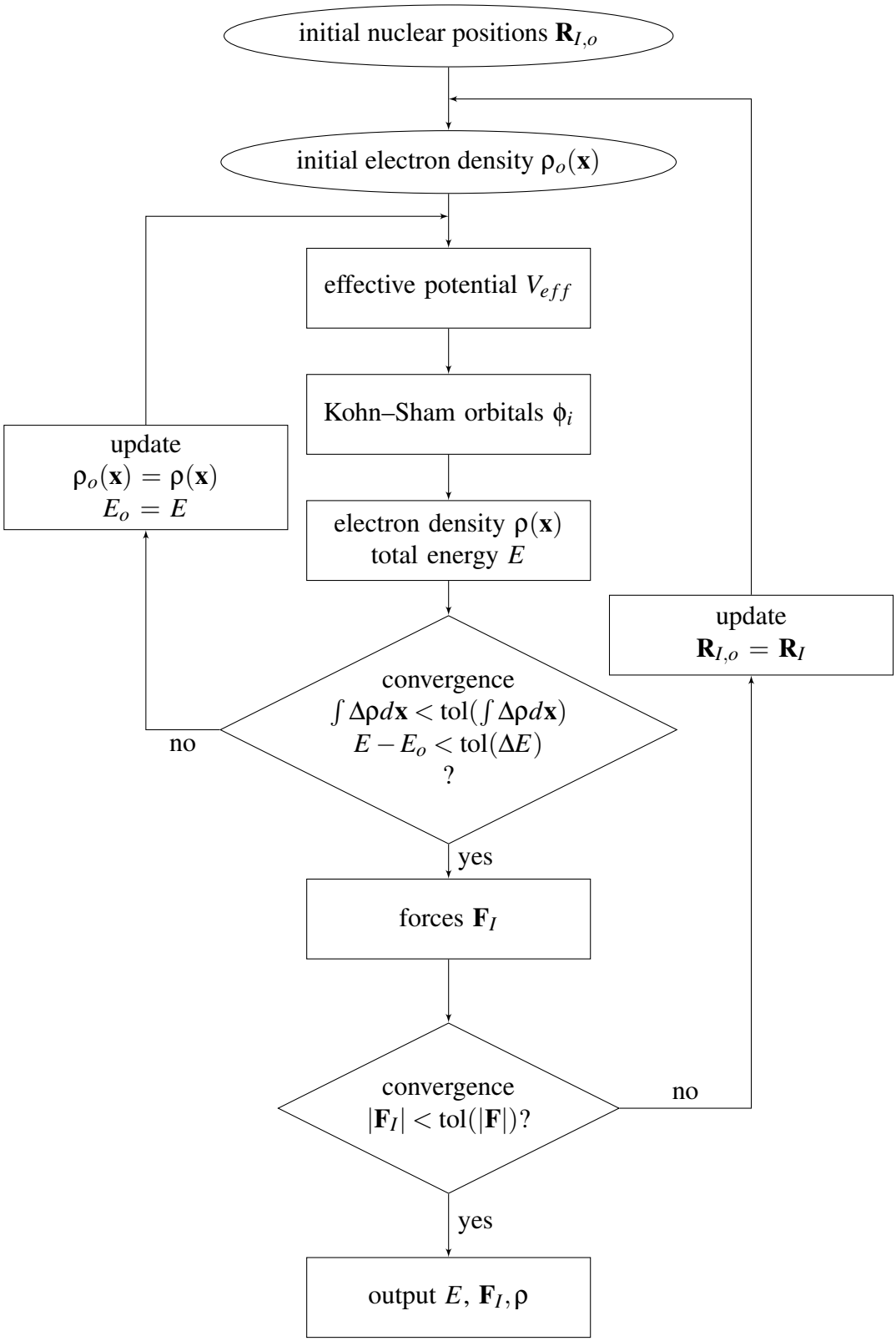

Figure 4.1: Flowchart of the determination of ρ via Kohn-Sham scheme, nuclei geometry optimization

LDA performs well for systems with uniform electronic density, such as bulk metals, but not for adsorbates, where the binding energy is often overestimated. LDA performs very poorly for hydrogen bonded or Van der Waals systems, where binding is dominated by density inhomogeneities. GGA provides a correction for inhomogeneities in ρ via an expansion of the density in terms of the gradient,

$$E_{xc}^{GGA} = \int \rho(\mathbf{x})\varepsilon_{xc}^{homo}[\rho]F_{xc}[\rho,\nabla\rho]d\mathbf{x}\,. \tag{4.18}$$

In this chapter, we apply the "revised Perdew–Burke–Ernzerhof" (RPBE) flavor of GGA, which provides accurate chemisorption energies [143].

4.2.5 DFT Implementation

Calculations discussed below were performed with either the Dacapo[3] [144] or GPAW (Grid based projector augmented wave method) [145, 146] DFT packages.

Pseudopotentials and the PAW method

A major challenge in DFT implementation is the strong Coulomb potential, which leads to sharp oscillations in the wave functions close to the nuclei. However, since chemical properties are determined mostly by valence electrons, approximations can be made for the core region.

In Dacapo, the core region is treated with pseudopotentials, illustrated in Fig. 4.2(a). A pseudopotential is an effective, smooth potential that accounts for the core electrons. Outside a certain cut-off radius, the pseudopotential is constructed to coincide with real potentials and reproduce the correct wave functions.

In GPAW, the core electrons are dealt with via the projected augmented wave (PAW) method under the frozen core approximation, illustrated in Fig. 4.2(b). This method

[3] All Dacapo calculations used were performed by Mårten Bjorketün.

transforms the one–electron wave functions into pseudo–wave functions that are smooth near the cores, the "augmentation spheres" region. This transformation results in a modified Kohn–Sham system. The frozen core approximation assumes the core electrons to be localised within the augmentation spheres, so that only valence states are solved for. The advantage of PAW over pseudopotential methods is that all wave functions can be obtained from the inverse transformation of the pseudo–wave functions.

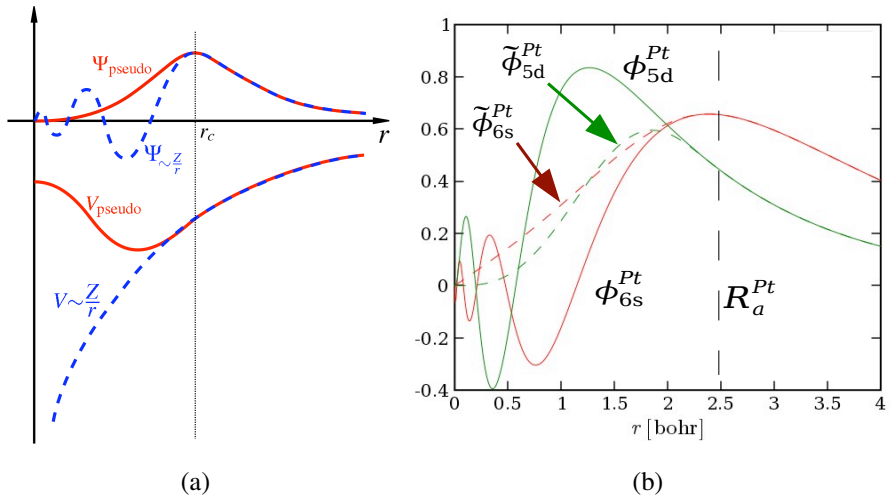

(a) (b)

Figure 4.2: (a) Outside a certain cut–off radius r_c, the pseudopotential is identical to the actual potential and reproduces the correct wave function. (b) In the PAW method, pseudo–wave functions are smoothed out inside the augmented sphere of radius R_a and identical to actual wave functions outside. Reproduced from Ref. [147].

Discretisation

A further difference in the Dacapo and GPAW implementations is in the discretisation of the Kohn–Sham equations. Dacapo applies a plane wave basis set to a cutoff frequency, while GPAW uses finite differences on a real space grid (GPAW). Increased accuracy is obtained via higher cut-off frequencies and finer grids, respectively. The advantage of real space methods is the possibility of parallelization over the domain for large model systems.

Brillouin zone sampling

Wave functions for infinite, periodic systems are represented by periodic Bloch functions,

$$\phi_{n\mathbf{k}}(\mathbf{x}) = \exp(i\mathbf{k}\cdot\mathbf{x}) f_{n\mathbf{k}}(\mathbf{x}) \tag{4.19}$$

where $f_n(\mathbf{x})$ has the periodicity of V_{ext} and n is the band index. Total energies and densities are determined by integrals over all $\mathbf{k}$–points in the Brillouin zone. In practice, the integral is approximated over a finite set of $\mathbf{k}$–points. We apply Monkhorst–Pack grids, which samples $\mathbf{k}$–points evenly over the Brillouin zone.

4.2.6 DFT Applications to Electrochemistry

Recent developments in DFT calculations on electrochemical systems have driven the development of new electrocatalysts [148–150]. Currently, there are two main types of *ab initio* studies on electrochemical systems. Catalyst screening/optimization studies focus on adsorption free energies of reaction intermediates. Water and electric fields are often omitted to reduce the use of computational resources [151], and the effect of potential is added *a posteriori* via the computational hydrogen electrode [138]. The other type is more fundamental and focusses on setting up explicit electrode potentials and electric fields at the interface, via water layers, excess free charge, counter-ions, and counter electrodes [152–156].

In what follows, we describe the computational hydrogen electrode and the methods to set up explicit electrode potentials, charge densities and fields.

Computational Hydrogen Electrode

The computational hydrogen electrode (CHE) is a simple and elegant method to account for the impact of electrode potential on adsorbate species without the explicit treatment of the solvent and solvated protons [138, 157, 158]. The potential is defined relative to

the standard/reversible hydrogen electrodes, based on the hydrogen oxidation/evolution reaction,

$$\mathrm{H^+ + e^- \leftrightarrow {}^1\!/\!_2 H_2}\ . \tag{4.20}$$

The sum of the electrochemical potentials of protons and electrons can be written

$$\mu_{\mathrm{H^+ + e^-}} = \mu^o_{\mathrm{H^+}} + kT \ln a_{\mathrm{H^+}} + e\phi^S + \mu^o_{\mathrm{e^-}} - e\phi^M \tag{4.21}$$

where ϕ^M and ϕ^S are the metal and solution phase potentials, respectively, $a_{\mathrm{H^+}}$ is the activity of protons, subscript o stands for standard conditions, and we have introduced for compactness the notation $\mu_{\mathrm{H^+ + e^-}} = \mu_{\mathrm{H^+}} + \mu_{\mathrm{e^-}}$.

At electrochemical equilibrium, under standard conditions, $a_{\mathrm{H^+}} = 1$, $\phi^M = \phi^{M,o}_{eq}$ and $\mu_{\mathrm{H^+ + e^-}} = {}^1\!/\!_2\mu_{\mathrm{H_2}}$. Therefore, Eq. (4.21) can be written

$$\mu_{\mathrm{H^+ + e^-}} = {}^1\!/\!_2\mu_{\mathrm{H_2}} - e(\phi^M - \phi^{M,o}_{eq}) + kT \ln a_{\mathrm{H^+}}\ , \tag{4.22}$$

$$= {}^1\!/\!_2\mu_{\mathrm{H_2}} - eU_{\mathrm{SHE}} - 2.3kT\,\mathrm{pH}\ = {}^1\!/\!_2\mu_{\mathrm{H_2}} - eU_{\mathrm{RHE}}. \tag{4.23}$$

where U_{SHE} and U_{RHE} stands for the electrode potential measured relative to SHE and RHE. Eq. (4.23) allows us compute free energies of reactions involving proton and electron transfer without having to consider the protons, solvent structure, or interfacial free charge explicitly. For example, consider the first step in oxygen reduction [138],

$$\mathrm{O_2 + H^+ + e^- \rightarrow OOH}\ , \tag{4.24}$$

which has the reaction energy

$$\Delta G = \mu_{\mathrm{OOH}} - \mu_{\mathrm{O_2}} - \mu_{\mathrm{H^+ + e^-}} \tag{4.25}$$

$$= \mu_{\mathrm{OOH}} - \mu_{\mathrm{O_2}} - ({}^1\!/\!_2\mu_{\mathrm{H_2}} - eU_{\mathrm{RHE}})\ . \tag{4.26}$$

Chemical potentials μ_{OOH}, μ_{O_2} and $^1/_2\mu_{H_2}$ are all easily obtained via DFT and standard molecular tables, and the effect of potential and pH is added via the $-eU_{RHE}$ term. This method assumes that pH, electric fields, and solvent have negligible effects on the adsorbate structures used to calculate the reaction energy [151].

Explicit Treatment of Potential, Fields, Surface Charge and Solvent

In the past decade or so, there have been several methods proposed to treat the electrode potential, fields, charge, and solvent explicitly. These methods are of particular importance to the calculation of activation energies of proton/ion transfer, where the solvent structure is involved. In all cases, the potential relative to SHE is found via the metal|solution work function, measured with respect to vacuum just outside the solution phase [159, 160],

$$U_{SHE} = \frac{\Phi_{e^-} - \Phi_{e^-}(SHE)}{e}. \tag{4.27}$$

The work function of the standard hydrogen electrode has the experimentally determined value of 4.44eV [159].

The methods treat the counter–ions differently. In Neurock *et al.*'s approach, a homogeneous background charge is applied to metal|solution systems to counter the charge at the metal surface [152]. Sugino *et al.*'s "effective screening medium" method adds a counter electrode with infinite dielectric constant across from a charged Pt(111)| water system [154]. Anderson and Marzari *et al.* have implemented hybrid *ab initio*/continuum methods, where the solvent is treated implicitly via a Poisson Boltzmann equation [104, 161]. Rossmeisl *et al.*'s approach is fully *ab initio*, with a model system of a metal slab with 1–3 water layers [153, 162]. Excess H is added to the water layers, which spontaneously separates into H^+ in solution and e^- in the electrode upon optimization.

In all these approaches, the water structures and corresponding dipole orientations

are rather arbitrary, and the effect of pH and these structures is not considered. The generalised computational hydrogen electrode we introduce below is required to determine the appropriate solvent structure as a function of potential and pH.

4.3 The Generalised Computational Hydrogen Electrode

To introduce the generalised computational hydrogen electrode, we rewrite Eq. (4.23) in terms of work functions (Eq. 4.27), and set the reference chemical potential $\mu_{H_2} = 0$,

$$\mu_{H^+ + e^-} = -2.3kT \cdot \mathrm{pH} - \Phi_{e^-} + \Phi_{e^-}(\mathrm{SHE}). \tag{4.28}$$

Fig. 4.3(a) maps out Eq. (4.28) in red iso-pH lines on the $(\Phi_{e^-}, \mu_{H^+ + e^-})-$plane. The core of the method presented here is: for a given metal|solution structure, if Φ_{e^-} and $\mu_{H^+ + e^-}$ are known, the corresponding pH is determined via Eq. (4.28).

We now describe an extrapolation scheme to determine the integral free energy, G^{int}, of interfacial structures on the $(\Phi_{e^-}, \mu_{H^+ + e^-})-$plane. For a given structure, Φ_{e^-} is fixed by its interface dipole. The free energy per surface metal atom at electrochemical equilibrium, $\mu_{H^+ + e^-} = 0$, is

$$G^{\mathrm{int}}(\mu_{H^+ + e^-} = 0, \Phi_e^-) = \frac{G_{N,n} - G_{N,0}}{N} - \frac{1}{2}\frac{n}{N} G_{H_2}\ , \tag{4.29}$$

where n is the number of hydrogens (as $H^+ + e^-$, or as adsorbates, H_{ad}, OH_{ad}, and O_{ad}), N the number of surface metal atoms, $G_{N,n}$ the free energy of the metal|solution system of interest, $G_{N,0}$ the free energy of a reference system with no ions nor adsorbates, and G_{H_2} the free energy of gas-phase H_2 under standard conditions. All G are straightforward to obtain via DFT and standard tables. If oxide species are present, i.e. H is removed from the water of the reference system, n can be negative. The corresponding pH can be calculated from Eq. (4.28). G^{int} for the interface at other pH, where

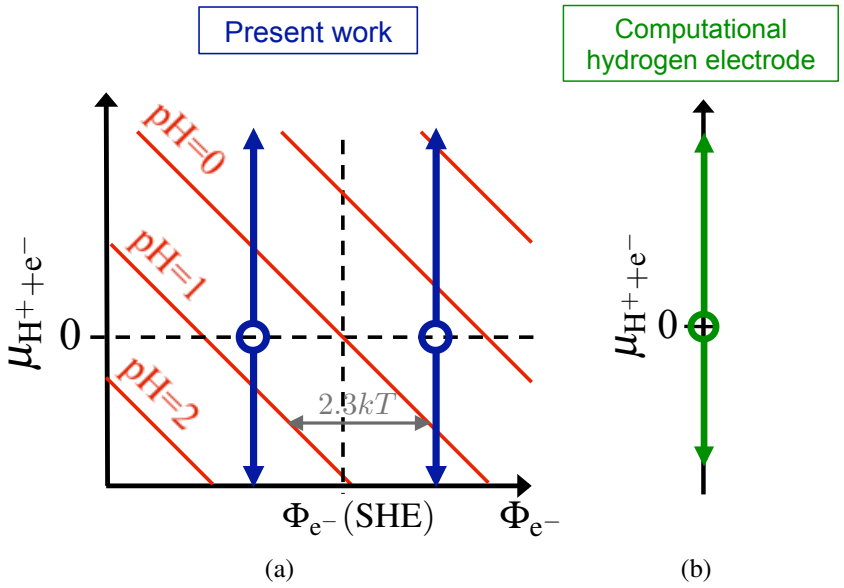

Figure 4.3: (a) Eq. (4.28) mapped as red iso-pH lines on the $(\Phi_{e^-}, \mu_{H^+ + e^-})-$plane. Extrapolations of G^{int} vs. $\mu_{H^+ + e^-}$ of the present work in blue arrows, where Φ_{e^-} is fixed by the interfacial structure. (b) Extrapolation of G^{int} vs. $\mu_{H^+ + e^-}$ of the computational hydrogen electrode in green arrows, where Φ_{e^-} is not considered.

$\mu_{H^+ + e^-} \neq 0$, is given by the linear extrapolation,

$$G^{int}(\mu_{H^+ + e^-}, \Phi_{e^-}) = G^{int}(\mu_{H^+ + e^-} = 0, \Phi_{e^-}) - \frac{n}{N} \cdot \mu_{H^+ + e^-} \ , \tag{4.30}$$

Fig. 4.3(a) illustrates, on the $(\Phi_{e^-}, \mu_{H^+ + e^-})-$plane , the extrapolation for two interface structures of different Φ_{e^-}, in blue arrows. For any given system, this extrapolation is performed at constant Φ_{e^-}.

At any given Φ_{e^-} and pH, the relevant ground state structure corresponds to that with minimum G^{int}. To map out ground state metal|solution interfacial structures at a range of Φ_{e^-} and $\mu_{H^+ + e^-}$ (or pH), a representative set of interfacial structures of varying charge density, adsorbate coverage, and water dipoles should be considered. Electric fields that are consistent with pH and potential are automatically set up.

Fig. 4.3 shows the distinction between the G^{int} extrapolations of the present work (a,

blue arrows) and the computational hydrogen electrode (b, green arrows) [138]. Computational hydrogen electrode calculations do not consider the work function Φ_{e^-}, and extrapolation of G^{int} to $\mu_{H^+ + e^-} \neq 0$ are all done along a single line. The effect of potential is only considered via $\mu_{H^+ + e^-} = -eU_{\text{RHE}}$, not in any changes in the physical dipole at the interface. Effects of water structure and interface electric fields on G^{int} are therefore neglected. In the present analysis, we consider explicitly Φ_{e^-} as fixed by the interface dipole, and map out G^{int} on the $(\Phi_{e^-}, \mu_{H^+ + e^-})-$plane at the given Φ_{e^-}. This approach thereby distinguishes contributions of potential and pH to $\mu_{H^+ + e^-}$. Water structures and electric fields that are consistent with the pH and potential are automatically included. We discuss below the implications of the current analysis on previous results.

The present analysis is general in that it places no restrictions on the atomic interface model considered, and that any atomic scale simulation of the electrochemical interface must include this analysis in order to explicitly and correctly account for pH and potential. With interface and bulk protons at electrochemical equilibrium, $\mu_{H^+}(\text{interface}) = \mu_{H^+}(\text{bulk})$, we can consider interface models with a limited number of water layers, provided that they fully screen the interface electric fields [153, 162].

To illustrate the method, we apply it to a variety of Pt(111)|water structures and determine the corresponding Pourbaix diagram. We consider 1-2 layers of ice-like hexagonal water structures [153, 160, 163] of a range of dipole orientations, adsorbate coverages (H_{ad}-covered, bare Pt, a dissociated water layer of 1/3 OH coverage), and H^+ concentrations. All model systems were charge neutral, such that the positive charge of H^+'s was balanced by a negative surface charge on the metal. The total number of model systems considered is 110.

4.4 Calculation details

DFT calculations were carried out with the Dacapo or GPAW code, integrated with the Atomic Simulation Environment [144, 145, 164, 165]. The density cutoff for plane wave Dacapo calculations was 350eV while the grid spacing for GPAW real-space calculations was 0.2Å. We have chosen Rossmeisl *et al.*'s fully *ab initio* approach to setting up an explicit potential [153, 162]; it does not rely on artificial background charges or counter–electrode slabs with set up an artificial field outside the metal slab, and it reproduces the expected capacitance of a bare Pt slab. All systems contained a periodic 3-layer Pt(111) slab and 1-2 water bilayers with at least 12Å vacuum in the direction perpendicular to the surface. An optimized Pt lattice constant of 4.02Å was used in all calculations. Unit cells of sizes (3x2), (3x3), (3x4), (3x6), and (6x4) were sampled with Monkhorst-Pack k-point grids (4x6), (4x4), (4x3), (4x2), and (2x3). In all cases, a dipole correction was applied [166]. The two bottom layers were constrained and all other atoms relaxed until the forces on them were less than 0.05eV/Å. To obtain the free energies G, the zero point energies and entropies of protons and adsorbed hydrogens were taken from Refs. [138, 162]. The reference energy structure corresponding to $G_{N,0}$ was a bare slab with water layer(s) of neutral dipole orientation (equal density of H-up and H-down waters).

4.5 Pt(111)|water example

Fig. 4.4 shows G^{int} for three sample Pt(111)|water structures. G^{int} was linearly extrapolated at the three corresponding Φ_{e^-} with Eq. (4.30). Constant pH = 0, 7, 14 planes are mapped out perpendicular to the $(\Phi_{e^-}, \mu_{H^+ + e^-})-$plane (Eq. 4.28). Intersections of the 3 lines with the pH planes are highlighted with flat circles, marking the G^{int} of the 3 structures at those particular pH.

Figs. 4.5(a) and (b) show the full set of considered water structures as projections of

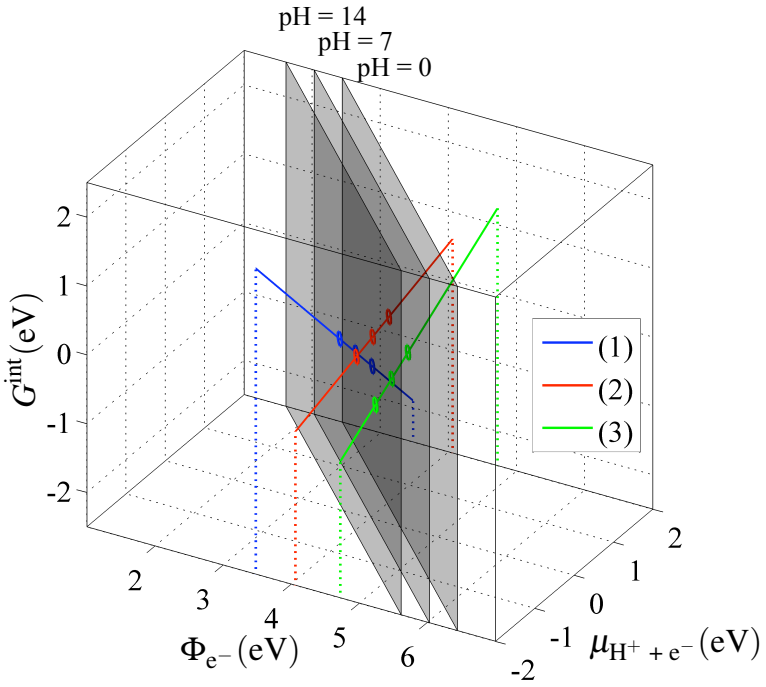

Figure 4.4: (Color online) Calculated G^{int} vs. Φ_{e^-} , $\mu_{H^+ + e^-}$, for select Pt(111)|solution interfacial structures: (1) Φ_{e^-} = 3.48eV, n/N = 0.98, (2) Φ_{e^-} = 4.06eV, n/N = −0.22, (3) Φ_{e^-} = 4.72eV, n/N = −0.44eV. Dashed lines are shown as guides for the eye. Intersections of G^{int} with constant pH = 0, 7, 14 planes are marked with circles, indicating G^{int} at those particular pH.

G^{int} onto the pH = 0 and 14 planes, respectively. The SHE scale is shown along the bottom x-axes, and the RHE along the top. The legend shows the dipole orientation of the water structure, with H-up water indicated by ↑ and H-down by ↓. The H concentration, n/N, is indicated by the colorbar.

We obtain a simple Pt(111)|water Pourbaix diagram by interpolating the results for select proton/adsorbate coverages, $n/N = -0.33$, 0, 0.17, 1, and 1.17. For these coverages, we fit straight lines through the G^{int} vs. potential data at a range of pH (cf. Fig. 4), and linearly interpolate both the G^{int} and dipole orientation. Then, at every U and pH, we pick out the most stable structure. The resultant Pourbaix diagram is shown in Fig. 4.6.

Consistent with experimental cyclic voltammograms and Pourbaix diagrams [167,

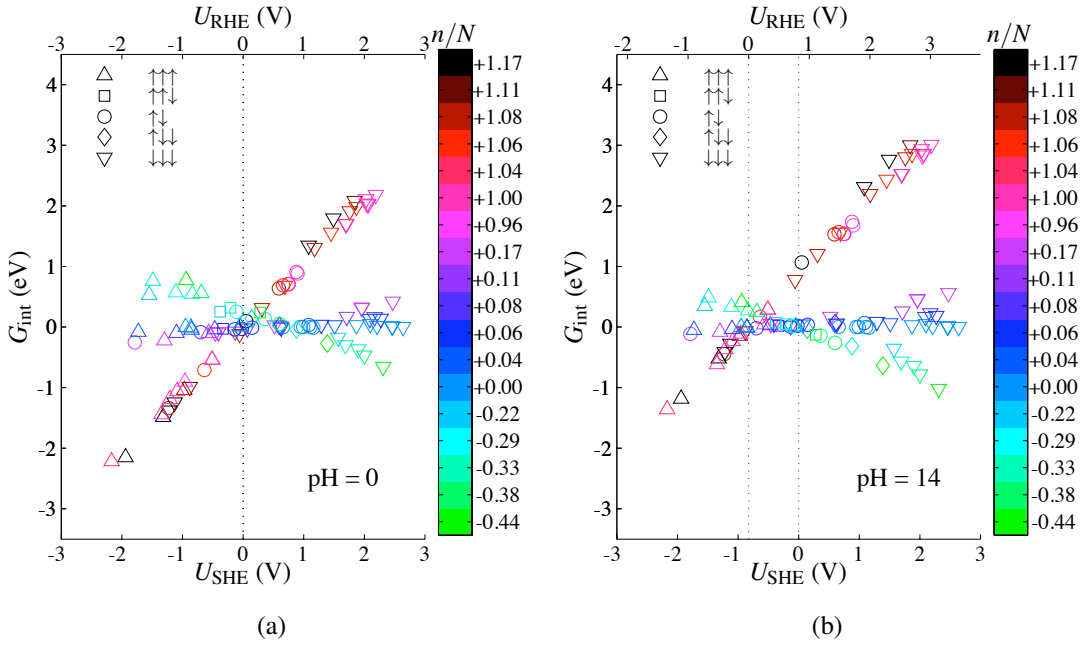

Figure 4.5: (Color online) Calculated G^{int} vs. U (vs. SHE and RHE) for all considered Pt(111)|solution interfacial structures, as projected onto (a) pH = 0 and (b) pH = 14 planes. The H concentration, n/N is indicated by the colorbar, and the net dipole of the water by arrows.

168], increasing U leads to a shift from a H_{ad} to OH_{ad} covered surface. The $-2.3kT$/pH (-0.059eV/pH) slope in the dotted lines dividing regions of different coverages show the expected U_{RHE} dependence of adsorbate coverage. Generally, as U increases and the surface transitions from H_{ad} to OH_{ad} covered, water orientation tends to shift from H-up to H-down; this maximises the hydrogen bonding between the adsorbates and water layer [169, 170]. Water orients from H-down to H-up as pH increases, i.e. at low pH, H's tend to point toward the Pt surface. This trend is in agreement with that suggested by impedance spectroscopy [171].

The Pt(111)|water example illustrates how pH and U affect the metal|solution interfacial structure. Essentially, the electrochemical potentials of both the protons and electrons are required to determine the ground state interfacial structure. Any U can be set up by a variety of adsorbate coverages, surface charge densities, and water dipole

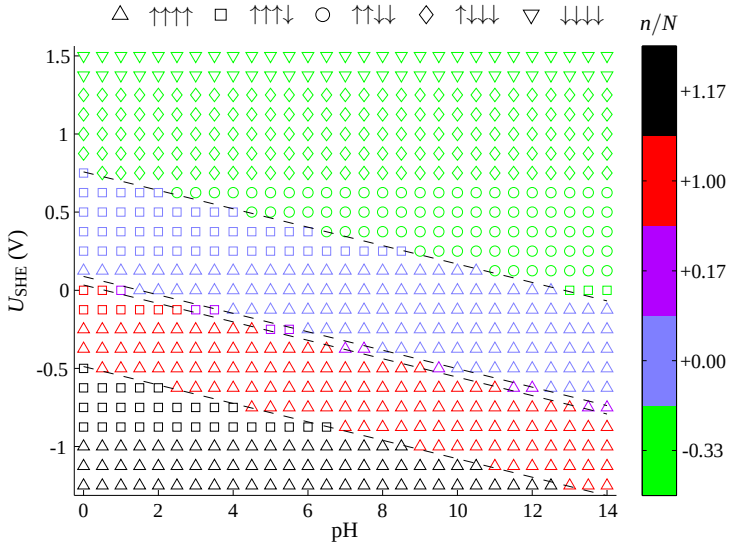

Figure 4.6: (Color online) Simulated Pourbaix diagram for Pt(111), showing the minimum energy structures as a function of pH and U_{SHE} for select excess H concentration n/N. Dotted lines dividing regions of different coverages have a -0.059eV/pH slope, indicating the expected U_{RHE} dependence of adsorbate coverage.

orientations. The electrochemical potential of the proton, determined by the pH, picks out the relevant minimum energy structure for a given U.

This new insight into the effect of pH on the interfacial structure does not necessarily invalidate previous computational hydrogen electrode studies, as long as the adsorbates of interest show negligible interactions with electric fields and water [151, 172]. In this case, for a given adsorbate coverage, only differences in the water orientation contribute to the variation of G^{int} with Φ_{e^-}, and such contributions are negligible[1] compared to those of adsorbate binding energies. G^{int} then depends mainly on $\mu_{\mathrm{H}^+ + \mathrm{e}^-}$, not Φ_{e^-}, i.e. $G^{\mathrm{int}} \approx f(\mu_{\mathrm{H}^+ + \mathrm{e}^-}) = f(-eU_{\mathrm{RHE}})$. This leads to a simple U_{RHE} dependence of adsorbate coverage, as is the case for $\mathrm{H_{ad}}$ and $\mathrm{OH_{ad}}$ on Pt, considered above. G^{int} obtained via a computational hydrogen electrode and the present extrapolation (cf. Fig. 4.3) would then be very similar, even though water structures considered previously, if any, were

[1] $G^{\mathrm{int}}(\mu_{\mathrm{H}^+ + \mathrm{e}^-} = 0)$ differences among neutral water layers of various dipoles are < 0.1eV.

likely not consistent with the ground state structures at the assumed pH and U. Where adsorbates are highly affected by field and/or water structure, e.g. adsorbates with substantial dipole moments [172], and/or where adsorbate coverages do not show a simple U_{RHE} dependence [173], the present analysis is required.

In reaction barrier studies, pH can have an important effect, as the barriers may be highly dependent on water structure. The ground state structures determined above could, for instance, explain the dramatically higher rates of hydrogen evolution on Pt in acidic solution than in basic ones [140, 141]. At relevant electrode potentials and low pH, some hydrogens point toward the surface, which results in a very small barrier for proton transfer. At higher pH, all hydrogens point away from the surface, which gives rise to an extra barrier.

We have focussed on a simple model system of Pt(111)|water to illustrate the method. We expect more complex model systems with extended water layers, anions, and oxide species to further demonstrate the capabilities of the model.

In principle, the surface charge density of Pt as a function of pH and U can be mapped with this method; the challenges are that realistic charge densities require unit cells of very large size, and stable water structures of general Pt(*hkl*) surfaces (aside from (111) [163], which has stable ice-like structures) are not known. Assuming a standard Helmholtz capacitance of 20μF/cm^2 in polycrystalline Pt, the surface charge densities at $|\phi - \phi^{pzc}| = 0$ to 0.4V would be 0–0.8$\times 10^{-5}$ C/cm^2. We expect surface charge densities within this range at relevant fuel cell operating potentials, since there are ϕ^{pzc} associated with both bare and oxidized Pt at a given pH [98, 137]. Currently, we have included a few 3x6x3 and 6x4x3 unit cell calculations. The minimum charge density (aside from 0C/cm^2) we can calculate with these cells, assuming 1H$^+$ in the water and 1 excess e$^-$ in the metal within the cell, would be of 1.26 and 0.95 $\times 10^{-5}$ C/cm^2, respectively. We would thus require even larger unit cells to map out the charge density at relevant potentials, or, to implement perhaps an *ab initio*/continuum model

hybrid model system, so that partial charges can be handled within small unit cells [104, 161] .

4.6 Summary

In summary, we have presented a simple scheme to determine the relevant interfacial structure at a given potential and pH, based on thermodynamic arguments. For any given interfacial structure containing any reaction intermediate of interest, the only required inputs to the analysis are the electron work function and the integral free energy, both easily determined with standard DFT. Applying the scheme to Pt(111)|water as an example, we show the pH to affect the adsorbate coverage and water orientation, which is expected to have an important impact on charge transfer reaction barriers. The method paves the way for *ab initio* studies of pH, field, and surface charge effects on the structure and electrocatalytic activity of electrochemical interfaces.

Chapter 5

Water Balance Model of UTCLs

Membrane electrode assemblies (MEAs) that employ 3M NSTF on the cathode side exhibit increased water management challenges. 3M NSTF MEAs show poor performance at low RH and low temperatures, and an increased propensity for cell reversal under load transients, i.e. a decrease of the cathode voltage to < 0V when the current density is abruptly ramped from close to 0 to 1A/cm^2 [67, 69, 70].

The causes of the water management issues in UTCL MEAs are not well established. Recent modeling work of UTCL MEAs consider only vapor diffusion in the gas diffusion layers, and attribute poor steady state performance and cell reversal during load transients to the flooding of the catalyst layers; effective oxygen diffusion coefficents were assumed to be zero once the UTCL saturates [67, 68]. However, both a simple consideration of the diffusion length of O_2 in flooded pores and modeling studies of flooded UTCLs [2] that include realistic diffusion coefficients of oxygen in water show that flooded CLs should not lead to limiting current behaviour or MEA shutdown. In fact, the ionomer–free UTCLs require water for proton conduction. In this work, we postulate that the primary cause of poor performance in MEAs with UTCLs arises from the flooding of the GDL, not CL.

We study water transport in MEAs containing UTCLs using a simple one–dimensional

water balance model of the MEA. We extend the half–PEFC model by Baghalha and Eikerling [15] to consider liquid water transport in the anode and vaporization in the GDL via a transmission line model of water fluxes [174]. The model relates transport properties and operating conditions to capillary pressure distributions, current density, liquid and vapor water fractions out the anode and cathode, and the onset of catalyst layer and GDL flooding. We evaluate strategies for increasing the current density for the onset of GDL flooding and discuss methods to identify regimes of transport via water flux measurements.

5.1 Model Formulation

5.1.1 Model Assumptions

We consider a 1D water balance model approach [15] to water fluxes in the UTCL MEA. Figure 5.1 shows a schematic of the MEA and the water fluxes. Red arrows show the sources of water in the cathode catalyst layer (cCL), i.e. the electro–osmotic drag of water across the PEM and oxygen reduction. Blue arrows show fluxes of water away from the cCL, via permeation, vaporization, and subsequent diffusion.
We make the following simplifying assumptions:

(i) We consider only steady state operation under isothermal conditions.

(ii) Flow rates in flow field channels are high, such that relative humidities (RHs) at the MEA boundaries are fixed and liquid water does not accumulate in the channels.

(iii) Total gas pressures at the anode and cathode, p_a^G and p_c^G, are constant, due to high convective flux of gases in the diffusion media.

(iv) GDLs are treated with a transmission line model of coupled liquid and vapor fluxes [174]. We make a 3–state approximation for the capillary pressure–saturation

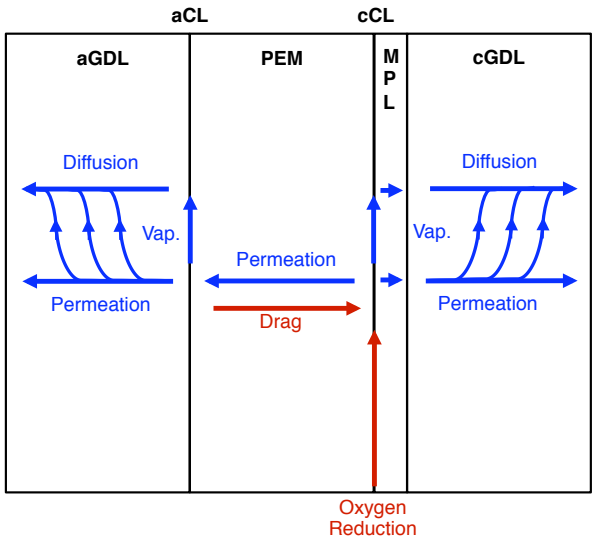

Figure 5.1: Schematic of water transport paths in the MEA. GDL = gas diffusion layer, MPL = microporous layer, CL = catalyst layer, PEM = polymer electrolyte membrane. a and c indicate anode and cathode, respectively. Red arrows show the sources of water in the cCL, i.e. the electro–osmotic drag of water across the PEM and oxygen reduction. Blue arrows show fluxes of water away from the cCL, via permeation, vaporization, and subsequent diffusion.

curves of the GDLs, illustrated in Fig. 5.2. Saturation and liquid permeability are zero at capillary pressure $p^c < 0$, constant at $0 \leq p^c < p^c_{GDL,fl}$, and reaching flooded conditions with maximal saturation at $p^c = p^c_{GDL,fl}$.

(v) The cathode microporous layer (MPL) has constant vapor diffusivity and liquid permeability. Negligible vaporization occurs in the MPL.

(vi) Anode and cathode catalyst layers (aCL and cCLs) are approximated as infinitesimally thin interfaces. The CLs flood at a negative capillary pressure, since they are hydrophilic.

(vii) Water is transported through the PEM via electro-osmotic drag and hydraulic permeation, with constant drag coefficient n_{eo} and permeability that depends linearly on water content, w [175].

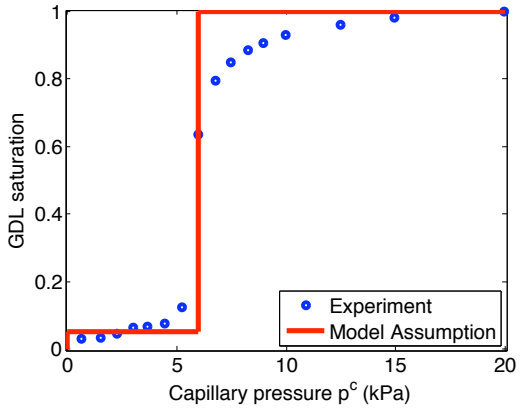

Figure 5.2: 3–state approximation for the capillary isotherm of the GDLs. Saturation and liquid permeability are zero at capillary pressure $p^c < 0$, constant at $p^c \geq 0$, and reaching flooded conditions with maximal saturation at $p^c = p^c_{GDL,fl}$. Experimental data adapted from Ref. [16], where the capillary isotherm was measured for the entire diffusion medium, GDL + MPL. We assumed that the measured variation in saturation was mainly due to GDL saturation. Capillary pressures required to penetrate the nanosized, hydrophobic pores of the MPL were considered to be high. We further assumed that the entire GDL is saturated at the maximum capillary pressure applied, and normalized the data to the saturation at this maximum capillary pressure.

In (iv), we neglect dynamic breakthrough and eruptive transport phenomena [176, 177], as well as hysteresis arising from the mixed wettability of the GDLs [16].

In (v), we assume that water flows through hydrophilic cracks in the MPL [16, 178]. Given the nanometer-sized (10–100nm) and hydrophobic MPL pores [179], we do not consider flooding in the MPL, and assume vaporization rates in it to be negligible. We do not include an MPL at the anode side [71].

In (vi), the interface assumption is based on the 2–3 orders of magnitude lower thickness of the UTCLs compared to the other MEA components, which should result in essentially constant pressure distributions along the UTCL thickness. Therefore, unlike conventional CLs, the UTCL plays little role in steering of liquid fluxes within the MEA [18, 180]. The assumption of a single flooding capillary pressure in the UTCL corresponds to assuming it to have monodisperse pores.

In (vii), we neglect water transport via diffusion in the PEM, though its effect could be incorporated into the hydraulic permeation term [29].

The above assumptions could be relaxed in a more complex, all-encompassing model [181]. However, such models require a detailed knowledge of transport parameters and properties of MEA components, which are not available for 3M NSTF MEAs. The focus of the present work is on the qualitative trends and results, not in the exact reproduction of fluxes and pressure distribution within any particular MEA.

5.1.2 Regimes of Transport

With the assumed model of the GDL, there are three regimes of water transport at each electrode, denoted as

- regime "V", where all liquid water is vaporized at the CL; only vapor is transported out of the CL.
- regime "V_g", where liquid water is transported out of the CL into the MPL and GDL, and vaporized completely in the GDL; there is no liquid flux out from the GDL to the flow fields. This corresponds to a case where the liquid water is not transported along the entire extent of the GDL.
- regime "M", where a mixture of liquid water and vapor flows out of the GDL and into the flow fields.

There are 9 possible regimes of transport, with V, V_g, or M on either the anode or cathode side. In labeling the transport regime, we state first the tranport regime at the anode, then the transport regime at the cathode, e.g. VMT means that only vapor (V) flows out of the aCL and mixed liquid/vapor (M) flow out of the cGDL; T stands for transport. Fig. 5.3 shows these regimes with possible paths for the transitions amongst

them as current density increases. As current density and liquid production in the cathode increases, each electrode goes from V to V_g and eventually to the M regime; current densities at these transitions are determined by the MEA component transport properties and operating conditions. In practice, we can neglect the case of liquid transport in the anode prior to the cathode (e.g. the V_gVT regime), unless a large differential in gas pressure across the MEA is applied ($\Delta p^G = p_c^G - p_a^G > 70$kPa with the base case parameters assumed in this work), or with unusually impermeable diffusion media at the cathode side. In Fig. 5.3, such paths are marked in grey while more likely paths are marked in red.

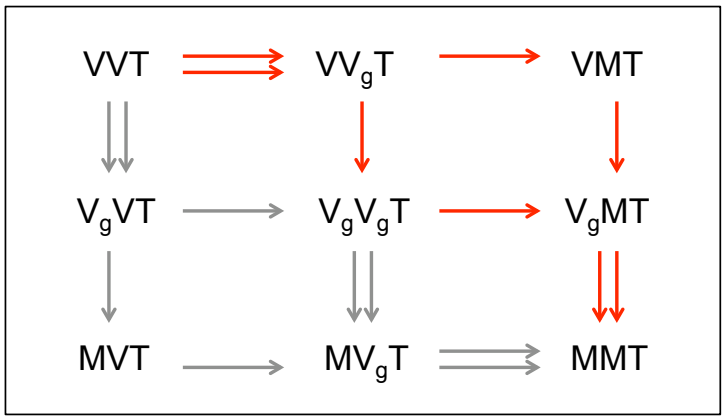

Figure 5.3: The 9 possible regimes of transport within the current model. Possible paths for transitions amongst the regimes, as current density increases, are shown in arrows. Likely paths are marked in red; less likely paths, corresponding to liquid transport in the anode relative to the cathode, are marked in grey.

We denote the current density at the onset of liquid flux out of the cCL and out of the cGDL at the cathode by $j_c^{V_g}$ and j_c^M, respectively. For the current densities referring to the transitions at the anode, the subscript is a. For example, for the path shown in red in Fig. 5.3, $j_c^{V_g} < j_c^M < j_a^{V_g} < j_a^M$. The onset of cGDL flooding, where $p^c = p^c_{GDL,fl}$ at the MPL|cGDL interface, is denoted by j^{fl}_{cGDL}. Fig. 5.4 shows a schematic of a polarization curve with these current densities marked out in black dashed lines. The

present model does not include analysis at $j_o > j_{cGDL}^{fl}$, viz. above the onset of flooding of the cGDL. Above this j_{cGDL}^{fl}, given the 4-5 orders of magnitude decrease of the O_2 diffusion coefficient in water relative to air, the increasing liquid water saturation in the GDL is expected to cause severe oxygen transport losses. In view of flooding mitigation, j_{cGDL}^{fl} is the key optimization parameter of the present model.

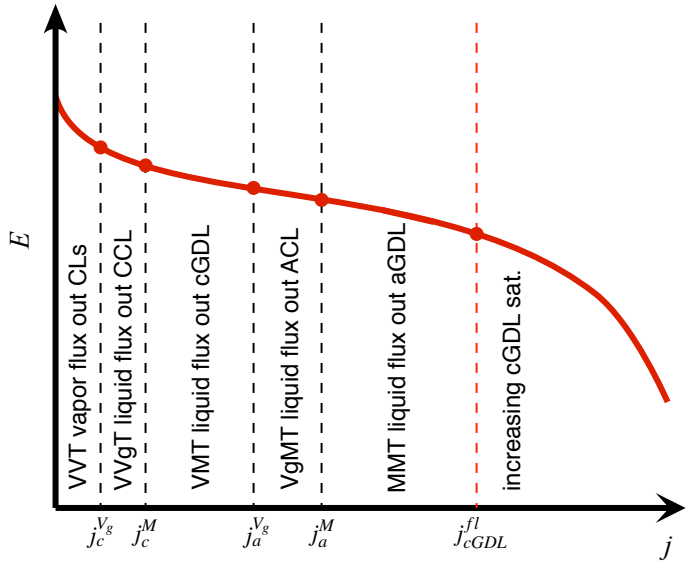

Figure 5.4: Schematic of a polarization curve with a typical sequence of transport regimes, transition and cGDL flooding current densities marked out. The model does not consider current densities above j_{cGDL}^{fl}, the onset of flooding at the cGDL|MPL interface.

5.1.3 Model Equations

In what follows, we show the equations of water balance in the aCL and cCL, and flux in the MEA components. Symbols, parameters, and their definitions are given in Table 3. Pressure gradients are the driving force for water flux. Vaporization rates, diffusivities, permeabilities, MEA component thicknesses, and water viscosity are lumped into

effective resistances to water flux. We impose flux and pressure continuity at component interfaces. For the diffusion media, we only show the flux equations for cathode components, indicated by a subscript c; the anode equations are identical (subscript a), with the additional condition that R^L_{MPL} and $R^V_{MPL} = 0$, since we do not include an MPL on the anode side.

Mass balance equations at cCL and aCL are

$$\text{at cCL}: \qquad J_o + J_{eo} = J_c + J^L_{PEM}, \tag{5.1}$$

$$\text{at aCL}: \qquad J_{eo} + J_a = J^L_{PEM} \tag{5.2}$$

where J_o is the flux produced with the oxygen reduction reaction (ORR), J_{eo} the electroosmotic flux across the PEM from anode to cathode, J^L_{PEM} the back permeation in the PEM, and J_c and J_a the total water fluxes out the cGDL and aGDL, respectively.

Mass fluxes of water produced in the cCL via ORR and arriving via electro-osmotic drag in the PEM are, respectively,

$$J_o = \frac{j_o M_w}{2F}\ ,\ J_{eo} = \frac{j_o n_{eo} M_w}{F}\ , \tag{5.3}$$

where j_o is the Faradaic ORR current density.

Liquid flux in the PEM is given by

$$J^L_{PEM} = -\frac{w}{R^L_{PEM}}\frac{dp^L}{dy_p},\ R^L_{PEM} = \frac{\mu_w L_{PEM}}{k^{sat}_{PEM}\rho_w} \tag{5.4}$$

where w is the water content of the PEM with range $0 \leq w \leq 1$, nomalized by the saturated water content, and y_p the variable of displacement along the PEM axis, normalized by the thickness of the PEM, L_{PEM}. We have assumed a linear dependence of permeability with w [175]. The relationship of w to equilibrium vapor pressure $p^{V,eq}$ and capillary pressure p^c are given by empirical fits to capillary and sorption isotherms

of Nafion 112 [182, 183],

$$w = \frac{3}{14}\left(\frac{p^{V,eq}}{p_{\infty}^{V,eq}}\right)^{0.2} + \frac{11}{14}\left(\frac{p^{V,eq}}{p_{\infty}^{V,eq}}\right)^{4} \tag{5.5}$$

$$w = 0.5(1+\tanh(-\log|p^c|+2.4)) \tag{5.6}$$

where $p_{\infty}^{V,eq}$ is the saturated vapor pressure, and $p^c = p^L - p^G$, given in bars. In Eq. 5.5, the fractions denote surface and bulk water fractions of a saturated membrane. These isotherms are shown in Fig. 5.5.

The saturated vapor pressure is given by the empirical Antoine equation

$$\log p_{\infty}^{V,eq} = a - \frac{b}{T+c} \tag{5.7}$$

where $a = 4.6543,\ b = 1435.624,\ c = 64.848$ for $p_{\infty}^{V,eq}$ in bars [8]. The variation in viscosity with temperature is given by [184]

$$\mu_w = A \times 10^{\frac{B}{T-C}},\ A = 2.41 \times 10^{-5}\text{Pa}\cdot\text{s},\ B = 247.8\text{K},\ C = 140\text{K}\,. \tag{5.8}$$

We treat liquid and vapor fluxes within the anode and cathode GDL with a transmission line model [174], illustrated in Fig. 5.6. To condense notation, we denote properties/fluxes within the cGDL by the subscript c, and those within the aGDL by the subscript a. We introduce here the flux equations within the cGDL; the anode ones are identical with the subscript c replaced by a. In the current three–state assumption of the GDL, liquid water penetrates the GDL progressively, and the length of the transmission line, L_{cTL}, is variable. The axis along the transmission line, y_c, is normalized by L_{cTL}. We introduce a dimensionless parameter $l_c = L_{cTL}/L_c$, where $0 \le l_c \le 1$. The vapor and

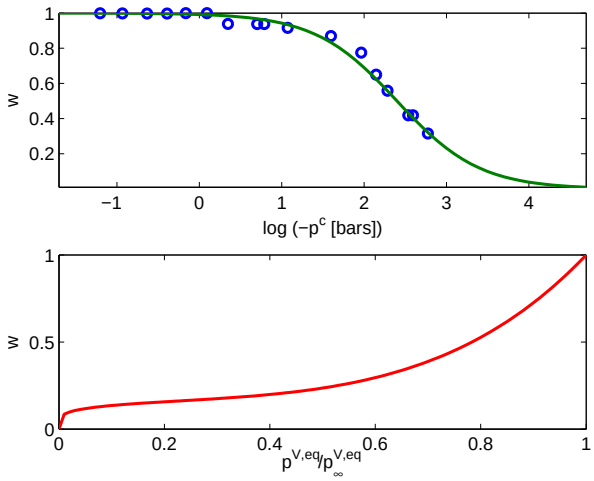

Figure 5.5: Empirical fits to capillary (top) and vapor sorption (bottom) isotherms of Nafion 112 [182, 183]

liquid fluxes in the cGDL are,

$$J_c^V = -\frac{1}{R_c^V l_c}\frac{dp_c^V}{dy_c}, \quad R_c^V = \frac{RTL_c}{D_c M_w}, \tag{5.9}$$

$$J_c^L = -\frac{1}{R_c^L l_c}\frac{dp^L}{dy_c}, \quad R_c^L = \frac{\mu_w L_c}{k_c \rho_w}. \tag{5.10}$$

Vaporization converts liquid to vapor flux, and is given by

$$\frac{dJ_c^V}{dy_c} = -\frac{dJ_c^L}{dy_c} = \frac{p_\infty^{V,eq} - p_c^V}{R_c^{LV}/l_c}, \quad R_c^V = \frac{1}{\kappa^{LV}\xi_c^{LV}}. \tag{5.11}$$

The total flux in the cGDL is $J_c = J_c^V + J_c^L$.

The boundary conditions for the transmission line GDL model are given by pressure and flux continuity, which depend on the transport regime. Given the large GDL pores (1–10μm) [179], we can assume $p_c^c(1) = 0$, i.e. $p_c^L(1) = p_c^G$. Where the transmission line does not extend to the GDL|flow field interface (the V_g regime), $0 < l_c < 1$, the

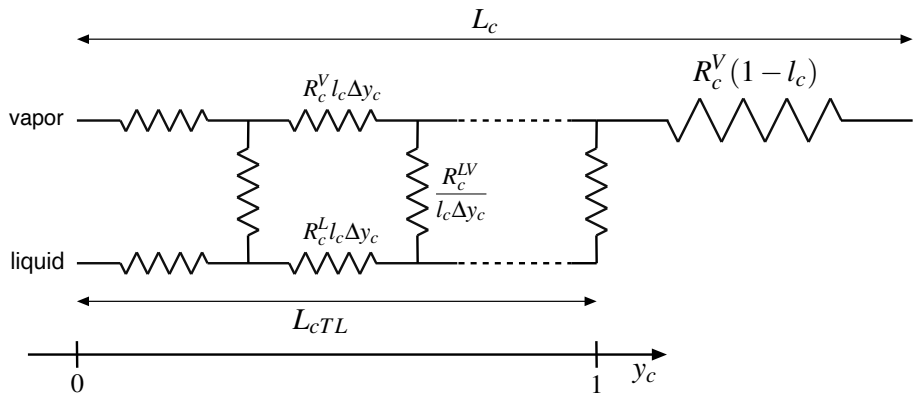

Figure 5.6: Transmission line model of the cGDL, showing the effective resistances to liquid and vapor fluxes and liquid|vapor conversion. The axis y_c is normalised to L_{cTL}, the extent of the transmission line and penetration of liquid water in the GDL. L_c is the width of the cGDL. Δy_c denotes an infinitesimal element along y_c.

vapor flux out of the GDL and into the flowfield is

$$J^V_{cFF} = \frac{p^V_c(1) - p^{V,eq}_\infty \mathrm{RH}_c}{R^V_c(1-l_c)}, \tag{5.12}$$

and liquid flux out is zero.

The vaporization rate at the cCL is [18]

$$J^{LV}_{cCL} = \frac{p^{V,eq}(w) - p^V_{cCL}}{R^{LV}_{CL}},\ R^{LV}_{CL} = \frac{1}{\kappa^{LV}\xi^{LV}_{cCL}}, \tag{5.13}$$

where $p^{V,eq}(w)$ is given implicitly by Eq. (5.5). In the anode, without an MPL, $p^V_{aCL} = p^V_a(0)$ and $p^L_{aCL} = p^L_a(0)$. Vapor diffusion and liquid permeation flux in the cathode MPL are

$$J^V_{MPL} = \frac{p^V_{cCL} - p^V_c(0)}{R^V_{MPL}} = \frac{p^{V,eq}(w) - p^V_c(0)}{R^V_{MPL} + R^{LV}_{CL}},\ R^V_{MPL} = \frac{RTL_{MPL}}{D_{MPL}M_w} \tag{5.14}$$

$$J^L_{MPL} = \frac{p^L_{cCL} - p^L_c(0)}{R^L_{MPL}},\ R^L_{MPL} = \frac{\mu_w L_{MPL}}{k_{MPL}\rho_w} \tag{5.15}$$

The 2nd equality of Eq. (5.14) is given by pressure and flux continuity at the cCL|MPL interface, $J^V_{MPL} = J^{LV}_{cCL}$ from Eq. (5.13).

5.2 Model Solution

In the following, we first discuss the solutions to the PEM and GDL models in terms of liquid and/or vapor pressures a their respective boundaries. When these solutions are combined with mass balance (Eqs. 5.1,5.2), and pressure and flux continuity at the MEA component boundaries, we obtain the relationships between j_o and capillary pressure (e.g. at the cCL and cGDL boundaries, p^c_{cCL} and $p^c(0)$), the anode and cathode fluxes, and current densities at CL and cGDL flooding.

5.2.1 Solution to PEM Model

We make the approximation of constant water content w within the PEM, since pressure differences of $\gtrsim 10$ bars are required for $\Delta w \sim 0.2$ (cf. Fig. 5.5); we check this assumption *a posteriori* with the computed pressure drop across the PEM. In this case, Eq. (5.4) reduces to

$$J^L_{PEM} = \frac{w}{R^L_{PEM}}\left(p^L_{cCL} - p^L_{aCL}\right) = \frac{w}{R^L_{PEM}}\left(p^c_{cCL} - p^c_{aCL} + \Delta p^G\right) \tag{5.16}$$

where $\Delta p^G = p^G_c - p^G_a$. Where there is liquid in either electrode, i.e. p^c_{aCL} and/or $p^c_{cCL} \geq p^c_{fl,CL}$, $w = 1$ throughout the PEM. Where water is transported out both the anode and cathode in vapor form (VVT regime), $w < 1$, and must be solved for via mass balance and Eqs. (5.5, 5.6).

5.2.2 Solution to the Transmission Line Model of the GDL

We first give the solution to Eqs. (5.9, 5.10, 5.11) in terms of p_c^V and p_c^L at the transmission line boundaries, $y_c = 0$ and 1. Eqs. (5.9, 5.11) give a 2nd order ODE for J_c^V;

$$\frac{d^2 J_c^V}{dy_c^2} - \frac{R_c^V}{R_{GDL}^{LV}} l_c^2 J_c^V = 0 \,. \tag{5.17}$$

As discussed below, estimates for R_c^V, R_c^{LV} indicate that $R_c^V << R_c^{LV}$. Where $R_c^V \lesssim R_c^{LV}$, we can linearize the solutions to Eq. (5.17). At $y_c = 0$ and 1,

$$J_c^V(0) = \frac{p_c^V(0) - p_c^V(1)}{l_c R_c^V} - \frac{l_c}{6R_{GDL}^{LV}} \left(3p_\infty^{V,eq} - p_c^V(1) - 2p_c^V(0)\right) \tag{5.18}$$

$$J_c^V(1) = \frac{p_c^V(0) - p_c^V(1)}{l_c R_c^V} + \frac{l_c}{6R_{GDL}^{LV}} \left(3p_\infty^{V,eq} - p_c^V(1) - 2p_c^V(0)\right) \,. \tag{5.19}$$

From mass conservation, the total water flux in the cGDL, J_c, is fixed. Substituting $J_c^L = J_c - J_c^V$ into Eq. (5.10) and integrating from $y_c = 0$ to 1, we obtain

$$J_c^L(0) = \frac{p_c^L(0) - p_c^G}{l_c R_c^L} + \frac{l_c}{6R_{GDL}^{LV}} \left(3p_\infty^{V,eq} - p_c^V(1) - 2p_c^V(0)\right) \tag{5.20}$$

$$J_c^L(1) = \frac{p_c^L(0) - p_c^G}{l_c R_c^L} - \frac{l_c}{6R_{GDL}^{LV}} \left(3p_\infty^{V,eq} - p_c^V(1) - 2p_c^V(0)\right) \,. \tag{5.21}$$

We now show J_c and relevant capillary pressures in the 3 regimes, V, V$_g$, and M.

Solution in the V regime

The V regime corresponds to the trivial case of $l_c = 0$, vapor transport only in the GDL, and the transmission line model is not required. Continuity of pressures and fluxes at the cCL|MPL and MPL|cGDL boundaries gives the total flux

$$J_c = \frac{p^{V,eq}(w) - p_\infty^{V,eq} \cdot \mathrm{RH}_c}{R_{CL}^{LV} + R_{MPL}^V + R_{cGDL}^V} \,. \tag{5.22}$$

In the anode case, $R^V_{MPL} = 0$. Where there is liquid in either the anode or cathode GDL, $w = 1$ and $p^{V,eq}(w) = p^{V,eq}_\infty$. In the VVT regime, w is determined from the mass balance equations and Eqs. (5.5, 5.6).

Solution in the V_g regime

In the V_g regime, where $0 < l_c < 1$, continuity of fluxes and pressures gives:

$$\begin{aligned} J^V_c(0) &= J^V_{MPL} && \text{(Eqs. 5.18 and 5.14)} \\ J^V_c(1) &= J^V_{cFF} && \text{(Eqs.5.19 and 5.12)} \\ J^L_c(0) &= J^L_{MPL} && \text{(Eqs. 5.20 and 5.15)} \\ J^L_c(1) &= 0 && \text{(Eq. 5.21) .} \end{aligned}$$

This provides 4 equations for the 4 unknowns, $p^L_{cCL}, p^L_c(0), p^V_c(0), p^V_c(1)$, which give

$$J_c = J^V_c(1) = A_1 p^{V,eq}_\infty (1 - \mathrm{RH}_c) \,, \tag{5.23}$$

$$p^c_{cCL} = (A_2 + A_3) p^{V,eq}_\infty (1 - \mathrm{RH}_c) = p^c_c(0) + A_3 p^{V,eq}_\infty (1 - \mathrm{RH}_c), \tag{5.24}$$

where the factors A_1, A_2, A_3 depend on l_c and transport resistances. These factors are given in Appendix D. In the anode case, where no MPL is considered, $p^c_{aCL} = p^c_a(0)$ and the corresponding $A_3 = 0$. The mass balance equations provide an implicit function of l_c, which can be solved for via, e.g. Newton type methods.

Solution in the M regime

In the M regime, l_c = 1 and $p^V_c(1) = p^{V,eq}_\infty \mathrm{RH}_c$. Applying continuity of fluxes and pressures, i.e. the 1st and 3rd conditions given above for the V_g regime above, we have 2 equations for 2 unknowns $p^V_c(0)$, and $p^c_c(0)$. We can then write the total, vapor, and

liquid fluxes out the GDL,

$$J_c = J_c^V + J_c^L = \frac{p_{cCL}^c}{R_c^L + R_{MPL}^L} + B_1 p_\infty^{V,eq}(1 - \mathrm{RH}_c), \tag{5.25}$$

$$J_c^V(1) = B_2 p_\infty^{V,eq}(1 - \mathrm{RH}_c)\ , \tag{5.26}$$

$$J_c^L(1) = \frac{p_{cCL}^c}{R_c^L + R_{MPL}^L} + (B_1 - B_2) p_\infty^{V,eq}(1 - \mathrm{RH}_c) \tag{5.27}$$

and p_{cCL}^c is related to $p_c^c(0)$ via

$$p_{cCL}^c = \frac{R_c^L + R_{MPL}^L}{R_c^L} p_c^c(0) + B_3 p_\infty^{V,eq}(1 - \mathrm{RH}_c)\ . \tag{5.28}$$

The factors B_1, B_2 and B_3, given in Appendix D, depend on the transport resistances. Again, in the anode case, $R_{MPL}^L = R_{MPL}^V = 0$ and the corresponding $B_3 = 0$.

5.2.3 Solution of the mass balance equations

At any of the 9 water transport regimes (cf. Fig. 5.3), relations among j_o, relevant p^c, and water fractions are obtained by combining the solutions to the PEM and GDL transmission line models with mass balance equations (Eqs. 5.1,5.2). Given either j_o or the capillary pressure at a point within the MEA, e.g. $p_{cCL}^c, p_c^c(0)$, or p_{aCL}^c, the corresponding transport regime is not known *a priori*. It can, in principle, be determined via trial and error with the transmission line solutions in various regimes until a consistent scenario is found, i.e. the determined capillary pressures are consistent with the transport regime assumed. An additional challenge is that mass balance involving V_g on either side give implicit functions of l_c, p_{cCL}^c, and/or j_o. These cases rely on Newton solution methods for the mass balance equations that require good initial guesses to obtain the physical solution. We therefore consider V_g regimes last, and only when M and V cases do not give consistent solutions. This solution procedure is detailed in Appendix E.

5.3 Results and Discussion

In what follows, we perform a parameter study of the effective transport resistances, RH, and gas pressures. We evaluate the impact of these parameters on the pressure distribution in the MEA, transition and flooding current densities, and anode and cathode water and liquid fractions.

5.3.1 Base Case Parameters

Base case transport coefficients, operating conditions and effective transport resistances are listed in Table 3. We obtained transport coefficients from various literature sources for the base case, as there is no comprehensive published data on the transport properties of the components of MEAs with ultrathin catalyst layer. The focus of this work is qualitative results and trends, not the reproduction of exact results within any particular UTCL MEA.

A particular source of uncertainty is the dependence of the permeability of diffusion media on saturation. Recent work from Hussaini and Wang suggest the relative permeability of carbon paper to show an empirical $s^{5.5}$ dependence, where s is the saturation, and carbon cloth to follow $0.01s^3$, while the saturated permeability of both materials was $\sim 2\times10^{-11}$ m^2. Since we assume the GDL to have continuous liquid water paths within the extent of the transmission line, they must then have a saturation corresponding to at least that at the breakthrough pressure Refs. [16] and [185] found $s\sim 1-10\%$ at breakthrough; assuming $s=5\%$, either of Hussaini's relations give a total permeability of $k_{GDL}\sim 1\times10^{-17}$ m^2. For the MPL permeability k_{MPL}, we assume the fitted value from the water balance model of Ref. [15].

Assuming a monodisperse pore size distribution in the CL, it should either be completely unsaturated or fully flooded, so the CL liquid|vapor interfacial area, ξ_{CL}^{LV}, should always be about 1. We therefore assume a base case value of $\xi_{CL}^{LV}=1$. Dispersion

in pore sizes would result in partial saturation at certain current densities and an increase of ξ_{CL}^{LV}. To obtain a rough, base case estimate of ξ_{GDL}^{LV}, we assume that the water is transported through MPL cracks and that the GDL saturates first in proximity of these cracked regions [16]. From the estimated area density of MPL cracks, $n_{crack} = 810\text{cm}^{-2}$, and crack perimeters, $p_{crack} = 0.42\text{cm}$, of Ref. [186], we estimate $\xi_{GDL}^{LV} \sim n_{crack} p_{crack} L_{GDL} \sim 1$. We consider the impact of varying ξ_{CL}^{LV} and ξ_{GDL}^{LV} on the onset of CL and GDL flooding.

The capillary pressure at CL flooding, $p_{fl,CL}^{c}$, is estimated from the CL pore radius r via the Young–Laplace equation

$$p^c = -\frac{2\gamma\cos\theta}{r}\,, \tag{5.29}$$

where γ is the surface tension of water and the contact angle $\theta = 0$ due to hydrophilicity of Pt. For the base case, we assume r = 50nm, which is around the size of the NSTF whiskers. The capillary pressure at the onset of GDL flooding, $p_{fl,GDL}^{c}$ is estimated from the capillary pressure isotherms of Ref. [16].

5.3.2 Ultrathin Catalyst Layer Flooding

The degree of the liquid water saturation in the UTCL is a source of controversy [67]. For the base case, the assumed r =50nm corresponds to a $p_{CL,fl}^{c} = -25$ bar via Eq. (5.29). Fig. 5.7 shows the variation of the cCL flooding current density, j_{cCL}^{fl}, with temperature for the base case, as well as for various r, RH, and R_{CL}^{LV} (we assumed RH_a = RH_c = RH). A comparison of the base and $r = 5$nm ($p_{CL,fl}^{c} = -250$ bar) cases shows only a slight sensitivity of j_{cCL}^{fl} to r; this arises from the large capillary pressure variations required to vary the saturation, cf. Fig. 5.5. A comparison of j_{cCL}^{fl} corresponding to low (0%) and high (95%) RH shows the expected trend of higher j_{cCL}^{fl} for lower RH, which corresponds to higher vaporization rates at the CLs.

We have considered variation of R_{CL}^{LV} by factors of 0.2 and 5, since we expect about an order of magnitude uncertainty in R_{CL}^{LV}; Refs. [18] and [187] provide vaporization rates, κ^{LV}, that differ by about an order of magnitude, and ξ_{CL}^{LV} could increase with dispersion in pore sizes. j_{cCL}^{fl} from R_{CL}^{LV} varied by factors of 0.2 and 5 are significantly different at high $T >$320K. At $0.2 \times R_{CL}^{LV}$, j_{cCL}^{fl} approaches 1A/cm^2 at high $T > 350K$; in this case, the catalyst layer may not be fully flooded at certain operating j_o and T. Since protons require water for conduction, an unsaturated CL would lead to increased proton transport losses, as suggested by the polarization data of Ref. [67]. Operation at high RH may be required to keep CL pores flooded, to minimize proton transport losses.

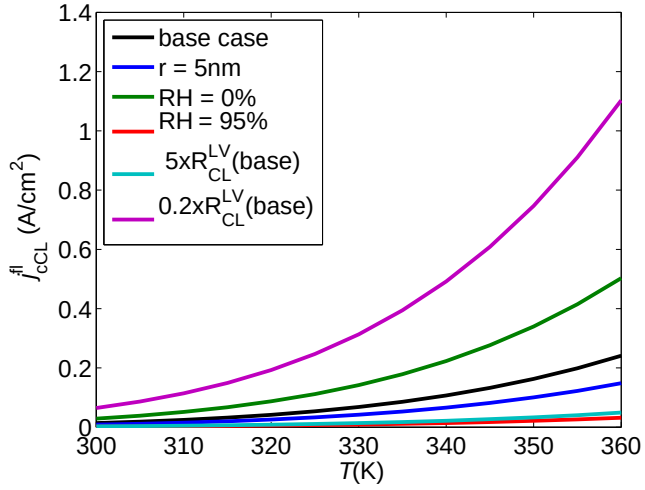

Figure 5.7: The variation of j_{cCL}^{fl} with temperature for the base case with $r = 50$nm, RH$= 50\%$ (at anode and cathode), as well as for various pore radii r, RH, and vaporization resistances R_{CL}^{LV}.

5.3.3 Water and Liquid Fractions and Transition Current Densities

The fraction of water produced in the ORR transported across the PEM from cathode to anode is the anode water fraction,

$$\text{AWF} = \frac{J_a}{J_o} \,. \tag{5.30}$$

Where the cathode is in the "M" regime, the fraction of water transported out the cathode flow fields in liquid form is the cathode liquid fraction,

$$\text{CLF} = \frac{J_c^L(1)}{J_c} \,. \tag{5.31}$$

Where the anode is in the "M" regime, the anode liquid fraction is

$$\text{ALF} = \frac{J_a^L(1)}{J_a} \,. \tag{5.32}$$

Fig. 5.8 shows the AWF, CLF, and ALF vs. j_o for base case transport parameters and T=323K, RH = 50%. The various regimes of transport are also marked. The AWF curve shows that a substantial fraction of water produced in the cathode is evacuated out the anode; CLF and ALF curves show that the water is evacuated out both electrodes in liquid form, except at $j_o < 0.25\text{A/cm}^2$. Given that we have assumed R_{GDL}^{LV} to be similar in magnitude as R_{CL}^{LV}, the intermediate V_g regimes occur at a small range of j_o, i.e. liquid flux out the flow fields occurs at current densities slightly above the onset of liquid flux into the GDL.

The cusps in AWF arise from transitions between regimes at the anode side. In the VVT case, with the assumption of constant w, the AWF is

$$\text{AWF} = \frac{J_o(R_{CL}^{LV} + R_{MPL}^{V} + R_{cGDL}^{V}) + p_{\infty}^{V,eq}(\text{RH}_c - \text{RH}_a)}{J_o\left(2R_{CL}^{LV} + R_{aGDL}^{V} + R_{MPL}^{V} + R_{cGDL}^{V}\right)}. \tag{5.33}$$

At the base case parameters assumed, AWF $\approx 1/2$, as shown. In the VV$_g$T and VMT regimes, the AWF is

$$\text{AWF} = \frac{J_{aCL}^{LV}}{J_o} \tag{5.34}$$

and J_{aCL}^{LV} is given by Eq. (5.13) with $w = 1$, and is fixed as J_o varies. In the V$_g$MT and MMT regimes, where liquid is also present in the anode GDL, the AWF is determined by the liquid pressure distributions that vary with j_o.

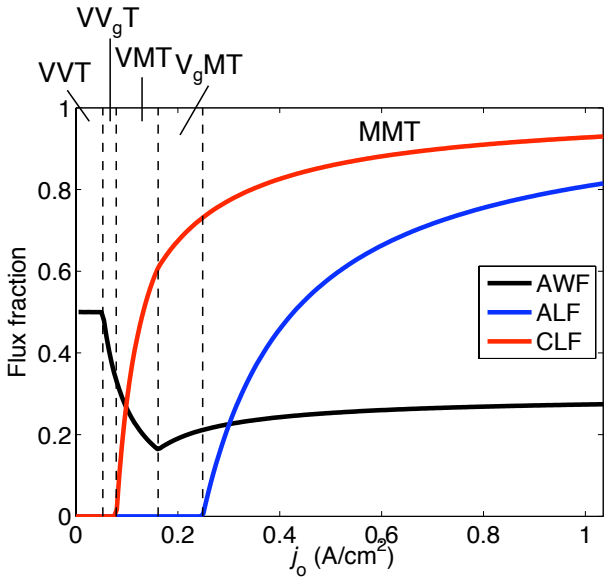

Figure 5.8: Water and liquid fractions CWF, CLF, and ALF vs. the j_o for base case transport parameters (Table 3) and T=323K, RH$_a$ = RH$_c$ = 50%.

Fig. 5.9 shows the base case transition current densities, $j_c^{V_g}, j_c^M, j_a^{V_g}, j_a^M$, and the cGDL flooding current density j_{cGDL}^{fl} as a function of T. At $T < 330$K, we would expect liquid transport out both the anode and cathode (MMT regime) for all $j_o > 0.2$A/cm^2. The reduced flooding current density at lower T arises from primarily the decrease in $p_\infty^{V,eq}$, which decreases vaporization rates, and also the decrease in μ_w, which increases the permeation resistances. This dramatic reduction in j_{cGDL}^{fl} with temperature is in

line with increased issues with flooding observed in UTCL MEAs at low and moderate temperatures [69, 70].

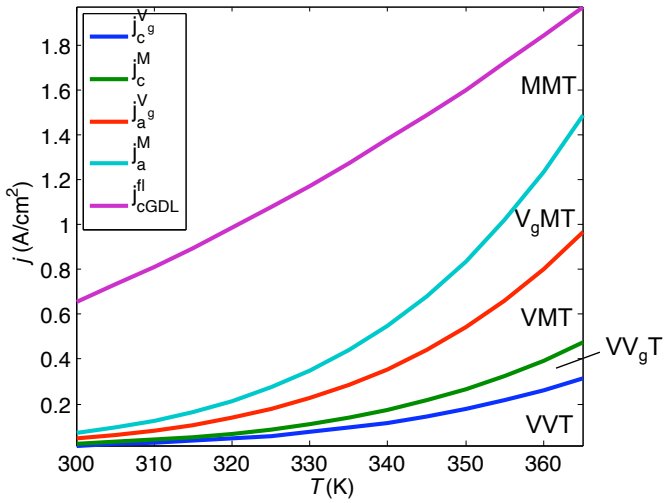

Figure 5.9: Transition current densities, $j_c^{V_g}, j_c^M, j_a^{V_g}, j_a^M$, and cathode GDL flooding current density j_c^{fl} as a function of T; the various regimes of transport are also marked. Assumed base case transport parameters of Table 3.

5.3.4 Effect of transport resistances, operating conditions on onset of flooding at the GDL

Fig. 5.10 shows j_{cGDL}^{fl} vs. $R/R(\text{base})$ for $R = R_{CL}^{LV}$ and R_{GDL}^{LV} (on both the cathode and anode sides). In both cases, there is a dramatic increase in j_{cGDL}^{fl} as the $R/R(\text{base})$ decreases (i.e. vaporization rates increase). This effect has been explored in 3M NSTF MEAs by Kongkanand *et al.* [69], who found hybrid NSTF – low-loaded conventional CL structures to dramatically improve steady state and transient performance at low temperatures. This improvement may arise from the increased vaporization area around the CL region (increased ξ_{CL}^{LV}). Modeling studies suggest that conventional CLs, comprised of 3–phase composites of Pt nanoparticles, carbon black, and ionomer, have a

large liquid|vapor interfacial area due to their partially saturated bimodal porous structure [18, 180]. Additional increases in ξ_{GDL}^{LV} via, e.g., engineering GDLs with a hydrophilic/hydrophobic bimodal porous structure, may also lead to further increases in performance.

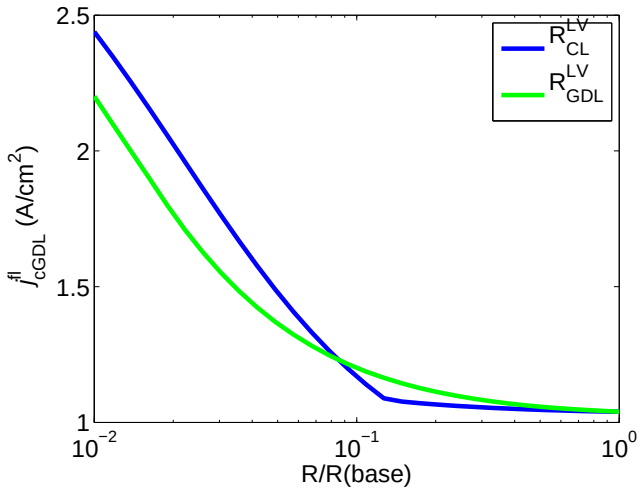

Figure 5.10: j_{cGDL}^{fl} vs. R/R(base) for R_{CL}^{LV} and R_{GDL}^{LV} (on both cathode and anode)

Given that liquid water transport predominates over relevant ranges of j_o, liquid transport resistances have a dramatic impact on j_{cGDL}^{fl}. Fig. 5.11 shows the variation in j_{cGDL}^{fl} as R_{PEM}^{L}, R_{cMPL}^{L}, and R_{cGDL}^{L} are varied. We note that in certain cases the anode can also begin to flood. However, given the 6 orders of magnitude difference between HOR and ORR exchange current densities [27, 28], we expect H_2 diffusion limitations in the aGDL to pose negligible overpotential losses compared to those from O_2 diffusion limitations. Therefore, anode flooding should not have a significant impact on performance, and we do not investigate it further with the model.

Since R_{PEM}^{L} and R_{MPL}^{L}, are order(s) of magnitude higher than R_{cGDL}^{L} and R_{aGDL}^{L}, they determine the liquid flux distribution. By either decreasing R_{PEM}^{L} or increasing R_{MPL}^{L}, the water fraction to the anode is increased and j_{cGDL}^{fl} increases. R_{cGDL}^{L} has little effect

on the overall liquid flux distribution, but decreasing R^L_{cGDL} does decrease j^{fl}_{cGDL}, since lower p^c differences across the GDL are required for a given amount of liquid flux.

These results suggest two methods for mitigating cathode GDL flooding via MEA component liquid permeabilities: maximizing the R^L_{MPL}/R^L_{PEM} ratio to steer more liquid to the anode side, or decreasing R^L_{cGDL} to facilitate water removal via the cathode. In recent years, PEM thicknesses have already been reduced by an order of magnitude, so an increase in R^L_{MPL}/R^L_{PEM} should likely arise from an increase in R^L_{MPL}, i.e. through reducing the hydrophilic cracks that form in MPLs during MEA fabrication [16,178,186]. Decreasing R^L_{cGDL} without conceding substantial decreases in O_2 diffusivity and $p^c_{fl,GDL}$ may be possible via introducing ordered, hydrophililic laser-perforations in GDLs [188].

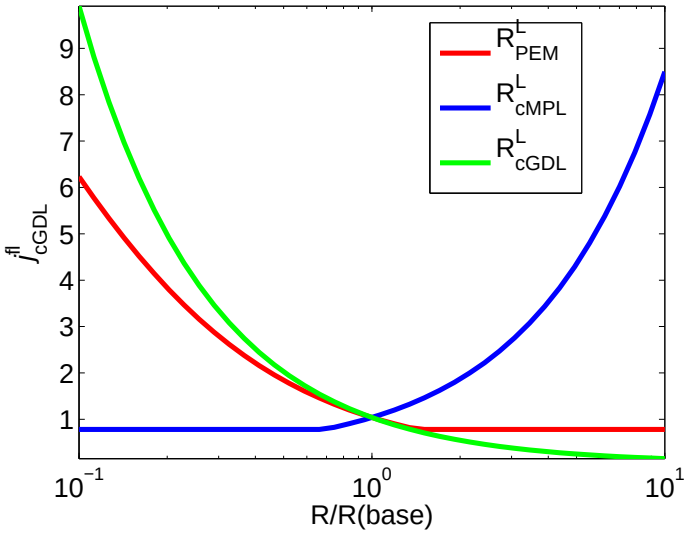

Figure 5.11: j^{fl}_{cGDL} (solid lines), j^{fl}_{cGDL} (dotted lines) vs R/R(base) for R^L_{PEM}, R^L_{MPL}, R^L_{cGDL}, and R^L_{aGDL} are varied.

The distribution of liquid fluxes is affected by the gas pressure differential $\Delta p^G = p^G_c - p^G_a$. Fig. 5.12 shows j^{fl}_{cGDL} as a function of Δp^G. As the cathode pressure increases relative to the anode one, anode water fractions increase and j^{fl}_{cGDL} increases.

The change in slope at $\Delta p^G = -75$kPa corresponds to a VMT to V$_g$MT transition; in the VMT regime, anode water flux is solely in vapor phase and the gas pressure no longer has an effect on the water flux distribution. The increase in j^{fl}_{cGDL} with a positive Δp^G is consistent with preliminary experimental results from 3M [71], where improvements in steady state performance were observed with sub-atmospheric anode pressures.

5.3.5 Anode Water Fractions

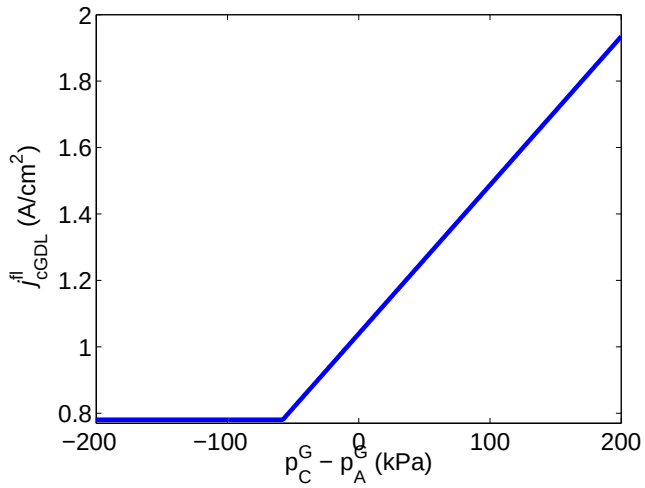

Figure 5.12: j^{fl}_{iGDL} as a function of Δp^G at RH$_a$ = RH$_c$ = 50%, $T = 323$K, and base case transport parameters

Water flux measurements can help identify the water transport regimes. For any given MEA, AWF can be varied as a function of j_o, Δp^G, and RH. Variation of AWF with j_o was discussed in Sec. 5.3.3; changes in slope and curvature indicate changes in the water transport regime. In this section, we focus on the variation of AWF with Δp^G and RH. Fig. 5.13 shows the AWF vs. Δp^G for j_o = 0.2, 0.5, and 0.8A/cm^2 at RH = 50%, $T = 323$K, and base case transport parameters. As Δp^G increases, the transport regimes shift in the sequence VMT $\rightarrow$ V$_g$MT $\rightarrow$ MMT $\rightarrow$ MV$_g$T $\rightarrow$ MVT. The four

transition points for each j_o are marked with dotted lines in the same color as the AWF curve. Where there is liquid phase in both the anode and cathode GDLs (V_g or M on either side), $\Delta p^G = p_c^L(1) - p_a^L(1)$, i.e. the gas pressure difference determines the liquid pressure difference at the ends of cathode and anode transmission lines, and thus has a direct influence on the water flux distributions. In either the VMT or MVT regimes, the water flux distribution is determined by the vaporization rate on one side of the PEM, which is unaffected by Δp^G.

In the MMT regime, where liquid flux is present on both sides, the slope of AWF vs. Δp^G is

$$\text{slope} = \frac{1}{J_o \times (R^L_{PEM} + R^L_{aGDL} + R^L_{cGDL} + R^L_{MPL})} , \tag{5.35}$$

i.e. it is inversely proportional to the total liquid transport resistance of all MEA components. With V_g on either side, there is no explicit expression for the slope of AWF vs Δp^G. However, as Fig. 5.13 shows, Δp^G does exert an influence on AWF as long as there is liquid water within the GDL. Preliminary 3M water flux measurements at j_o = 1A/cm^2, T = 20–50C, and $\Delta p^G = 0$ to 150kPa suggest a linear dependence of AWF on Δp^G, and hence the presence of liquid water in the GDLs on both electrodes [71].

In principle, changes in the slopes of AWF vs. RH may also help identify the water transport regime. The present model assumes constant RH along the flow channels, corresponding to differential cell conditions; variations in RH along the channel would lead to a smoothing out of slope transitions, which then become difficult to detect from experimental data. However, for completeness, we show the effect of RH on AWF below. Fig. 5.14 shows AWF vs. RH_a and RH_c for j_o = 0.2, 0.5, and 1.0A/cm^2. In the $j_o = 0.2$A/cm^2 case, the transport regime changes from VMT $\rightarrow$ V_gMT $\rightarrow$ MMT as RH_a and RH_c increase, and the transitions are marked with red dashed lines. For the other j_o, the transport regime is MMT under all RH considered. In the VMT case, the

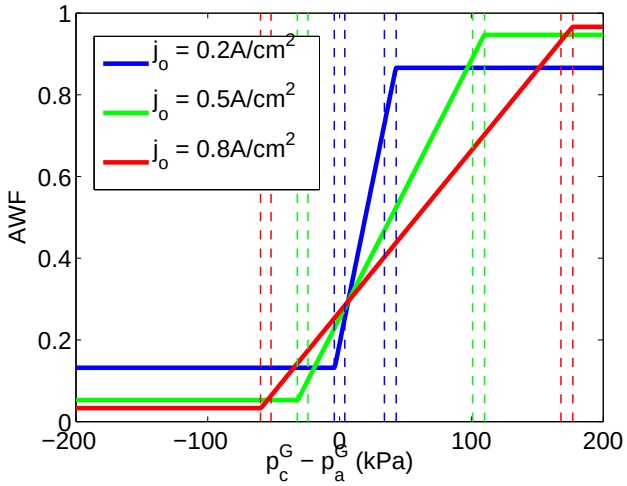

Figure 5.13: AWF vs. $\Delta p^G = p_C^G - p_A^G$ for j^o = 0.2, 0.5, and 0.8A/cm^2 at RH$_i$ = 50%, T = 323K, and base case transport parameters. As Δp^G increases, the transport regimes shift in the sequence VMT $\rightarrow$ V$_g$MT $\rightarrow$ MMT $\rightarrow$ MV$_g$T $\rightarrow$ MVT. The four transition points for each j^o are marked with dotted lines in the same color as the AWF curve.

AWF is fixed by the vaporization rate at the anode, i.e.,

$$\text{AWF} = \frac{p_\infty^{V,eq}(1-\text{RH}_a)}{J_o(R_{CL}^{LV} + R_{aGDL}^{V})}, \tag{5.36}$$

and hence shows no dependence on RH$_c$, and a linear dependence on RH$_a$. With V$_g$ regimes, there are no explicit expressions for the slope.

In the MMT case, under the assumption $R_{GDL}^{LV} >> R_{aGDL}^{V}$, R_{cGDL}^{V} (valid in the base case), the slope with respect to RH$_a$ is

$$\text{slope} = -\frac{p_\infty^{V,eq} R_{aGDL}^{L}}{J_o(R_{CL}^{LV} + R_{aGDL}^{V})(R_{PEM}^{L} + R_{aGDL}^{L} + R_{MPL}^{L} + R_{cGDL}^{L})}. \tag{5.37}$$

Comparing Eqs. (5.36) and (5.37), we see that a sequence of VMT $\rightarrow$ V$_g$MT $\rightarrow$ MMT transitions results in a decreased slope of AWF vs. RH$_a$, as shown in Fig. 5.14(a) for j_o = 0.2A/cm^2.

The slope with respect to RH_c in the MMT regime, where $R^{LV}_{GDL} >> R^{V}_{aGDL}$, R^{V}_{cGDL}, is

$$\text{slope} = \frac{p^{V,eq}_{\infty}(R^{L}_{MPL} + R^{L}_{cGDL})}{J_o(R^{LV}_{CL} + R^{V}_{MPL} + R^{V}_{cGDL})(R^{L}_{PEM} + R^{L}_{aGDL} + R^{L}_{MPL} + R^{L}_{cGDL})}. \tag{5.38}$$

Therefore, a sequence of VMT $\rightarrow$ V_gMT $\rightarrow$ MMT transitions as RH_c is increased results in an increase in slope of AWF vs. RH_c from 0, as shown in Fig. 5.14(b) for j_o = 0.2A/cm^2.

In the MVT case, not shown in Fig. 5.14, the AWF is determined by the vaporization rate out of the cathode,

$$\text{AWF} = 1 - \frac{p^{V,eq}_{\infty}(1 - \mathrm{RH}_c)}{J_o(R^{LV}_{CL} + R^{V}_{MPL} + R^{V}_{cGDL})}, \tag{5.39}$$

and shows no RH_a dependence. Finally, AWF in the VVT regime, which occurs at the smallest current densities, is given by Eq. (5.33).

In principle, the predicted trends in AWF vs. j_o, Δp^G, and RH can be verified experimentally, in view of model evaluation. In practice, a variation of j_o, Δp^G, or RH along the channels may blur the transitions predicted by this work; inclusion of a flow-field model would be required to investigate the impact of these variations. We also note that the slopes predicted for AWF vs. RH using the current set of base case parameters are rather small, and changes in them may be difficult to detect experimentally; however, the magnitude of such slopes are, as shown in the equations above, dependent on the magnitudes of MEA component transport resistances, which can vary widely. In the case of Δp^G it is expected that AWF levels off at high and low enough Δp^G, corresponding to MVT and VMT regimes, respectively; this should occur regardless of any variation along the flow channels.

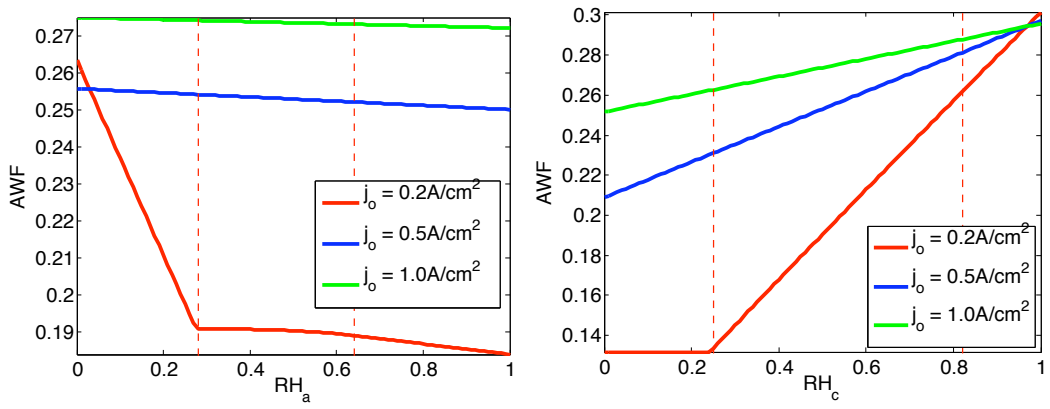

Figure 5.14: AWF vs. RH_a (left, at RH_c = 50%) and RH_c (right, at RH_c = 50%) for j_o = 0.2, 0.5, and 1.0A/cm^2. In the j_o = 0.2A/cm^2 case, the transport regime shifts from VMT to V$_g$MT to MMT, as RH_a or RH_c increases. The transition points between these regimes are marked with dotted red lines.

5.4 Conclusions

In this chapter, we presented a water balance model of the UTCL MEA, where the PEM was considered via a hydraulic permeation model [45] and the GDL via a transmission line model of water flux [174]. The model provides relationships between current density and pressure distributions, current densities at transitions between liquid and vapor transport regimes, and current densities at the onset of CL and GDL flooding. We have analysed the model in the relevant case of high vaporization resistances, where liquid water transport dominates in the MEA at moderate RH and T.

Model results suggest that UTCL MEAs could require high RH at high $T \sim 80$C to retain flooded CLs for proton conduction, but also efficient liquid transport paths out of the MEA at low to moderate T. This is in contrast to previous models of UTCL MEAs, where poor steady state and transient performance was attributed to the flooding of the UTCL, and GDLs were considered to be free of liquid water [67, 68]. The current density at onset of cathode GDL flooding can be increased by:

- increasing the ratio of MPL to PEM permeation resistances to steer liquid flux to the anode side, or by a cGDL of increased liquid permeability but fixed flooding capillary pressure (e.g. introduction of hydrophilic channels via laser perforation).
- a gas pressure differential, which steers liquid flux to the anode side.
- increasing vaporization areas via hybrid NSTF/conventional catalyst layers, or by developing increasing the vaporization rates within diffusion media via a specifically designed pore space morphology and wettability.

Preliminary experiments on 3M NSTF MEAs are consistent with several of these recommendations; increased steady state performance has been observed in hybrid NSTF/conventional catalyst layer electrodes [69], in MEAs of reduced PEM thickness, and where gas pressure differentials between cathode and anode have been applied [71]. Finally, water flux measurements can identify water transport regimes. The model predicts transitions among transport regimes as the j_o, RH or gas pressure differential are varied, which are reflected in slope changes of the anode water fraction. In particular, where liquid is present on both GDLs, the anode water fraction is expected to show a linear dependence on the gas pressure differential, and no dependence on gas pressure when water transports out of either catalyst layer in vapor form. The former dependence has been suggested in preliminary 3M NSTF water flux measurements [71], which further suggests the dominance of liquid transport in the diffusion media of 3M NSTF MEAs.

Chapter 6

Conclusions and Outlook

Ultrathin catalyst layers (UTCLs) have emerged as a genuine alternative to conventional catalyst layers in polymer electrolyte fuel cells, due to their high intrinsic activity and, in the case of 3M nanostructured thin films (NSTF), their dramatically improved resistance to degradation. In this thesis, we presented a single pore model of the UTCL, a novel generalisation of the computational hydrogen electrode, and a water balance model of MEAs of UTCLs. These models seek to address the open questions of proton transport in the ionomer–free UTCLs and the water management challenges in MEAs of UTCLs.

The main assumption of the single pore model of the UTCL is that protons undergo bulk transport, with the proton concentration determined by the interaction of the protons with the metal surface charge. The model explicitly considers the metal|solution interface via a Stern double layer model, applied to the boundaries of a single pore. The steady state variant of the model suggests the importance of metal|solution charging phenomena, which is mostly determined by the potential of zero charge of the metal phase. The implication for UTCL design is that materials should be chosen by their charging properties in addition to their intrinsic catalytic activity. The impedance variant of the model allows for the separation of electrostatic and kinetic contributions to UTCL performance.

The mechanism of proton transport at low relative humidities, where UTCL performance decreases, remains an open question [67]. Assuming capillary equilibrium, a poorer proton conductivity would correspond to a partial saturation of the UTCLs and a decreased capillary radius. Several authors have also speculated that protons transport in thin surface water films at low RH [64, 67]. Given that UTCLs contain no bulk electrolyte, any surface proton transport model must still include considerations of the metal surface charge.

The complex dependence of the surface charge density of Pt on potential and oxide coverage (which depends on both potential and pH) is not trivial to address from an *ab initio* point of view. Up until now, there has been no method to address the impact of pH on interface structure and charge. The novel generalised computational hydrogen electrode is a scheme to determine of the ground state metal|solution interfacial structure as a function of potential and pH. We applied the scheme to Pt(111)|water structures as an example. In further work, the scheme can be applied to determine the surface charge of Pt as a function of potential and pH, required to refine the current UTCL model to account for the complex charging behaviour of Pt and Pt oxides. However, with a fully *ab initio* approach, very large unit cells are required to obtain realistic surface charge densities. Implementation of hybrid continuum/*ab initio* methods may be required. We note that this method is applicable to any metal|solution interface, and should be applied in *ab initio* studies of any electrochemical system where the structure of water, fields, and/or surface charge is required.

The water balance model suggests that, due to the poor vaporization capacity of UTCLs, UTCL MEAs require efficient liquid water paths at moderate and low temperatures. This is in contrast to previous models of UTCL MEAs, where poor steady state and transient performance was attributed to the flooding of the UTCL, and GDLs were assumed to be free of liquid water [67, 68]; these conclusions rested on the unrealistic

assumption of a zero oxygen diffusion coefficient in flooded pores. The main determinants of current density at onset of GDL flooding are MEA component vaporization capacities and liquid permeabilities and the difference in gas pressure between the anode and cathode. The model predicts that water flux measurements can identify the regime of water transport.

While there are many possibilities to further the current work theoretically, we emphasise that a critical next step is to obtain experimental input in order to evaluate the major assumptions made in the current models. Our experimental collaborators have begun preliminary impedance measurements on 3M NSTFs; the current challenge is that high frequency inductances obscure the crucial solution resistance, which would allow for the detemination of proton conductivity. We expect thicker model systems (e.g. Pt Black catalyst layers), which have lower critical frequencies, to overcome these difficulties with the thin 3M NSTFs. Inert nanoporous systems (e.g. Au) are expected to show simpler charging behaviour, which could allow for the evaluation of the simple Stern model.

Previous work from GM in the flooding mitigation of NSTF MEAs have focussed on modifications to the catalyst layer [67–69]; this could be due to the erroneous assumption that oxygen cannot diffuse through water-flooded catalyst layers, and that therefore catalyst layer flooding leads to dramatic performance losses. Our water balance model emphasizes the impact of diffusion media transport and vaporization properties and gas pressure differentials on flooding mitigation. The model should be evaluated via the implementation of the suggested changes to MEA components to delay GDL flooding, and also via water flux measurements.

Appendix A

Boundary condition for potential at the pore wall: the Pt|solution interface

In Sec. 2.2.3, the boundary condition for potential at the pore wall, Eq. (2.17), was derived for a simple, adsorbate–free metal|solution interface. Here, we consider the impact of adsorption on the surface charge density of a metal|solution interface.

In the presence of specific adsorption, σ and C_H are functions of both ϕ and θ (which depends on pH and ϕ).

$$C_H = \frac{d\sigma}{d(\phi^M - \phi(R,z))} = C_{HF} + C_{d\theta}, \tag{A.1}$$

$$C_{HF} = \left(\frac{\partial\sigma}{\partial(\phi^M - \phi(R,z))}\right)_\theta, \; C_{d\theta} = \left(\frac{\partial\sigma}{\partial\theta}\right)_{(\phi^M - \phi(R,z))} \frac{d\theta}{d(\phi^M - \phi(R,z))}. \tag{A.2}$$

C_{HF} refers to "high frequency" capacitance, where oxide adsorption processes are slower than the potential modulation, and $d\theta$ refers to the capacitance that arises from a change in electronic structure arising from a change in θ [3, 168, 189].

Since σ and C_H are now functions of 2–variables, the path over which the integration of C_H is taken should be specified. One convenient path would be to first deal with the contribution from the change in ϕ^M (i.e. the case of a pore filled with ionomer

where $\phi(R,z) = \phi^o$, neglecting Ohmic losses) and then the contribution arising from the "diffuse layer", i.e. the effect of $\phi(R,z)$, c_{H^+} deviating from the bulk values ϕ^o, $c^o_{\mathrm{H}^+}$, since the ionomer does not extend into the pore,

$$\sigma = \int_{\phi^{pzc}-\phi^o}^{\phi^M-\phi^o} (C_{HF} + C_{d\theta})_{\mathrm{pH}^o} d\phi + \int_{\phi^M-\phi^o}^{\phi^M-\phi(R,z)} (C_{HF})_{\theta^o} d\phi \,, \tag{A.3}$$

The first integral is taken with the capacitances at constant pH^o, and the second at constant θ^o, since with a Poisson–Boltzmann distribution of protons in the diffuse layer, $\theta(z) = \theta^o$ (Sec. 2.4.1).

Pajkossy and Kolb have determined C_{HF} of Pt(111) and Pt(100) in 0.1 $KClO_4$ aqueous solutions of pH = 4–7 at –0.5 to 0.75V_{SHE} [3–5]. Despite the presence of adsorbed oxide species for these solutions at relatively high pH, they found $C_{HF} \sim 20\,\mu\mathrm{F/cm^2}$ with the exception of a pH-independent peak at $\sim$ 0.37 V_{SHE} for Pt(111) and $\sim$ 0.14V_{SHE} for Pt(100), attributed to water re-orientation [5].

The difficulty in applying Eq. (A.3) arises from $C_{d\theta}$ and ϕ^{pzc}. $C_{d\theta}$ is not known, and impedance data cannot be used to determine $C_{d\theta}$, since it cannot be separated from adsorption pseudocapacitances. Frumkin and Petrii's data, as discussed in Sec. 2.3.2, would suggest $C_{d\theta}$ has a substantial effect in the oxide region, given that they observed a second ϕ^{pzc} in the oxide region. There is a wide range of reported values of ϕ^{pzc} (Sec. 2.3.2), due also, perhaps, to oxide formation.

Given these unknowns, we apply Eq. 2.17 to our model system as a first step, with ϕ^{pzc} as a variable parameter, keeping in mind that oxide species likely leads to some complex but largely unsettled effects on the charging of the Pt|solution interface.

Appendix B

Derivation of 1D governing equation system

We perform a heuristic perturbation analysis of the full PNP equations about equilibrium to obtain a simplified 1D governing equation system. For pores with small R, reactant distributions in the radial direction do not deviate significantly from equilibrium values. In the case of oxygen, the characteristic diffusion length in the radial direction is $\lambda_{O_2} = 4FD_{O_2}c^o_{O_2}/j_F$. Assuming a large $|\eta_c| = 0.5$V and a large effectiveness $\Gamma = 1$, $\lambda_{O_2} = 20\mu$m. Since for typical UTCL pores, $R \ll \lambda_{O_2}$, oxygen concentration can be assumed to be uniform at a given z, $c_{O_2}(r,z) = c_{O_2}(z)$. Then, the oxygen continuity equation (Eq. 3.3), integrated from $r = 0$ to R, becomes

$$\partial_t c_{O_2} - D_{O_2}\partial_{zz}c_{O_2} = \frac{j_F}{2FR}. \tag{B.1}$$

Eq. (3.20) gives the linearized transient part.

A similar argument can be made for the proton distribution, which varies with r due to the electric double layer at the metal|solution interface. For the case $|N_{H^+,r}/D_{\mathrm{H}^+}| \ll$

$|\partial_r c_{H^+}|$, $|c_{H^+} k \partial_r \phi|$, the proton concentration distribution is given by a Boltzmann distribution,

$$c_{H^+}(r,z) = c^c_{H^+}(z) \exp\left[-k(\phi(r,z) - \phi^c(z))\right], \tag{B.2}$$

where the superscript "c" refers to values at $r = 0$, the pore centre.

Substituting Eq. (B.2) into the Poisson equation, Eq. (3.2) gives a 2D Poisson Boltzmann equation. At zero flux, $\partial_z \phi = 0$ and ϕ must have a nonzero 2nd derivative in the r direction due to the electric double layer at the metal|solution interface; we thus further assume $\frac{1}{r}\partial_r(r\partial_r\phi) \gg \partial_{zz}\phi$. Then, the Poisson Boltzmann equation reduces to 1D,

$$\frac{1}{r}\partial_r(r\partial_r\phi(r,z)) = -\frac{c^c_{H^+}(z) F \exp\left[-k(\phi(r,z) - \phi^c(z))\right]}{\varepsilon}, \tag{B.3}$$

which has the analytical solution

$$\phi(r,z) - \phi^c(z) = \frac{2}{k}\ln(1 - \Lambda c^c_{H^+}(z) r^2), \tag{B.4}$$

$$c_{H^+}(r,z) = \frac{c^c_{H^+}(z)}{(1 - \Lambda c^c_{H^+}(z) r^2)^2}. \tag{B.5}$$

where both the pore centre potential, $\phi^c(z)$, and pore centre concentration, $c^c_{H^+}(z)$, are functions of z. Λ is the constant factor given by $F^2/8\varepsilon R_g T$. The factor $\Lambda c^c_{H^+} R^2$ is limited to a range $0 < \Lambda c^c_{H^+} R^2 < 1$, since c_{H^+} must be positive, and ϕ is undefined for $\Lambda c^c_{H^+} R^2 \geq 1$

Substituting the above expressions for ϕ and c_{H^+} into the continuity equation for proton concentration, Eq. (3.1), and integrating along r, we obtain a 1D equation in terms of $\phi^c(z)$ and $c^c_{H^+}(z)$,

$$\frac{1}{(1 - \Lambda c^c_{H^+} R^2)}\left[\partial_t c^c_{H^+} - D_{H^+}(\partial_{zz} c^c_{H^+} + k\partial_z c^c_{H^+}\partial_z\phi^c + k c^c_{H^+}\partial_{zz}\phi^c)\right] + \frac{\Lambda R^2}{(1 - \Lambda c^c_{H^+} R^2)^2}\left[c^c_{H^+}\partial_t c^c_{H^+} - D_{H^+}\partial_z c^c_{H^+}(\partial_z c^c_{H^+} + k c^c_{H^+}\partial_z\phi^c)\right] = \frac{2 j_F}{RF}, \tag{B.6}$$

where j_F, written in terms of c_{O_2}, $c^c_{H^+}$ and ϕ^c, is

$$j_F = -j^o \left(\frac{c_{O_2}}{c^o_{O_2}}\right)\left(\frac{c^c_{H^+}}{c^o_{H^+}}\right)^{\gamma}(1-\Lambda c^c_{H^+}R^2)^{2(\alpha-\gamma)}\exp(-\alpha k[\eta_c-\phi^c+\phi^o]). \tag{B.7}$$

Writing the Robin boundary condition for potential at $r = R$ (Eq. 2.17) in terms of $c^c_{H^+}$ and ϕ^c, we obtain a second relation between them,

$$2\ln(1-\Lambda c^c_{H^+}R^2)+k(\phi^c-\phi^o)-\frac{4\varepsilon\Lambda c^c_{H^+}R}{C_H(1-\Lambda c^c_{H^+}R^2)} = k(\phi^M-\phi^{pzc}) \tag{B.8}$$

The three equations, Eqs. (B.1), (B.6), and (B.8), with j_F given by Eq. (B.7), form a simplified 1D set of three coupled equations. Their solution gives $c_{O_2}(z)$, $\phi^c(z)$, and $c^c_{H^+}(z)$.

Like for the full system of equations, we assume a small applied AC signal and linearize the transient part of the simplified 1D system. We make an additional assumption to further simplify the governing equations. We found in Chapter 2 that the steady proton and potential distributions usually do not show significant variation along z under many relevant operating conditions, and were well approximated by the 1D solution to the Poisson-Boltzmann equation for a cylinder. Thus, $\overline{c}^c_{H^+}$ and $\overline{\phi}^c$ can be assumed to vary negligibly along z, i.e. all derivatives of $\overline{c}^c_{H^+}$ and $\overline{\phi}^c$ vanish, which greatly simplifies linearization of the transient part of Eq. (B.6). With this assumption, $\overline{c}^c_{H^+}$ is given implicitly by the steady part of Eq. (2.30), and $\overline{\phi}^c$ by the steady state part of Eq. (2.26), evaluated at $r = 0$,

$$\overline{\phi}^c-\phi^o = \frac{1}{k}\ln\frac{c^o_{H^+}}{\overline{c}^c_{H^+}}\,. \tag{B.9}$$

The corresponding electrostatic effectiveness is

$$\Gamma_{elec} = \left[\frac{(1-\Lambda\overline{c}^c_{H^+}R^2)^2 c^o_{H^+}}{\overline{c}^c_{H^+}}\right]^{\alpha-\gamma}. \tag{B.10}$$

With constant $\overline{c}^c_{H^+}$ and $\overline{\phi}^c$, the linearized transient part of the Robin boundary condition, Eq. (B.8), shows $\delta\phi^c$ to be directly proportional to $\delta c^c_{H^+}$,

$$\delta\phi^c - \delta\phi^M = \frac{c_1}{k}\delta c^c_{H^+}, \tag{B.11}$$

where the proportionality constant is

$$c_1 = \frac{2\Lambda R^2}{1-\Lambda\overline{c}^c_{H^+}R^2}\left(1+\frac{2\varepsilon}{C_H R}\cdot\frac{1}{1-\Lambda\overline{c}^c_{H^+}R^2}\right). \tag{B.12}$$

Eq. (B.11) decouples $\delta\phi^c$ from the three transient governing equations, reducing the number of coupled equations to two.

Applying (B.11) to the linearized, transient parts of both the proton continuity equation (Eq. B.6) and the Faradaic current density (Eq. B.7), we obtain 2 coupled ODEs for $\delta c^c_{H^+}$ and δc_{O_2}, Eqs. (3.19) and (3.20). The transient part of j_F, given by Eq. (3.21), uses the constant c_2

$$c_2 = \frac{\gamma}{\overline{c}^c_{H^+}} + \frac{2\Lambda R^2}{1-\Lambda\overline{c}^c_{H^+}R^2}\left(\gamma+\frac{2\varepsilon\alpha}{C_H R}\frac{1}{1-\Lambda\overline{c}^c_{H^+}R^2}\right). \tag{B.13}$$

Appendix C

PNP equations: Numerical solution method

Numerical solutions to the full 2D set of governing equations and boundary conditions, Eqs. (3.1-3.16), were solved using the Comsol Multiphysics software package, an implementation of the finite element method. Interfaced from Matlab, the Comsol function `femnlin` was used to solve the nonlinear steady state problem and `femlin` was used to solve the linear impedance problem. In the steady state problem, the analytical PB equation was applied as an initial guess and parametric continuation in the exchange current density j_o was used to ensure convergence. Finer meshes were used close to the $z = 0$ and $r = R$ boundaries, due to the steep double layer at the PEM|UTCL interface and the singularity at $(r,z) = (R,0)$. Convergence was verified by computation over a series of finer grids. All calculated numerical impedance spectra used a dimensional $\delta\phi^M = 10\text{mV}$ and 30 logarithmically spaced frequencies in the range $f = 10^{-3} - 10^{8}$ Hz, unless otherwise noted.

Appendix D

Constant factors in solution of transmission line water flux model

The constant factors in the solution to the transmission line model in the V_g case, Eqs. (5.23–5.24), are

$$A_1 = \frac{1}{\Sigma}((R_{CL}^{LV} + R_{MPL}^{V})R_c^V l_c^3 + 4R_c^{LV} R_c^V l_c^2 + 12(R_{CL}^{LV} + R_{MPL}^{V})R_c^{LV} l_c + 12(R_c^{LV})^2) \ , \quad \text{(D.1)}$$

$$A_2 = \frac{1}{\Sigma}\left[R_c^L l_c^2(6(R_{CL}^{LV} + R_{MPL}^{V})R_c^{LV} + 4R_c^V R_c^{LV} l_c + (R_{CL}^{LV} + R_{MPL}^{V})R_c^V l_c^2))\right] \ , \quad \text{(D.2)}$$

$$A_3 = \frac{1}{\Sigma}\left[R_{MPL}^L l_c((R_{CL}^{LV} + R_{MPL}^{V})R_c^{LV} + 6R_c^V R_c^{LV} l_c + (R_{CL}^{LV} + R_{MPL}^{V})R_c^V l_c^2\right] \ , \quad \text{(D.3)}$$

with the denominator Σ

$$\begin{aligned}\Sigma = &-(R_c^V)^2(R_{CL}^{LV} + R_{MPL}^{V})l_c^4 + (R_c^V)^2((R_{CL}^{LV} + R_{MPL}^{V}) - 4R_c^{LV})l_c^3 \\ &+ 4R_c^V R_c^{LV}(-2(R_{CL}^{LV} + R_{MPL}^{V}) + R_c^V)l_c^2 + 12(R_{CL}^{LV} + R_{MPL}^{V})R_c^V R_c^{LV} l_c \\ &+ 12(R_c^{LV})^2((R_{CL}^{LV} + R_{MPL}^{V}) + R_c^V) \ . \end{aligned} \quad \text{(D.4)}$$

In the anode case, where no MPL is considered, $R_{MPL}^L = R_{MPL}^V = 0$.

The constant factors in the solution to the transmission line model in the M regime,

Eqs. (5.25–5.28), are

$$B_1 = \frac{\left[6R_c^{LV}(R_c^L + R_{MPL}^L) - R_c^V R_{MPL}^L + 3R_c^L(R_{CL}^{LV} + R_{MPL}^V)\right]}{2\left(R_c^L + R_{MPL}^L\right)\left(3R_c^V R_c^{LV} + 3(R_{CL}^{LV} + R_{MPL}^V)R_c^{LV} + (R_{CL}^{LV} + R_{MPL}^V)_c^V\right)}, \tag{D.5}$$

$$B_2 = \frac{12(R_c^{LV})^2 + 12(R_{CL}^{LV} + R_{MPL}^V)R_c^{LV} + 4R_c^V R_c^{LV} + R_c^V(R_{CL}^{LV} + R_{MPL}^V)}{4R_c^{LV}(3R_c^V R_c^{LV} + 3(R_{CL}^{LV} + R_{MPL}^V)R_c^{LV} + (R_{CL}^{LV} + R_{MPL}^V)R^V)}, \tag{D.6}$$

$$B_3 = \frac{R_{MPL}^L}{2}\left[\frac{(R_c^V + 3(R_{CL}^{LV} + R_{MPL}^V))}{3R_c^V R_c^{LV} + 3(R_{CL}^{LV} + R_{MPL}^V)R_c^{LV} + (R_{CL}^{LV} + R_{MPL}^V)R_c^V}\right] \tag{D.7}$$

Again, in the anode case, $R_{MPL}^L = R_{MPL}^V = 0$.

Appendix E

Determination of the water transport regime

In this section, we detail the approach for determining the transport regime corresponding to a given j_o. We first require the p^c_{cCL} at the transitions between transport regimes. At the transition from V to V_g, the capillary pressure at the cCL $p^c_{cCL} = 0$. At the transition from V_g to M, the capillary pressure $p^c_{cCL,M}$ is found via Eq. (5.21) with $j^L_c(1) = 0$. (For the anode, the subscripts c are replaced by a).From these capillary pressures, we determine the transition current densities by trial and error of the mass balance equations, where regimes that include V_g are tested last, e.g.,

- Determination of $j_c^{V_g}$. $p^c_{cCL} = 0$
    1. solve mass balance with VVT
    2. if p^c_{aCL} determined is inconsistent with VVT, i.e. $p^c_{aCL} > 0$, solve mass balance with MVT
    3. if p^c_{aCL} determined is inconsistent with MVT, i.e. $p^c_{aCL} < p^c_{aCL,M}$, solve mass balance with V_gVT

- Determination of j_a^M. $p_{aCL}^c = p_{aCL,M}^c$

  1. solve mass balance with MVT
  2. if p_{cCL}^c determined is inconsistent with MVT, i.e. $p_{cCL}^c > 0$, solve mass balance with MMT
  3. if p_{cCL}^c determined is inconsistent with MMT, i.e. $p_{cCL}^c < p_{cCL,M}^c$, solve mass balance with MV$_g$T

Likewise, $j_a^{V_g}$ and j_c^M can also be determined.

With the transition current densities, we determine the transport regime corresponding to a given j_o via the following table:

	$j_o \leq j_c^{V_g}$	$j_c^{V_g} < j_o < j_c^M$	$j^o > j_c^M$
$j_o \leq j_a^{V_g}$	VVT	VV$_g$T	VMT
$j_a^{V_g} < j_o < j_a^M$	V$_g$VT	V$_g$V$_g$T	V$_g$MT
$j_o > j_a^M$	MVT	MV$_g$T	MMT

Table E.1: Table relating transport regimes and transition current densities

For the determination of current densities at the onset of GDL flooding, the procedure is similar. For j_{cGDL}^{fl}, we consider the capillary pressure at the MPL|cGDL boundary, i.e. $p_c^c(0)$. The capillary pressure at the V$_g$ to M transition, $p_{c,M}^c(0)$, can be determined from Eqs. (5.27, 5.28), with $j_c^L(1) = 0$. The determination of j_{cGDL}^{fl} is as follows:

- if $p_{fl,GDL}^c > p_{c,M}^c(0)$,

  1. solve mass balance with VMT
  2. if p_{aCL}^c determined is inconsistent with VMT, i.e. $p_{aCL}^c > 0$, solve mass balance with MMT
  3. if p_{aCL}^c determined is inconsistent with MMT, i.e. $p_{aCL}^c < p_{aCL,M}^c$, solve mass balance with V$_g$MT

- if $p^c_{fl,GDL} < p^c_{c,M}(0)$,

    1. solve mass balance with $\mathrm{VV}_g\mathrm{T}$
    2. if p^c_{aCL} determined is inconsistent with $\mathrm{VV}_g\mathrm{T}$, i.e. $p^c_{aCL} > 0$, solve mass balance with $\mathrm{MV}_g\mathrm{T}$
    3. if p^c_{aCL} determined is inconsistent with $\mathrm{MV}_g\mathrm{T}$, i.e. $p^c_{aCL} < p^c_{aCL,M}$, solve mass balance with $\mathrm{V}_g\mathrm{V}_g\mathrm{T}$

Similarly we can determine the current densities at the onset of flooding in the anode GDL, and at both catalyst layers.

Bibliography

[1] P. D. Beattie, F. P. Orfino, V. I. Basura, K. Zychowska, J. Ding, C. Chuy, J. Schmeisser, S. Holdcroft, *J. Electroanal. Chem.* **503**, 45 (2001).

[2] K. Chan, M. Eikerling, *J. Electrochem. Soc.* **158**, B18 (2011).

[3] T. Pajkossy, D. M. Kolb, *Electrochim. Acta* **46**, 3063 (2001).

[4] Z. Kerner, T. Pajkossy, L. A. Kibler, D. M. Kolb, *Electrochem. Commun.* **4**, 787 (2002).

[5] T. Pajkossy, D. M. Kolb, *Electrochem. Commun.* **5**, 283 (2003).

[6] K. Kreuer, *Proton Conductors: Solids, membranes, and gels - materials and devices* (Cambridge University Press, 1992), p. 476.

[7] J. Welty, C. Wicks, R. Wilson, G. Rorrer, *Fundamentals of Momentum, heat, and Mass Transfer* (John Wiley and Sons, Inc., 2008).

[8] *N.I.S.T. Chemistry Webbook* (http://webbook.nist.gov/chemistry/).

[9] A. Parthasarathy, S. Srinivasan, A. Appleby, *J. Electrochem. Soc.* **139**, 2530 (1992).

[10] D. Sepa, M. Vojnovic, A. Damjanovic, *Electrochim. Acta* **26**, 781 (1981).

[11] D. Archer, P. Wang, *J. Phys. Chem. Ref. Data* **19**, 371 (1990).

[12] A. Parthasarathy, S. Srinivasan, J. Appleby, C. Martin, *J. Electrochem. Soc.* **139**, 2856 (1992).

[13] J. M. LaManna, S. G. Kandlikar, *Int. J. Hydrogen Energy* **36**, 5021 (2011).

[14] M. Adachi, T. Navessin, Z. Xie, B. Frisken, S. Holdcroft, *J. Electrochem. Soc.* **156**, B782 (2009).

[15] M. Baghalha, M. Eikerling, J. Stumper, *ECS Trans.s* **33**, 1529 (2010).

[16] J. T. Gostick, M. A. Ioannidis, M. W. Fowler, M. D. Pritzker, *Electrochem. Comm.* **11**, 576 (2009).

[17] N. Vargaftik, B. N. Volkov, L. D. Voljak, *J. Phys. Chem. Ref. Data.* **12**, 817 (1983).

[18] M. Eikerling, *J. Electrochem. Soc.* **153**, E58 (2006).

[19] K. Bewig, W. Zisman, *Journal of Physical Chemistry* **69**, 4238 (1965).

[20] *2008 US DOE Annual Progress Report* (US Department of Energy - Hydrogen Program, 2008).

[21] J. Larminie, A. Dicks, *Fuel Cell Systems Explained* (Wiley, 2000).

[22] Z. Xia, Q. Wang, M. Eikerling, Z. Liu, *Can. J. Chem.* **86**, 657 (2008).

[23] Y. Wang, K. S. Chen, J. Mishler, S. C. Cho, X. C. Adroher, *Applied Energy* **88**, 981 (2011).

[24] F. Barbir, *PEM Fuel Cells: Theory and Practice* (Elsevier Inc., 2013), second edn.

[25] L. Carrette, K. A. Friedrich, U. Stimming, *Fuel Cells* **1**, 5 (2001).

[26] W. Schmickler, E. Santos, *Interfacial Electrochemistry, 2nd ed.* (Oxford University Press, 2010).

[27] W. Sheng, H. A. Gasteiger, Y. Shao-Horn, *J. Electrochem. Soc.* **157**, B1529 (2010).

[28] K. C. Neyerlin, W. Gu, J. Jorne, H. A. Gasteiger, *J. Electrochem. Soc.* **153**, A1955 (2006).

[29] M. Eikerling, Y. I. Kharkats, A. A. Kornyshev, Y. M. Volfkovich, *J. Electrochem. Soc.* **145**, 2684 (1998).

[30] R. O'Hayre, S.-W. Cha, W. Colella, F. B. Prinz, *Fuel Cell Fundamentals* (Wiley, 2009), second edn.

[31] F. T. Wagner, B. Lakshmanan, M. F. Mathias, *The Journal of Physical Chemistry Letters* **1**, 2204 (2010).

[32] *U.S. D.O.E.: Fuel Economy - Where the energy goes* (http://www.fueleconomy.gov/feg/atv.shtml. Accessed May 2013.).

[33] G. Karlberg, J. Rossmeisl, J. Norskov, *Physical Chemistry Chemical Physics* **9**, 5158 (2007).

[34] V. Stamenkovic, B. Mun, K. Mayrhofer, P. Ross, N. Markovic, J. Norskov, *Angewante Chemie International Edition* **45** (2006).

[35] H. A. Gasteiger, S. S. Kocha, B. Sompalli, F. T. Wagner, *Applied Catalysis B: Environmental* **56**, 9 (2005).

[36] K. Lee, J. Zhang, H. Wang, D. Wilkinson, *Journal of Applied Electrochemistry* **36**, 507 (2005).

[37] H. A. Gasteiger, N. M. Marković, *Science* **324**, 48 (2009).

[38] H. A. Gasteiger, J. E. Panels, S. G. Yan, *J. Power Sources* **127**, 162 (2004).

[39] *2012 US DOE Annual Progress Report* (US Department of Energy - Hydrogen Program, 2012).

[40] J. Wu, X. Z. Yuan, J. J. Martin, H. Wang, J. Zhang, J. Shen, S. Wu, W. Merida, *J. Power Sources* **184**, 104 (2008).

[41] M. F. Mathias, R. Makharia, H. A. Gasteiger, J. J. Conley, T. J. Fuller, C. J. Gittleman, S. S. Kocha, D. P. Miller, C. K. Mittelstead, T. Xie, S. G. Yan, P. T. Yu, *Electrochemical Society Interface* **14**, 24 (2005).

[42] V. R. Stamenkovic, B. Fowler, B. S. Mun, G. Wang, P. Ross, C. A. Lucus, N. M. Markovic, *Science* **315**, 493 (2007).

[43] O. Murphy, G. Hitchens, D. Manko, *J. Power Sources* **47**, 353 (1994).

[44] I. D. Raistrick, *Diaphragms, Separators, and Ion–Exchange Membranes, ECS Proceedings Series* p. 172 (1986).

[45] M. Eikerling, A. A. Kornyshev, *J. Electroanal. Chem.* **453**, 89 (1998).

[46] K. Malek, M. Eikerling, Q. Wang, T. Navessin, Z. Liu, *J. Phys. Chem. C* **111**, 13627 (2007).

[47] H. Zhang, X. Wang, J. Zhang, J. Zhang, *PEM Fuel Cell Catalysts and Catalyst Layers – Fundamentals and Applications* (Springer, 2008), chap. Conventional Catalyst Ink, Catalyst Layer and MEA Preparation.

[48] R. O'Hayre, S.-J. Lee, S.-W. Cha, F. B. Prinz, *J. Power Sources* pp. 483–493 (2002).

[49] M. Saha, A. Gulla, R. Allen, S. Mukerjee, *Electrochim. Acta* **51**, 4680 (2006).

[50] J. M. Tang, K. Jensen, M. Waje, W. Li, P. Larsen, K. Pauley, Z. Chen, P. Ramesh, M. E. Itkis, Y. Yan, R. C. Haddon, *J. Phys. Chem. C* **111**, 17901 (2007).

[51] P. Ramesh, M. E. Itkis, J. M. Tang, R. C. Haddon, *J. Phys. Chem. C* **112**, 9089 (2008).

[52] J. Wee, K. Lee, S. Kim, *J. Power Sources* **165**, 667 (2007).

[53] D. Gruber, N. Ponath, J. Müller, F. Lindstaedt, *J. Power Sources* **150**, 67 (2005).

[54] J. Tang, K. Jensen, W. Li, M. Waje, P. Larsen, P. Ramesh, M. Itkis, Y. Yan, R. Haddon, *Aust. J. Chem.* **60** (2007).

[55] A. Caillard, C. Charles, R. Boswell, P. Brault, C. Coutanceau, *Applied Physics Lett.* **90**, 223119 (2007).

[56] M. K. Debe, A. K. Schmoeckel, G. D. Vernstrom, R. Atanasoski, *J. Power Sources* **161**, 1002 (2006).

[57] Z. Ismagilov, M. Kerzhentsev, N. Shikina, A. Lisitsyn, L. Okhlopkova, C. Barnakov, M. Sakashita, T. Iijima, K. Tadokoro, *Catalysis Today* **102-103**, 58 (2005).

[58] X. Yu, S. Ye, *J. Power Sources* **172**, 145 (2007).

[59] Y. Ding, M. Chen, J. Erlebacher, *J. Am. Chem. Soc.* **126**, 6876 (2004).

[60] R. Zeis, A. Mathur, G. Fritz, J. Lee, J. Erelbacher, *J. Power Sources* **165**, 65 (2007).

[61] M. Debe, *Handbook of Fuel Cells- Fundamentals, Technology, and Applications* **3**, 576 (2003).

[62] M. Debe, A. Schmoeckel, S. Hendricks, G. Vernstrom, G. Haugen, R. Atanasoski, *ECS Trans.* **8**, 51 (2006).

[63] L. Gancs, T. Kobayashi, M. Debe, R. Atanasoski, A. Wieckowski, *Chemistry of Materials* **20**, 2444 (2008).

[64] M. K. Debe, *J. Electrochem. Soc.* **160**, F522 (2013).

[65] P. Red pp. http://www.chemnet.com/Suppliers/13683/Perylene–Red–S–0722–1408597.html. Accessed May 2013.

[66] A. Kongkanand, Z. Liu, I. Dutta, F. T. Wagner, *J. Electrochem. Soc.* **158**, B1286 (2011).

[67] P. K. Sinha, W. Gu, A. Kongkanand, E. Thompson, *J. Electrochem. Soc.* **158**, B831 (2011).

[68] A. Kongkanand, P. K. Sinha, *J. Electrochem. Soc.* **158**, B703 (2011).

[69] A. Kongkanand, M. Dioguardi, C. Ji, E. L. Thompson, *J. Electrochem. Soc.* **159**, F405 (2012).

[70] A. Kongkanand, J. E. Owejan, S. Moose, M. Dioguardi, M. Biradar, R. Makharia, *J. Electrochem. Soc.* **159**, F676 (2012).

[71] A. J. Steinbach, M. K. Debe, J. Wong, M. J. Kurkowski, A. T. Haug, D. M. Peppin, S. K. Deppe, S. M. Hendricks, E. M. Fischer, *ECS Trans.* **33**, 1179 (2010).

[72] A. J. Steinbach, M. K. Debe, M. J. Pejsa, D. M. Peppin, A. T. Haug, M. J. Kurkowski, S. M. Maier-Hendricks, *ECS Transactions* **41**, 449 (2011).

[73] J. Erlebacher, J. Snyder, *ECS Trans.* **25**, 603 (2009).

[74] R. Fan, S. Huh, R. Yan, J. Arnold, P. Yang, *Nat Mater* **7**, 303 (2008).

[75] W. Sparreboom, A. van den Berg, J. C. T. Eijkel, *Nat Nano* **4**, 713 (2009).

[76] H. Daiguji, *Chem. Soc. Rev.* **39**, 901 (2010).

[77] M. Nishizawa, V. P. Menon, C. R. Martin, *Science* **268**, 700 (1995).

[78] C. R. Martin, M. Nishizawa, K. Jirage, M. Kang, *The Journal of Physical Chemistry B* **105**, 1925 (2001).

[79] D. Stein, M. Kruithof, C. Dekker, *Phys. Rev. Lett.* **93**, 035901 (2004).

[80] E. Thompson, D. Baker, *ECS Trans.* **41**, 709 (2011).

[81] J. McBreen, *J. Electrochem. Soc.* **132**, 1112 (1985).

[82] W.-Y. Tu, W.-J. Liu, C.-S. Cha, B.-L. Wu, *Electrochimica Acta* **43**, 3731 (1998).

[83] U. Paulus, Z. Veziridis, B. Schnyder, M. Kuhnke, G. Scherer, A. Wokaun, *J. Electroanal. Chem.* **541**, 77 (2003).

[84] Q. Wang, M. Eikerling, D. Song, Z. Liu, *J. Electrochem. Soc.* **154**, F95 (2007).

[85] W. Im, B. Roux, *J. Mol. Biol.* **322**, 851 (2002).

[86] S. Y. Noskov, W. Im, B. Roux, *Biophys. J.* **87**, 2299 (2004).

[87] J. Keener, *Mathematical Physiology* (Springer-Verlag, New York, 1998).

[88] R. Coalson, M. Kurnikova, *Biological membrane ion channels: dynamics, structure, and applications* (Springer, 2007), chap. "Poisson-Nernst-Planck Theory of Ion Permeation Through Biological Channels.

[89] A. Bard, L. Faulkner, *Electrochemical Methods, Fundamentals and Applications* (John Wiley and Sons, Inc, 2001).

[90] W. Schmickler, *Interfacial Electrochemistry* (Oxford University Press, 1996).

[91] A. Bonnefont, F. Argoul, M. Z. Bazant, *J. Electroanal. Chem.* **500**, 52 (2001).

[92] P. M. Biesheuvel, Y. Fu, M. Z. Bazant, *Phys. Rev. E* **83**, 061507 (2011).

[93] B. E. Benjaminsen, Nanoflow of protons and water in polymer electrolyte membranes, *Tech. rep.*, Norwegian University of Science and Technology (2013).

[94] D. Sepa, M. Vojnovic, A. Damjanovic, *Electrochim. Acta* **32**, 129 (1987).

[95] A. Damjanovic, *Electrochemistry in Transition* (Plenum Press, 1992), pp. 107–126.

[96] M. Gattrell, B. MacDougall, *Handbook of Fuel Cells - Fundamentals, Technology and Applications* (John Wiley and Sons, Inc, 2003), vol. 2: Electrocatalysis, chap. 30: Reaction mechanisms of the O_2 reduction/evolution reaction.

[97] K. Mayrhofer, D. Strmcnik, B. Blizanac, V. Stamenkovic, M. Arenz, N. Markovic, *Electrochim. Acta* **53**, 3181 (2008).

[98] A. Frumkin, O. Petrii, *Electrochim. Acta* **20**, 347 (1975).

[99] S. Trassatti, E. Lust, *Modern Aspects of Electrochemistry*, no. 33 (Kluwer Academic/Plenum, 1999), chap. 1. The Potential of Zero Charge.

[100] V. Climent, N. Garcia-Araez, E. Herrero, J. Feliu, *Russ. J. Electrochem.* **42**, 1145 (2006).

[101] M. J. Weaver, *Langmuir* **14**, 3932 (1998).

[102] U. Hamm, D. Kramer, R. Zhai, D. Kolb, *J. Electroanal. Chem.* **414**, 85 (1996).

[103] O. Petrii, *Electrochim. Acta* **41**, 2307 (1996).

[104] F. Tian, R. Jinnouchi, A. Anderson, *J. Phys. Chem. C* **113**, 17484 (2009).

[105] R. Paul, S. J. Paddison, *J. Phys. Chem. B* **108**, 13231 (2004).

[106] R. Paul, *Device and Materials Modeling in PEM Fuel Cells* (Springer-Berlin/Heidelberg, 2009), chap. Modeling the State of Water in Polymer Electrolyte Membranes.

[107] H. Tsao, *J. Phys. Chem. B* **102**, 10243 (1998).

[108] P. Berg, K. Ladipo, *Proc. R. Soc. A* **465**, 2663 (2009).

[109] M. Eikerling, A. A. Kornyshev, A. M. Kuznetsov, J. Ulstrup, S. Walbran, *J. Phys. Chem. B* **105**, 3646 (2001).

[110] F. Baldessari, *J. Colloid Interface Sci.* **325**, 526 (2008).

[111] K. J. J. Mayrhofer, B. B. Blizanac, M. Arenz, V. R. Stamenkovic, P. N. Ross, N. M. Markovic, *J. Phys. Chem. B* **109**, 14433 (2005).

[112] T. Soboleva, Z. Xie, Z. Shi, E. Tsang, T. Navessin, S. Holdcroft, *J. Electroanal. Chem.* **622**, 145 (2008).

[113] M.-S. Kang, C. R. Martin, *Langmuir* **17**, 2753 (2001).

[114] M. Schmuck, P. Berg, *Applied Mathematics Research eXpress* (2012).

[115] A. Bonakdarpour, K. Stevens, G. Vernstrom, R. Atanasoski, A. Schmoeckel, M. Debe, J. Dahn, *Electrochim. Acta* **53**, 688 (2007).

[116] B. Grgur, N. Markovic, P. Ross, *Can. J. Chem.* **75**, 1465 (1997).

[117] A. Sarapuu, S. Kallip, A. Kasikov, L. Matisen, K. Tammeveski, *J. Electroanal. Chem.* **624**, 144 (2008).

[118] A. Bonakdarpour, K. Stevens, G. D. Vernstrom, R. Atanasoski, A. K. Schmoeckel, M. K. Debe, J. R. Dahn, *Electrochim. Acta* **53**, 688 (2007).

[119] S. Rinaldo, J. Stumper, M. Eikerling, *J. Phys. Chem. C* **114**, 5773 (2010).

[120] V. Markin, I. Chizmadzhev, I. Chirkov, *Doklady Akademii Nauk SSSR* **150**, 596 (1963).

[121] S. Srinivasan, H. D. Hurwitz, J. O. Bockris, *J. Chem. Phys.* **46**, 3108 (1967).

[122] R. de Levie, *Advances in Electrochemistry and Electrochemical Engineering* (Interscience Publishers, 1967), vol. 6, p. 329.

[123] K. Chan, M. Eikerling, *J. Electrochem. Soc.* **159**, B155 (2012).

[124] E. Barsoukov, J. R. Macdonald, eds., *Impedance Spectroscopy: Theory, Experiment, and Applications, 2nd Edition* (Wiley, 2005).

[125] M. Eikerling, A. Kornyshev, *J. Electroanal. Chem.* **475**, 107 (1999).

[126] M. Keddam, C. Rakotomavo, H. Takenouti, *J. Appl. Electrochem.* **14**, 437 (1984).

[127] M. D. Gasda, G. A. Eisman, D. Gall, *J. Electrochem. Soc.* **157**, B437 (2010).

[128] A. Lasia, *ECS Trans.* **13**, 1 (2008).

[129] Y. Liu, M. W. Murphy, D. R. Baker, W. Gu, C. Ji, J. Jorne, H. A. Gasteiger, *J. Electrochem. Soc.* **156**, B970 (2009).

[130] Y. Liu, C. Ji, W. Gu, D. R. Baker, J. Jorne, H. A. Gasteiger, *J. Electrochem. Soc.* **157**, B1154 (2010).

[131] K. Wiezell, P. Gode, G. Lindbergh, *J. Electrochem. Soc.* **153**, A759 (2006).

[132] S. K. Roy, M. E. Orazem, B. Tribollet, *J. Electrochem. Soc.* **154**, B1378 (2007).

[133] M. Mathias, D. Baker, J. Zhang, Y. Liu, W. Gu, *ECS Trans.* **13**, 129 (2008).

[134] M. K. Debe, Advanced mea's for enhanced operating conditions, amenable to high volume manufacture (2007).

[135] M. Debe, *DOE Hydrogen Program Review, Advanced Cathode Catalysts and Supports for PEM Fuel Cells* (2010).

[136] M. Debe, Private communication.

[137] T. Kolotyrkina, O. Petrii, W. Kazarinov, *Elektrokhimiya* **10**, 1352 (1974).

[138] J. Norskov, J. Rossmeisl, A. Logadottir, L. Lindqvist, J. Kitchin, T. Bligaard, H. Jonsson, *J. Phys. Chem. B* **108**, 17886 (2004).

[139] J. Rossmeisl, K. Chan, R. Ahmed, V. Tripkovic, M. E. Bjorketun, *Phys. Chem. Chem. Phys.* **15**, 10321 (2013).

[140] N. M. Markovic, S. T. Sarraf, H. A. Gasteiger, P. N. Ross, *J. Chem. Soc., Faraday Trans.* **92**, 3719 (1996).

[141] R. Subbaraman, D. Tripkovic, D. Strmcnik, K.-C. Chang, M. Uchimura, A. P. Paulikas, V. Stamenkovic, N. M. Markovic, *Science* **334**, 1256 (2011).

[142] J. Kohanoff, *Electronic Structure Calculations for Solids and Molecules: Theory and Computational Methods* (Cambridge University Press, 2006).

[143] B. Hammer, L. B. Hansen, J. K. Nørskov, *Phys. Rev. B* **59**, 7413 (1999).

[144] *Dacapo pseudopotential code* (https://wiki.fysik.dtu.dk/dacapo, Center for Atomic-scale Materials Design (CAMD), Technical University of Denmark, Lyngby).

[145] J. Enkovaara, *et al.*, *J. Phys.: Condens. Matter* **22**, 253202 (2010).

[146] C. Rostgaard, *The Projector Augmented Wave Method*, http://arxiv.org/abs/0910.1921 (2009).

[147] J. Enkovaara, *CAMD Summer School 2012* (Lyngby, Denmark, 2012).

[148] J. Greeley, I. E. L. Stephens, A. S. Bondarenko, T. P. Johansson, H. A. Hansen, T. F. Jaramillo, J. Rossmeisl, I. Chorkendorff, J. K. Nørskov, *Nat Chem* **1**, 552 (2009).

[149] J. K. Nørskov, T. Bligaard, J. Rossmeisl, C. H. Christensen, *Nat Chem* **1**, 37 (2009).

[150] F. Calle-Vallejo, M. T. Koper, *Electrochim. Acta* (2012).

[151] G. S. Karlberg, T. F. Jaramillo, E. Skúlason, J. Rossmeisl, T. Bligaard, J. K. Nørskov, *Phys. Rev. Lett.* **99**, 126101 (2007).

[152] C. D. Taylor, S. A. Wasileski, J.-S. Filhol, M. Neurock, *Phys. Rev. B* **73**, 165402 (2006).

[153] J. Rossmeisl, E. Skúlason, M. E. Björketun, V. Tripkovic, J. K. Nørskov, *Chem. Phys. Lett.* **466**, 68 (2008).

[154] M. Otani, O. Sugino, *Phys. Rev. B* **73**, 115407 (2006).

[155] J. Cheng, M. Sprik, *Phys. Chem. Chem. Phys.* **14**, 11245 (2012).

[156] S. Schnur, A. Groß, *Catalysis Today* **165**, 129 (2011).

[157] J. Rossmeisl, J. Greeley, G. Karlberg, *Fuel Cell Catalysis: A Surface Science Approach* (Wiley, 2009), chap. Electrocatalysis and Catalyst Screening from Density Functional Theory Calculations.

[158] A. A. Peterson, F. Abild-Pedersen, F. Studt, J. Rossmeisl, J. K. Norskov, *Energy Environ. Sci.* **3**, 1311 (2010).

[159] S. Trasatti, *Pure & Appl. Chem.* **58**, 955 (1986).

[160] V. Tripkovic, M. E. Björketun, E. Skúlason, J. Rossmeisl, *Phys. Rev. B* **84**, 115452 (2011).

[161] I. Dabo, N. Bonnet, Y. L. Li, N. Marzari, *Fuel cell science : theory, fundamentals, and biocatalysis* (Wiley, 2010), chap. Ab-initio electrochemical properties of electrode surfaces.

[162] E. Skúlason, V. Tripkovic, M. E. Björketun, S. Gudmundsdóttir, G. Karlberg, J. Rossmeisl, T. Bligaard, H. Jónsson, J. K. Nørskov, *J. Phys. Chem. C* **114**, 18182 (2010).

[163] H. Ogasawara, B. Brena, D. Nordlund, M. Nyberg, A. Pelmenschikov, L. G. M. Pettersson, A. Nilsson, *Phys. Rev. Lett.* **89**, 276102 (2002).

[164] J. J. Mortensen, L. B. Hansen, K. W. Jacobsen, *Phys. Rev. B* **71**, 035109 (2005).

[165] S. R. Bahn, K. W. Jacobsen, *Comput. Sci. Eng.* **4**, 56 (2002).

[166] L. Bengtsson, *Phys. Rev. B* **59**, 12301 (1999).

[167] M. Pourbaix, *Atlas of electrochemical equilibria in aqueous solutions* (Pergamon Press, 1966).

[168] N. Garcia-Araez, V. Climent, E. Herrero, J. M. Feliu, J. Lipkowski, *Electrochim. Acta* **51**, 3787 (2006).

[169] A. Peremans, A. Tadjeddine, *Phys. Rev. Lett.* **73**, 3010 (1994).

[170] G. Jerkiewicz, G. Vatankhah, S.-i. Tanaka, J. Lessard, *Langmuir* **27**, 4220 (2011).

[171] K. J. P. Schouten, M. J. T. C. van der Niet, M. T. M. Koper, *Phys. Chem. Chem. Phys.* **12**, 15217 (2010).

[172] J. Rossmeisl, J. K. Nørskov, C. D. Taylor, M. J. Janik, M. Neurock, *J. Phys. Chem. B* **110**, 21833 (2006).

[173] M. van der Niet, N. Garcia-Araez, J. Hernandez, J. M. Feliu, M. Koper, *Catalysis Today* **202**, 105 (2013).

[174] J. Liu, J. Gazzarri, M. Eikerling, *Fuel Cells* (2013).

[175] S. Renganathan, Q. Guo, V. A. Sethuraman, J. W. Weidner, R. E. White, *J. Power Sources* **160**, 386 (2006).

[176] A. Bazylak, D. Sinton, N. Djilali, *J. Power Sources* **176**, 240 (2008).

[177] C. Hartnig, I. Manke, R. Kuhn, S. Kleinau, J. Goebbels, J. Banhart, *J. Power Sources* **188**, 468 (2009).

[178] J. P. Owejan, J. E. Owejan, W. Gu, T. A. Trabold, T. W. Tighe, M. F. Mathias, *J. Electrochem. Soc.* **157**, B1456 (2010).

[179] E. C. Kumbur, K. V. Sharp, M. M. Mench, *J. Electrochem. Soc.* **154**, B1295 (2007).

[180] J. Liu, M. Eikerling, *Electrochim. Acta* **53**, 4435 (2008).

[181] H. Wu, X. Li, P. Berg, *Electrochimica Acta* **54**, 6913 (2009).

[182] J. Divisek, M. Eikerling, V. Mazin, H. Schmitz, U. Stimming, Y. M. Volfkovich, *J. Electrochem. Soc.* **145**, 2677 (1998).

[183] M. H. Eikerling, P. Berg, *Soft Matter* **7**, 5976 (2011).

[184] Udo, Kaatze, *Radiation Physics and Chemistry* **45**, 539 (1995).

[185] Z. Lu, M. M. Daino, C. Rath, S. G. Kandlikar, *Int. J. Hydrogen Energy* **35**, 4222 (2010).

[186] O. Lu, Private presentation.

[187] S. G. Rinaldo, C. W. Monroe, T. Romero, W. Merida, M. Eikerling, *Electrochem. Comm.* **13**, 5 (2011).

[188] D. Gerteisen, T. Heilmann, C. Ziegler, *J. Power Sources* **177**, 348 (2008).

[189] J. Mostany, E. Herrero, J. M. Feliu, J. Lipkowski, *J. Electroanal. Chem.* **558**, 19 (2003).